國立中山大學材料科學研究所

碩士論文

鎂銅銀釓塊狀非晶質合金之玻璃形成能力及機械性質

Glass Forming Ability and Mechanical Properties of Mg-Cu-Ag-Gd Bulk Metallic Glasses

研究生：陳海明 撰

指導教授：黃志青 博士

中華民國 九十五 年 七 月

國立中山大學研究生學位論文審定書

本校材料科學研究所碩士班

研究生陳海明（學號：M933060008）所提論文

鎂銅銀釓塊狀非晶質合金之玻璃形成能力及機械性質
Glass Forming Ability and Mechanical Properties of Mg-Cu-Ag-Gd Bulk Metallic Glasses

經本委員會審查並舉行口試，符合碩士學位論文標準。

學位考試委員簽章：

鄭憲清　　黃志青

謝克昌

指導教授(可免) 黃志青

系主任/所長(可免)

致謝

轉眼間在中山研究所的兩年就要落幕了，在材料所求學這段期間，讓我體驗到很多可貴的經驗，結交到許多知心的好友，研究室的溫暖、師長們的教誨、同學間的相處以及研究時遇到的難題與辛酸，這些都讓我有著難忘的經驗與回憶，我想在中山這兩年的時光對我將來的人生將會是重要的轉戾點。

回顧這兩年期間，首先我要感謝我的指導教授 黃志青老師，在做人做事上以及課業的指導上，老師一直都不遺餘力的支持我教導我，使我的論文得以完成，在研究上，老師給予我很多自由的空間，讓我能充分的發揮自我，使我能夠盡情地從事論文研究，因此我要特別感謝老師這麼的挺我，在此我想要跟老師說一聲：「老師，謝謝你！」此外，我也要感謝謝克昌老師以及鄭憲清老師在論文方面給予的指導與意見，使學生的論文更為完善令我獲益良多。

在我精采的研究生涯中我受到許多的人的協助，首先，我要先特別感謝實驗室非晶質組的第一把交椅子翔學長，學長在我的研究中給予我很多的指導以及協助。接著，我要感謝已經畢業現在站在第一前線為國家貢獻的宇庭學長，他交會了我很多東西；另外我要謝謝實驗室的鉉凱、英博、育誠、敬仁、志溢、友杰、家豪、政信等學長在生活上的照顧；然後我要感謝我那些可愛的學弟妹鴻昇、致榮、浩然、振偉、哲男，有了你們陪伴讓我的生活更多彩多姿。此外，我由衷的感謝義守大學可愛的學弟阿聰，阿富在實驗上給予的協助。

再來我要感謝我的同袍戰友炎暉、育霖、俊宏(百九)、阿強、弘杰(冰紅茶)、靖允(時尚男)、俊誠(賴肥)以及材料所的眾美女們宜珊、馨儀、麗君、宜亭，有了你們的陪伴讓我更珍惜這份回憶，在研究所期間大家一起奮鬥，一起玩樂，扯出的一些荒唐事以

及幹過的那些豐功偉業，這些大家一起經歷過的酸甜苦辣，將會是我這輩子無價的財富；最後我要感謝我的父母以及家人，在學業上或生活上一直都默默的支持與不斷的鼓勵我，讓我能夠無後顧之憂的向前邁進面對挑戰，爸媽我愛你們。

Content

Table List

Figures List

論文摘要

近幾十年來，非晶質合金因具有一些獨特的物理性質及化學性質，因此引起世界各地眾多學者的研究與探討，隨著時代進步許多研究家的努力下，以往在非晶質合金製造尺寸限制的難題早已克服，其中塊狀非晶質合金為最近這幾年的研究主流，而在眾多非晶質合金系統中，鎂基非晶質合金因其具有高比強度，低玻璃轉換溫度和低密度等特性，因此在輕金屬之應用中，佔有相當大的發展潛力及優勢。

本實驗為鎂基塊狀非晶質合金之玻璃形成能力及機械性質之研究。$Mg_{65}Cu_{25}Gd_{10}$ 合金經由傳統的銅模鑄造方式能夠成功的製作出具直徑 3-6 mm 及長度約 5 cm 的棒材，而藉由銀的添加後發現，$Mg_{65}Cu_{15}Ag_{10}Gd_{10}$ 合金亦可製作出相同尺寸大小的棒材。

在熱性質方面，$Mg_{65}Cu_{25}Gd_{10}$ 非晶質合金顯示出寬廣的過冷液體區間，意味著其具有優良的熱穩定性，此外根據非晶質合金玻璃形成能力的參考指標，其結果顯示 $Mg_{65}Cu_{25}Gd_{10}$ 擁有良好的玻璃形成能力，然而銀的添加會使得 $Mg_{65}Cu_{15}Ag_{10}Gd_{10}$ 非晶質合金降低其熱穩定性及γ值，然而在 T_{rg} 方面卻有著較高的值。在微氏硬度量測方面，$Mg_{65}Cu_{25}Gd_{10}$ 非晶質合金顯示著非晶質高硬度之特性，再者銀添加的效應對於硬度來說更能有效增加其硬度。

在熱機性質方面，以 $Mg_{65}Cu_{25}Gd_{10}$ 塊狀非晶質合金為主，藉由熱機械分析儀(TMA)及動態機械分析儀(DMA)來進行量測，藉著溫度的提升非晶質合金結構從室溫的玻璃固態至高溫的玻璃轉換溫度時結構轉換成黏滯流體，而進一步升至更高溫接近結晶溫度時結構會從黏滯流體轉換成具結晶化固體，研究顯示，熱機性質深受其非晶質合金在升溫度過程中結構的變化之影響，另一方面亦可發現，在玻璃泰以及結晶化時皆具有鎂合金的熱膨脹行為，而當溫度升至過冷液體區間時，非晶質合金轉變成黏滯流體而具有很大

的形變量。

在室溫的壓縮測試方面，以 $Mg_{65}Cu_{25}Gd_{10}$ 塊狀非晶質合金棒材具不同高度與直徑比例為 2、1、0.5 及 0.25 進行壓縮測試。研究顯示壓縮破壞強度、變形應變及彈性模數會依不同的試片尺寸比例呈現不同的變化，對於高度直徑比為 2：1 及 1：1 其壓縮強度約為 600-800 MPa，破壞應變為 1-2 %以及彈性模數約為 40-60 GPa，進行破斷面的觀察則呈現一般鎂基塊狀非晶質合金的脆性破斷之性質。然而，對於高度直徑比為 0.25 之試片則為不同之結果，其破壞應變明顯增加至約 17%，破斷面的觀察則可發現大量脈紋狀(vein)的結構分布於整個試片，因此對於高度直徑比例小的試片來說可發現其具有良好的延性，由此來看，說明不同的非晶質合金幾何形狀於壓縮期間有著不同的變形機構在進行。

Abstract

The thermal and mechanical properties of the Mg-based bulk metallic glasses are reported in this thesis. The original ingots were prepared by arc melting and induction melting. The $Mg_{65}Cu_{25}Gd_{10}$ and $Mg_{65}Cu_{15}Ag_{10}Gd_{10}$ bulk metallic glasses with different diameters from 3 to 6 mm were successfully fabricated by conventional copper mold casting in an inert atmosphere.

The $Mg_{65}Cu_{25}Gd_{10}$ bulk metallic glass shows the high glass forming ability and good thermal stability. However, the addition of Ag in the $Mg_{65}Cu_{15}Ag_{10}Gd_{10}$ alloy degrades the thermal stability. Based on the DSC results, the supercooled liquid region ΔT_x and glass forming criterion γ decrease from 69 K and 0.423 for $Mg_{65}Cu_{25}Gd_{10}$ to 43 K and 0.408 for $Mg_{65}Cu_{15}Ag_{10}Gd_{10}$. However, the addition of Ag will increase the hardness from 232 H_v for $Mg_{65}Cu_{25}Gd_{10}$ to 255 H_v for $Mg_{65}Cu_{15}Ag_{10}Gd_{10}$.

Based on the thermal mechanical analyses, during heating, the temperature interval in which a rapid change in displacement occurs is close to the supercooled liquid region of the $Mg_{65}Cu_{25}Gd_{10}$. Based on the dynamic mechanical analyses, the structure changes from glass solid to viscous flow liquid and finally to crystalline solid state with increasing temperature, resulting in that the thermal mechanical properties of the $Mg_{65}Cu_{25}Gd_{10}$ would change.

The mechanical properties of $Mg_{65}Cu_{25}Gd_{10}$ in terms of compression testing are examined using an Instron 5582 universal testing machine. Room temperature compression tests are conducted on specimens with various height to diameter ratios (h/d) from 2:1, 1:1, 1:2 to 1:4. The fracture strength and the deformation strain, as well as the fracture surface morphologies, were formed to vary systematically in accordance with the specimen h/d ratio. The possible deformation mechanisms of the Mg-based bulk metallic glasses are discussed.

Chapter 1 Introduction

1.1 Amorphous metallic alloys

Amorphous metallic alloys are disordered materials that lack the periodicity of crystals. The structure of amorphous metallic alloys could be defined by the presence of short range order in contrast to crystalline materials showing long range order with repeating unit cell. However, the atomic arrangement in amorphous alloys is not completely random, but maintains a greater degree of short range order than that in a liquid, as shown in Figure 1.1 [1]. Usually, amorphous metallic alloys have also been called as liquid metals, non-crystalline metals, glassy metals, or metallic glasses.

Generally, high cooling rates are required to produce amorphous alloys in the form of ribbons, flakes or powders and great efforts have been made to consolidate this material into bulk amorphous part. In recent years, more and more researchers worldwide discover the better ways to fabricate amorphous alloys by employing much lower cooling rates or the combination of alloy compositions for glassy metals. The increased demand for light and strong materials able to withstand severe environmental conditions has stimulated considerable research on bulk metallic glasses (BMGs). Bulk amorphous alloys can expand the application area further by eliminating the size limit.

It has been shown that amorphization of metallic materials might cause sometimes excellent increase in mechanical strength and toughness compared with those of the corresponding crystalline alloys. Amorphous metallic alloys have unique mechanical and physical properties attributed to the atomic structure of amorphous phase, such as high strength and hardness, low elastic modulus, excellent corrosion resistance, electromagnetic properties, and easy shaping or forming ability [2], which are different from the corresponding crystalline alloys. The fundamental properties and application fields of amorphous alloys are listed in Table 1.1 [3].

1.2 The development of Mg-based amorphous alloys

Among a large number of alloys, Mg-based alloys have attracted attention especially due to a high strength to weight ratio and a low glass transition temperature. From the industrial needs of developing high strength materials with light weight, Mg-based alloys have attracted more and more interest due to the lowest specific weight among all structural metallic materials. Mg-based BMGs are regarded as a new family of promising materials with excellent specific strength and good corrosion resistance [4].

New Mg-based ternary amorphous alloys with a wide supercooled liquid region and a high glass formation ability have been developed in a number of alloy systems, such as Mg-TM-Y (TM = transition metal such as Cu, Ni, Zn). The formation of the Mg-based BMGs was firstly reported in 1991. In 1991, Inoue et al. [5] found that the Mg-Cu-Y alloys exhibited a high glass formation ability (GFA), which made it possible to produce bulk amorphous samples with a diameter of 4 mm by the copper mold casting method. Furthermore, the Mg-based BMGs exhibited high tensile fracture strength which is more than twice as high as the highest strength of conventional Mg-based crystalline alloys. Next year, Inoue's group [6] succeeded in fabricating bulk $Mg_{65}Cu_{25}Y_{10}$ metallic glasses with increased diameter up to 7 mm by using high-pressure die casting method. Since them, a new family of light amorphous alloy systems became available.

1.3 The effects of alloy additions in Mg-based alloys

The synthesis of the multicomponent metallic glasses with superior GFA is of scientific and technological interest because of their potential application as new structural and functional materials. In the last decade, advances in the synthesis of metallic glasses, especially by using unique combinations of elements to form the multi-component metallic glasses, have resulted in the critical cooling rate dropping from 10^5 K/s to as low as 1 K/s, and the specimen size increasing from 0.05 mm to as large as 80 mm [7]. So far, the investigations worldwide have shown efforts on the improvement of the GFA by additions of the alloy elements on Mg-based BMGs.

Liu and Lu [8] have reviewed the recent works regarding the effects of minor alloying additions on glass formation in bulk metallic glasses. Recently, minor alloying addition has shown to have dramatic effects on the glass formation and thermal stability of many bulk metallic glasses. Liu and Lu suggested to add a small amount of alloying additions (usually, less than 2 at%) to the existing bulk metallic glasses for the purpose of further improving their GFA. Experimental evidences indicate that alloying additions of small atoms with atomic radius smaller than 0.12 nm (such as B and Si) or large atoms with radius greater than 0.16 nm (such as Y and Sc) are most effective in enhancing glass forming ability.

Further improvement of GFA has been reported in the Mg-Cu-Y alloy system where Cu is partially substituted with other alloy elements, such as Ag, Pd, or Zn. For example, $Mg_{65}Cu_{15}Ag_{10}Y_{10}$ [9], $Mg_{65}Cu_{15}Ag_5Pd_5Y_{10}$ [10], and $Mg_{65}Cu_{20}Zn_5Y_{10}$ [11-12] alloys all exhibit high GFA, enabling the fabrication of BMGs in rods with diameters of 6, 7 and 6 mm, respectively, by a Cu mold injection casting method.

Subsequently, a series of $Mg_{65}Cu_{25}RE_{10}$ BMGs (RE = rare earth elements such as La, Ce, Pr, Nd, Sm, Gd, Dy, Tb, Ho, Er and Yb) have been investigated [13-14]. As proposed by Men et al. [15], the effect of the substitution of Y in $Mg_{65}Cu_{25}Y_{10}$ alloy with Gd on GFA and thermal stability is significant improvement. The $Mg_{65}Cu_{25}Gd_{10}$ alloy with a high GFA enables the fabrication of BMG samples with a maximum diameter 8 mm by Cu mold injection casting method in inert atmosphere. Recently, Inoue et al. [4,16] proposed that the partial substitution of Cu by Ni significantly improves mechanical properties of Mg-Cu-Gd BMGs while keeping good GFA. The $Mg_{65}Cu_{20}Ni_{5}Gd_{10}$ BMG sample of 5 mm in diameter was fabricated by Cu mold casting method in an argon atmosphere. In spite of the degradation in terms of the narrower supercooled liquid region with increasing Ni content, the proper substitution of Cu by Ni in $Mg_{65}Cu_{25}Gd_{10}$ BMGs can result in the improvement of ductility and strength.

1.4 The purpose of this study

On the present reports, Gd and Y have similar atomic radii (Gd: 0.18013 nm; Y: 0.18015 nm), similar electronegativity (Gd: 1.2; Y: 1.22) and similar negative heat of mixing against Mg and Cu (Mg-Gd: -6 kJ/mol; Cu-Gd: -22 kJ/mol; Mg-Y: -6 kJ/mol; Cu-Y: -22 kJ/mol). The effect of substitution of Y with Gd in the $Mg_{65}Cu_{25}Y_{10}$ alloy on the GFA has a significant improvement, enabling the fabrication of the BMG with a diameter from 4 mm up to 8 mm by Cu mold casting method, possibly because of the difference in the electronic configurations between Y ($4d^{1}5s^{2}$) and Gd ($4f^{7}5d^{1}6s^{2}$). Among the Mg-based ternary alloys, the $Mg_{65}Cu_{25}Gd_{10}$ alloys have the highest the glass forming ability and high thermal stability.

With the partial substitution of Cu by Ag, the Mg-Cu-Ag-Y system was claimed to have higher glass forming ability. It possibly would be inferred that because of the reduction for the temperature interval from T_g to T_l enables the Ag-containing alloy to have high glass forming ability. On the other hand, it was expected that by the addition of Ag could generate strongly negative ΔH_{mix} for Mg-Ag and Gd-Ag in the Mg-Cu-Gd alloy system, more than those of Mg-Cu and Gd-Cu. Therefore, the more negative heats of mixing for Ag with Mg and Gd allow us to presume that the bonding forces among Mg, Cu, Ag and Gd elements are stronger than those among Mg, Cu and Gd elements. The substitution of Cu by Ag in the Mg-Cu-Gd alloy system should enhance the bonding force between the constituent atoms, so that it is more difficult to deform the Ag containing alloy than Ag-free alloy. Hence, it would be useful to improve the hardness and fracture strength on mechanical properties for the Ag containing alloy.

In this study, it is intended to investigate the influence of the partial substitution of Cu by Ag in the $Mg_{65}Cu_{25}Gd_{10}$ alloys on the amorphous nature, thermal stability and the glass forming ability. In addition, Most of the investigations on the mechanical properties of BMGs are concentrated on the Zr-based and Pd-based BMGs. In contrast, the investigations on the mechanical properties for the Mg-based BMGs are not enough. Hence, in order to evaluate the mechanical properties of the Mg-based BMGs, the $Mg_{65}Cu_{25}Gd_{10}$ BMG fabricated by the Cu mold casting method in an argon atmosphere with diameter of 4 mm will be applied to conduct the microhardness testing, compressive test and thermal mechanical analysis. On the other hand, in order to clarify the deformation mechanisms of the Mg-based BMGs, the room temperature compression tests will be conducted on specimens with various height to diameter ratios (h/d) from 2:1, 1:1, 1:2 to 1:4. The possible deformation mechanisms on specimens with various geometry ratios will be discussed.

Chapter 2 Background and Literature Review

2.1 The evolution of amorphous alloys

The amorphous metallic alloys was first fabricated in 1960 by Duwez et al. [17] by splat quenching method in the Au-Si system, it is recognized that this is the first method to rapidly quench from the melt metallic liquid to fabricate the metallic glass ribbons. A few years latter, Chen et al. [18] were able to make amorphous spheres of ternary alloy system in Pd-Si-N (N = Ag, Cu or Au). The alloy $Pd_{77.5}Cu_6Si_{16.5}$ could be made glassy with a diameter of 0.5 mm and the existence of a glass transition was demonstrated. In the Pd-Cu-Si and Pd-Ag-Si alloys, the supercooled liquid region extended to 40 K, it enables the investigators to perform the first detailed studies of crystallization in metallic glasses. In addition, Chen [19] made systematic investigations on the ternary Pd-T-P alloys (T = Ni, Co or Fe) in 1974 and obtained a critical casting thickness on the order of 1 mm in these alloys.

In the beginning of the 1980s, the Turnbull et al. [20] revisited the Pd-Ni-P alloys. By subjecting the specimens to surface etching followed by a succession of heating and cooling cycles, they decreased heterogeneous nucleation and were thus able to make glassy ingots of $Pd_{40}Ni_{40}P_{20}$ with a diameter of 5 mm. In 1984, the Turnbull group [20] could extend the critical casting thickness up to 10 mm by processing the Pd–Ni–P melt in a boron oxide flux. The Pd-Ni-P system may be considered as the first bulk metallic glass to be developed.

In the late 1980s, the Inoue group in Tohoku University of Japan investigated the rare earth materials with Al and Fe metals. They found exceptional glass forming ability in La-Al-Ni and La-Al-Cu alloys system [21]. The cylindrical samples with diameters up to 5 mm or sheets with similar thicknesses were made fully glassy in the $La_{55}Al_{25}Ni_{20}$ alloy by casting into Cu molds, and later the $La_{55}Al_{25}Ni_{10}Cu_{10}$ alloy was fabricated with a diameter up to 9 mm by the same method.

In 1991, the Inoue group developed glassy Mg–Cu–Y and Mg–Ni–Y alloys with the largest GFA obtained in $Mg_{65}Cu_{25}Y_{10}$ [22]. At the same time, the Inoue group developed a family of Zr-based Zr–Al–Ni–Cu alloys exhibiting a high GFA and thermal stability. The critical casting thickness was raised up to 15 mm and the supercooled liquid region in these alloys was extended to 127 K for the $Zr_{65}Al_{7.5}Ni_{10}Cu_{17.5}$ alloy [23]. In 1997, the Inoue group revisited the $Pd_{40}Ni_{40}P_{20}$ alloy and replaced 30 at% Ni by Cu. As a result, they developed an alloy with a critical casting thickness of 72 mm [24]. The Pd–Cu–Ni–P family is the metallic system with the highest GFA known to date. The critical casting thicknesses of metallic glasses are shown in Figure 2.1. Subsequently, Inoue and his group succeeded in finding new multicomponent alloy systems consisting mainly of common metallic elements and proposed the empirical rules to form bulk metallic glasses with high glass forming ability and lower critical cooling rate. The development of these alloys demonstrated that bulk metallic glass composition were not a laboratory curiosity and could be quite interesting for engineering application.

But because of the cost and heavy weight of Pd metal, the light weight metallic glasses such as Mg, Al, Ti and Zr-based alloys with the aim of improving the specific strength were developed. Recently, researches in the area of bulk metallic glasses are significantly growing. Many researchers are searching for new alloy compositions and investigating the mechanical, structural, thermal stability of these alloys. The development has enabled us to produce bulk metallic glasses with useful properties. Subsequently, it has been found that a BMG matrix containing nanocrystalline phases and exhibiting high tensile strength and good ductility is formed in Zr-Al-Cu-based system and the mechanical properties exceed those of the amorphous phase alloys [25]. It could expect that the more and more investigators pay attentions on the amorphous and nanocrystalline alloys in the future.

2.2 The evolution of fabrication methods of amorphous alloys

The fabrication methods of amorphous alloys could be divided into the following three types: (1) from gas state to solid state: sputtering and vacuum evaporation; (2) from liquid state to solid state: splat quenching method, single and two-roller quenching process, chill block melt spinning process (CMBS), planar flow casting process (PFC), spray forming process, conventional metallic mold casting method and high pressure die casting method; (3) from solid state to solid state: ion implantation, ion beam mixing, mechanical alloying (MA) and accumulative roll bonding (ARB) [1].

The liquid quenching method operated at the cooling rate of $10^3 \sim 10^8$ K/s is the major method widely applied to fabricate the different types of amorphous alloys such as powders, wires, ribbons and bulk forms. The process of the liquid quenching method is that the alloys are first heated to the melted condition, after melting homogeneously, the alloy are poured or injected into the mold with high cooling rate to fabricate the amorphous alloys.

The fabrication of amorphous alloy started with from the splat quenching method by Klement et al. [17] on the $Au_{75}Si_{25}$ alloy systems in 1960. This is recognized to be the first report of formation of amorphous alloys by quenching the liquid, as shown in Figure 2.2. However, this method could not produce the uniform shape and size of the amorphous alloys. In 1970s, these limitations of amorphous alloys have been removed by the two roller technique due to Chen and Miller [26], as shown in Figure 2.3. This method is one in which uniform long samples are produced due to flattening out quenching of dropped alloys between two rotating wheels. It is potentially continuous processes to be applied to thin solidified films or foils.

In 1976, the chill block melt spinning method (CMBS) was developed by Liebermann and Graham [27], as shown in Figure 2.4. The method of CMBS involves the formation of a melt jet by the expulsion of a molten alloy through an orifice and the impingement of this jet against a rapidly moving substrate surface. The puddle which results from continuing impingement of the melt jet, serves as a local reserver from which ribbon is continuously formed and chilled. Among various rapid solidification processes, the single roller chill block melt spinning is the most popular method, due to its simplicity in fabrication and effectiveness in producing the rapidly solidified ribbons.

In 1980, Narasimhan and coworkers [1] developed the planar flow casting (PFC) process for the fabrication of rapidly quenched tapes in which the nozzle is held very close to the moving substrate surface, as shown in Figure 2.5. The major difference between CBMS and PFC is that the nozzle of PFC process is brought closer to the quenching wheel so that the melt puddle is more stable to suppress oscillation of the puddle. The PFC process not only enhances the stability of the process but allows a better control of the ribbon dimension. The PFC process improves the quality of amorphous ribbons and also makes wider amorphous ribbons easily.

Until 1991, Inoue et al. [5] succeeded in fabricating the bulk metallic glass in Mg-Cu-Y alloy system with a diameter of 4 mm by copper mold casting method. Next year, the same group [6] succeeded in producing the $Mg_{65}Cu_{25}Y_{10}$ bulk metallic glasses with increased more the diameter up to 7 mm by using high-pressure die casting method. The bulk metallic glass could expand the application area further by eliminating limitation of amorphous alloy in size.

2.3 The system of bulk amorphous alloys

So far, a large number of bulk amorphous alloys have been reported. The alloy system of bulk metallic glasses could be divided into two main types, as shown in Table 2.1 [28]. Table 2.1 summarizes the types of bulk amorphous alloy systems reported to date and the calendar years when details of each alloy system were published. Generally, the bulk amorphous alloys can be separated into nonferrous and ferrous alloy systems. The nonferrous alloy systems include Mg-Ln-M (Ln = lanthanide metal, M = Ni, Cu or Zn) , Ln-Al-TM (TM = VI~VIII group transition metal), Ln-Ga-TM, Zr-Al-TM, Zr-Ti-Al-TM, Ti-Zr-TM, Zr-Ti-TM-Be, Zr-(Nb, Pd)-Al-TM, Pd-Cu-Ni-P, Pd-Ni-Fe-P, Pd-Cu-B-Si, and Ti-Ni-Cu-Sn systems. The ferrous alloy systems involve Fe-(Al, Ga)-metalloid (P, C, B, Si, Ge), (Fe, Co, Ni)-(Zr, Hf, Nb)-B, Fe-Co-Ln-B, and Ni-Nb-(Cr, Mo)-(P,B) alloys.

It is observed that the ferrous alloy systems have been found during the last four years after the synthesis of the nonferrous alloy systems. The alloy components are classified into five categories, as summarized in Table 2.2 [28]. The first group consists of ETM (or Ln), Al and LTM as exemplified for Zr-Al-Ni and Ln-Al-Ni systems, where ETM is IVB~VIB Group Transition Metal and LTM is VIIB~VIIIB Group Transition Metal. The second group is composed of LTM, ETM and metalloid as indicated by Fe-Zr-B and Co-Nb-B systems. The third group is LTM (Fe)-(Al, Ga)-metalloid systems, and the fourth group is indicated by Mg-Ln-LTM and ETM (Zr, Ti)-Be-LTM systems. However, the fifth systems as Pd-Cu-Ni-P and Pd-Ni-P systems are composed only of two kinds of group element (LTM and metalloid), which are different from the combination of the three types of group elements for the alloys belonging to the four previous groups.

It is noticed that the bulk metallic glasses could be produced in many important engineering alloy systems, such as Fe-, Co-, Ni-, Ti-, Zr- and Mg-based amorphous alloys. In addition, so far, the maximum diameter of bulk metallic glasses done by the investigators worldwide tends to increase in the order of Pd-Cu > Zr > Mg or Ln > Fe > Ni > Co or Ti systems.

2.4 The factors influencing the glass forming ability

Amorphous alloys could be produced by rapid quenching from the melt liquid for metallic glasses when the quenching rate exceeds its critical cooling rate. Glass forming ability (GFA), as related to the ease of devitrification, is very crucial for understanding the origins of glass formation and also important for designing and developing new bulk metallic glasses. The GFA of an alloy is evaluated in terms of the critical cooling rate (R_c) for forming metallic glasses, which is the minimum cooling rate necessary to keep the melt amorphous without any precipitation of crystals during the solidification process. The smaller R_c, the higher the GFA of an alloy system should be. However, R_c is a parameter which is difficult to evaluate precisely. So far, a large number of efforts have been devoted to searching for a simple and creditable gauge for quantifying GFA for metallic glasses. As a result, many criteria have been proposed to describe the relative GFA of bulk metallic glasses on the basis of the characteristic temperatures measured by differential thermal calorimetry (DSC) or differential thermal analysis (DTA).

The most extensively used criterion is the reduced glass transition temperature, T_{rg} [29] (= T_g/T_l, where T_g is the glass transition temperature and T_l is the liquidus temperature) and the supercooled liquid region, ΔT_x (= T_x-T_g, where T_x is the onset crystallization temperature and T_g is the glass transition temperature). As proposed by Lu et al. [30], T_{rg} shows a better correlation with GFA than that given by T_g/T_m for bulk metallic glasses (T_m is the solidus temperature). Usually the ΔT_x and T_{rg} are used as indicators of the GFA for metallic glasses. The tendency for R_c to decrease with increasing T_{rg} is shown in Figure 2.6. From the view point of T_{rg} (= T_g/T_l), T_l is dependent on composition, selecting a proper concentration close to the deep eutectic point is useful for the probability of being able to cool fast through the supercooled liquid region without any occurrence of crystallization, i.e., the GFA of alloy would be increased. As to another parameter ΔT_x (= T_x-T_g), the thermal stability of alloy could be increased by increasing T_x, i.e., a good thermal stability for amorphous alloy with a wide ΔT_x indicates that the amorphous alloy has the superior resistance against the crystallization from the supercooled liquid while heating. Figure 2.7 shows that R_c decreases with increasing ΔT_x so that the size of amorphous alloys would be increased.

Although both ΔT_x and the ratio T_g/T_l are used as indicators of the GFA for metallic glasses, they did show contrasting trends versus GFA in many alloy systems. Waniuk et al. [31] confirmed that T_g/T_l value is correlated well with GFA in Zr–Ti–Cu–Ni–Be alloys whereas the supercooled liquid range, ΔT_x, has no relationship with GFA in the least. Those glassy compositions with the largest ΔT_x are actually the poorest glass formers in the system. Inoue et al. [32] also proved that the bulk glass forming ability is more closely associated with T_g/T_l values in Cu-Zr-Ti ternary systems rather than ΔT_x. On the other hand, it was found that the ratio T_g/T_l is not reliable enough to infer relative GFA in $Pd_{40}Ni_{40-X}Fe_XP_{20}$ (X = 0 to 20) [33], and $Mg_{65}Cu_{15}M_{10}Y_{10}$ (M = Ni, Al, Zn and Mn) [34] alloy systems. On the contrary, ΔT_x was claimed to be a reliable and useful criterion for the optimization of bulk glass formation in these systems.

Hence, a new criterion for critical cooling rate and critical thickness to reflect the GFA of bulk metallic glasses was recently proposed by Lu and Liu [35]. The new parameter γ (= $T_x / (T_g + T_l)$) was defined for inferring the relative GFA among bulk metallic glasses. The definition of the parameter of γ is shown in Figure 2.8. The summary of ΔT_x, T_{rg}, γ, critical cooling rate R_c and critical section thickness Z_c obtained by DSC and DTA for various alloy systems is listed in Table 2.4. Regardless of alloy system, the relationship between γ and the critical cooling rate R_c (K/s) as well as critical section thickness Z_c (mm) has been formulated as follows:

$$R_c = 5.1\text{x}10^{21}\exp(-117.19\gamma), \tag{2-1}$$

$$Z_c = 2.8\text{x}10^{-7}\exp(41\gamma). \tag{2-2}$$

Note that these two equations can be utilized to estimate R_c and Z_c when γ is measured readily from DSC or DTA measurements. The new parameter γ reveals that a stronger correlation with GFA than T_{rg} and has been successfully applied to glass formation in the bulk metallic glass systems.

2.5 The empirical rules for the synthesis of amorphous alloys

Since the discovery of amorphous alloys, a number of attempts have been made to understand the mechanism of amorphization in order to predict alloy composition with better glass forming ability. So far, there are many various methods to produce bulk metallic glasses, but the investigators worldwide gradually attempt to understand that the correct designed alloy composition system would lead to metallic glasses with critical cooling rate as low as 1-100 K/s. As proposed by Inoue [28], three empirical rules have been developed for designing alloy composition to fabricate the bulk metallic glass. These are (1) multicomponent systems consisting of more than three elements; (2) significant difference in atomic size ratios above 12% among the three main constituent elements; (3) negative heats of mixing among the three main constituent elements. If there are more than three different elements mixed together and the difference in atomic size is large above 12%, the atomic configuration tends to form the high dense random packing, as shown in Figure 2.9. The larger heats of mixing for constituent elements could contribute to stabilization of the liquid phase by changing the local atomic structure. The alloys with these three empirical rules would have a good GFA to form metallic glass.

As summarized in Table 2.3, in a new type of supercooled liquid with a higher degree of dense randomly packed atomic configurations, new local atomic configurations and long-range homogeneous atomic configurations, the system will have high solid/liquid interfacial energy which is favorable for the suppression of nucleation and growth of a crystalline phase. The new type of liquid can have the difficulty of atomic rearrangement, leading to a decrease of atomic diffusivity and an increase of viscosity. Therefore, the new liquid can have high T_g. In any event, the multicomponent alloys with the three empirical rules always have very deep eutectic point with low melting temperatures, leading to the appearance of high T_{rg} value.

Although these empirical rules are certainly useful for selecting multicomponent alloy system to form amorphous alloys, the development of new amorphous alloys is still a very time-consuming process. In order to identify good glass forming compositions, it is required to experimentally map out the glass forming ability of every single composition in a given alloy system. In multicomponent systems, hundreds of alloy compositions have to be fabricated and evaluated for glass formation. Therefore, finding a more specific criterion for easy glass forming alloy systems would be very beneficial.

Furthermore, there are many other empirical criteria for the glass forming ability. Egami [36] suggest a correlation between atomic size and its concentration in certain metallic glasses. Shek et al. [37] have proposed that the composition of metallic glasses and their crystalline counterparts should possess a constant value of e/a (the average valence electron number per atom). Fang et al. [38] also have proposed that an empirical criterion between bond parametric functions that comprises of electronegativity difference and atomic size parameters to the relationship and width of the supercooled liquid region of Mg-based bulk metallic glasses, as summarized in Figure 2.10. Recently, Chen et al. [39] introduced atomic size and e/a ratio as two criteria to find the best bulk metallic glass forming composition. The electronegativity has also been introduced to explain the glass forming ability of Al- and Mg-based alloys, showing nearly linear relationship with glass forming ability.

Besides these three empirical rules, the specific composition around the eutectic point is an important factor for the multicomponent alloys to form amorphous phases. Comparing the quenching of composition 1 and 2 in Figure 2.11, from the view point of composition 1, the melt would pass through the larger the temperature range by quenching, leading to the probabilities of crystallization before reaching T_g. On the other word, since composition 2 is around the deep eutectic point, i.e., it has the smallest temperature interval between the liquidus and T_g, the melt could maintain liquidus state to lower temperature and immediately transform from liquid to solid to form amorphous alloy by quenching. Hence, the temperature around the deep eutectic point would cause lower T_l so that the GFA would be enhanced.

As proposed by Wang et al. [13] and coworkers have proposed that the criteria of bulk metallic glass formation in MgCu-based alloys. According to the empirical bulk metallic glass formation criteria [28], the bulk glass forming alloys should satisfy: (1) the multicomponent alloy systems consist of more than three elements, (2) there is a significant difference, (> 12%), in the atomic size ratios of the major constituent elements, (3) negative heats of mixing occur among the major elements and finally (4) alloy compositions need to be close to the deep eutectic point. As proposed by Wang et al. [14], a series of novel $Mg_{65}Cu_{25}RE_{10}$ bulk metallic glasses (RE = rare earth elements such as Gd, Nd, Sm, Dy), satisfying these rules with different critical diameters and near eutectic composition, are obtained. It is found that the glass forming ability in the Mg-Cu-RE alloys strongly depends on atomic size and electronegativity of the alloying RE elements.

2.6 The characterization of amorphous alloys

The amorphous alloys have various properties which are superior to the traditional crystalline alloys due to their unique structure. Table 1.1 summarizes the fundamental properties and application fields of bulk amorphous and nanocrystalline alloy. The various properties are described below:

2.6.1 Mechanical properties

The superior mechanical properties of bulk metallic glasses are the most promising characteristics for applications. Since the atomic random arrangement configuration and dense packing structure, when the applied stress is on the amorphous alloys, the amorphous alloys only allow limited atomic displacements to resist deformation. Due to the absence of dislocation mechanisms for plastic deformation, the amorphous alloys are always high strength materials.

The bulk metallic glasses have unique mechanical properties which are different from those of the crystalline alloys, i.e., the bulk metallic glasses have higher tensile strength and lower Young’s modulus and the difference reaches about three times [3]. The relation between tensile fracture strength (σ_f), Vickers hardness (H_v) and Young’s modulus (E) for the various bulk metallic glasses is shown in Figure 2.12, together with the data on the conventional crystalline alloys. The bulk metallic glasses have high σ_f of 840-2100 MPa combined with E of 47-102 GPa, depending on alloy compositions [28]. Hence, the bulk metallic glasses tend to exhibit higher σ_f, higher H_v and lower E than those of any kinds of crystalline alloys.

The three-point bending flexural stress and deflection curves of the Zr-Al-Ni-Cu and Zr-Ti-Al-Ni-Cu bulk amorphous alloys have been measured [40]. These bulk amorphous alloys have high bending flexural strength values of 3000-3900 MPa which are 2.0-2.5 times higher than those for crystalline Zr- and Ti-based alloys. Figure 2.13 summarizes the bending and rotating beam fatigue strength as a function of fatigue cycle up to failure for the bulk amorphous $Zr_{65}Al_{10}Ni_{10}Cu_{15}$ [41] and $Pd_{40}Cu_{30}Ni_{10}P_{20}$ [42] alloys, respectively, together with the data under tensile stress conditions for various melt spun amorphous ribbons. It is confirmed that the present Zr- and Pd-Cu-based bulk metallic glasses have good combination of various mechanical properties, which could not be obtained for conventional crystalline alloys.

2.6.2 Magnetic properties

Applications of magnetic glasses are mainly based on their superior soft magnetic properties. Sensors for electronic article surveillance have become a large application of amorphous materials. Thin sheets of glassy materials are first produced by melt spinning and subsequently annealed, which results in the formation of nanocrystals in a glassy matrix. These nanocomposites still sustain their soft magnetic properties, but have a higher saturation magnetization and lower magnetostriction than the purely amorphous base materials. The most famous example is an alloy with the tradename FINEMET [43], which is a Fe-rich Fe-Si-B alloy with a small addition of Cu and Nb. The use of thin sheets in high frequency applications is of advantage, since eddy currents can be reduced.

Thin ribbons of magnetic nanocomposites and purely metallic glasses are currently used in transformer cores, in magnetic sensors, and for magnetic shielding. Although some magnetic bulk glasses have recently been discovered, so far none of these materials show promising applications. The difficulty in the development of magnetic bulk glasses result from the fact that ferromagnetic elements like Fe, Co, Ni, and Gd are prone to oxidation, which increases the probability for heterogeneous nucleation. It was shown that the nucleation rate in Fe–Ni–P–B (Metglass) alloys can be reduced by four orders of magnitude when heterogeneous nucleation is minimized by the use of fluxing techniques [44]. Generally, the types of magnetic amorphous alloy systems could be divided into categories: TM-TM and TM-M (TM = Fe, Co, Ni, Zr, Hf, etc; M: B, C, Si, P, Ge, etc) systems.

2.6.3 Chemical properties

When bulk metallic glasses for their good static and dynamic mechanical properties are used as structural materials, it is essential for the bulk amorphous alloys to have good corrosion resistance in various kinds of corrosive solutions. Due to the homogeneous single phase structure which is lack of grain boundaries, dislocations and other defects in crystals, the amorphous alloys have superior corrosion resistance. In addition, the corrosion resistance of amorphous alloy could be improved by adding some kinds of corrosive solute.

The corrosion resistance is remarkably improved by the dissolution of Nb or Ta. Inoue et al. [45] have proposed that the corrosion resistance of melt-spun amorphous alloys was examined in Zr-TM-Al-Ni-Cu (TM=Ti, Cr, Nb, Ta) systems in HCl and NaCl solutions and it is found that the Nb- and Ta-containing amorphous alloys exhibit good corrosion resistance in their solutions at room temperature. The corrosion resistance is largest for the Nb-containing alloy, followed by the Ti-containing alloy and then the Zr-Al-Ni-Cu alloy. The corrosion resistance of the Nb-containing alloy is also superior to that of the pure Zr metal, indicating the remarkable effectiveness of Nb addition on the improvement of corrosion resistance even in the NaCl solution.

2.6.4 Other properties of amorphous alloys

Recently, the Zr–Al–Ni–Cu bulk metallic glasses with a wide supercooled liquid region before crystallization were found to exhibit a distinct plateau stage in the hydrogen pressure–concentration–isotherm relation, though the desorption ratio of hydrogen gas is very low (15%) [46]. It has subsequently been found that the desorption ratio remarkably increases by choosing Mg-based amorphous alloys and desorption ratio reaches approximately 100% [47]. It is therefore said that Mg-based bulk amorphous alloys are good candidate for hydrogen storage materials.

On the other hand, the Pd-based bulk metallic exhibits very high efficient ratios for the generation of chlorine gas as an electrode material [48]. The high efficiency above 90% remains unchanged even after 500 cycles, though the efficiency of the commercial pure Pt crystal decreases significantly after 20 cycles. The remarkable improvement of the generation efficiency of chlorine gas has already enabled us to use the Pd-based bulk amorphous alloy as a practical electrode material for the generation of chlorine gas.

2.7 The deformation mechanisms of amorphous alloys

Defect-free bulk metallic glasses exhibit different mechanical properties as compared with their crystalline counterparts. It is of great interest to study and understand the mechanical properties and deformation behaviors of BMGs, especially the fracture characteristics and the deformation mechanisms. Since 1970s, the mechanical properties of amorphous alloys have been investigated [49].

It is known that the crystalline alloy is subjected to elastic deformation, followed by yielding, plastic deformation and then final fracture. It is recognized that the feature of the amorphous alloys appeared in their stress-strain curves lacks sufficient plastic deformation, as shown in Figure 2.14. Generally, the plastic deformation for amorphous alloys is separated into two types: one is slight plastic deformation with slight work hardening and the other is distinct plastic deformation with serration. The serration phenomenon occurred before final fracture indicates the interaction of shear band deformation.

The atomic configuration of the amorphous alloys is different from the crystalline alloys. Because of the dense packing structure and irregular arrangement of atoms, when the stress is applied, the amorphous alloy only allows small displacement of atoms, as shown in Figure 2.15 [50]. In order to deform the amorphous alloy, a larger applied stress would be needed so that the clusters of atoms tend to move together like a band. Hence, the propagation of shear bands leads to the deformation of the amorphous alloy. Furthermore, the serration phenomenon is due to the interaction of shear bands from multiple directions causing the plastic phenomenon of the amorphous alloys.

As proposed by Inoue et al. [16], the Ni-containing $Mg_{75}Cu_5Ni_{10}Gd_{10}$ amorphous alloy exhibits a distinct yield under compressive loading, followed by plastic strain with serration phenomenon, which is different from that for the $Mg_{75}Cu_{15}Gd_{10}$ alloy, as shown in Figure 2.16. Figure 2.17 shows that the compressive fracture surface appearance of the two glass alloys. The fracture surface of the $Mg_{75}Cu_{15}Gd_{10}$ glassy alloy consists of smooth region resulted from shear sliding. However, the fracture surface of the $Mg_{75}Cu_{5}Ni_{10}Gd_{10}$ glassy alloy consists of mainly the vein-like patterns. The serration phenomenon indicates the occurrence of the plastic deformation of the amorphous alloys by the generation and propagation modes of inhomogeneous shear bands.

Over the last decade, several studies related to the deformation behavior of BMGs have been performed. Xiao et al. [51] studied the effect of the strain rates on the fracture surface morphologies of Zr-based BMGs by tension testing. The fracture surface morphology of the $Zr_{52.5}Al_{10}Ni_{10}Cu_{15}Be_{12.5}$ BMG under tension at low strain rates is shown in Figure 2.18. As proposed by Xiao and his workers [51], the typical cleavage veins appear on the fracture surface of the glassy sheets, which could be explained by a localized shear mechanism. The origin of fracture seems to be the center of the shear band as shown on the right photo of Figure 2.18. Once the localized shear bands form, they would rapidly propagate around with being exerted an applied force. The encounter of the neighboring shear bands results in the formation of ridgeline. The ridgelines of shear bands are ultimately torn off, and cause catastrophic failure. Figure 2.19 shows that the fracture surface morphologies of the $Zr_{52.5}Al_{10}Ni_{10}Cu_{15}Be_{12.5}$ BMG at high strain rates under tensile deformation. It is seen that the fracture features are obviously changed at high strain rates. The morphologies that appear on the failure surface are almost made up of microvoid-coalescence dimples, which could be explained by a localized melting mechanism.

Kusy et al. [52] have investigated the fracture morphologies of the Zr-based

BMG-matrix-composites (BMGCs) and Cu-based BMG under compression testing. The compression fracture surfaces of both Zr-based BMGCs and Cu-based BMGs reveal a mixture of three different distinct patterns: vein-like pattern, intermittent smooth regions and river-like pattern, as shown in Figures 2.20 and Figure 2.21. Furthermore, randomly distributed transversal steps on the fracture plane are also revealed. It is in contrast to previous studies that a characteristic vein-like pattern is considered a unique feature of the fracture of BMGs under compression testing. The presence of different fracture features indicates that the development of the fracture plane occurs in a stepwise mode.

So far, the worldwide researchers extensively investigate on the mechanical properties of amorphous alloys or amorphous-matrix-composites, such as Xiao worked on the tension testing [51], Lu and Liaw made efforts on compression testing [52-53], and Nieh is devoted to indentation experiment [54]. Several studies were reported to reveal the mechanisms of strain localization, plastic deformation, crack initiation and propagation. At the present day, it is a main stream to concentrate much attention on the investigations on the mechanical properties of BMGs and BMG-matrix-composites.

Chapter 3 Experimental procedures

The multicomponent alloys with the designed compositions of $Mg_{65}Cu_{25}Gd_{10}$ and $Mg_{65}Cu_{15}Ag_{10}Gd_{10}$ are researched in this study. Figures 3.1-3.6 show the related binary phase diagrams of Mg-Cu, Mg-Gd, Mg-Ag, Cu-Gd, Cu-Ag and Gd-Ag related to the Mg-Cu-Gd-Ag system. Furthermore, the amorphous ternary graphics of the Mg-Cu-Y system is shown in Figure 3.7, but the ternary phase diagram of the Mg-Cu-Gd system is not available now.

The $Mg_{65}Cu_{25}Gd_{10}$ and $Mg_{65}Cu_{15}Ag_{10}Gd_{10}$ bulk metallic glasses are fabricated by the copper mold casting method. The microstructure and amorphous nature of the samples are examined by X-ray diffraction (XRD), and a scanning electron microscopy (SEM) with energy dispersive X-ray spectrometry (EDS). The thermal stability of the $Mg_{65}Cu_{25}Gd_{10}$ and $Mg_{65}Cu_{15}Ag_{10}Gd_{10}$ alloys is examined by using a differential scanning calorimeter (DSC). The thermal mechanical properties of the $Mg_{65}Cu_{25}Gd_{10}$ and $Mg_{65}Cu_{15}Ag_{10}Gd_{10}$ bulk metallic glasses are evaluated by using thermal mechanical analysis (TMA) and dynamic mechanical analysis (DMA). The mechanical properties of the $Mg_{65}Cu_{25}Gd_{10}$ BMG in term of compression testing are conducted by using an Instron 5582 universal testing machine. The flow chart of the experimental procedure is shown in Figure 3.8.

3.1 Materials

The elements used in this study were purchased from Well Being Enterprise Co., Ltd, Taipei, Taiwan. Moreover, the purities of the elements are of concern; that magnesium is as pure as 99.9%, copper is as pure as 99.99%, gadolinium is as pure as 99.9% and silver is as pure as 99.99%. The constituent content of alloy system in this study is listed in Table 3.1 and the data related to the elements in this study are also listed in Table 3.2.

3.2 Sample preparation

3.2.1 Arc melting

Since the boiling point of Mg is close to or lowers than the melting points of Cu, Y, Gd and Ag, it is not suitable to arc melt the Mg with other elements. The arc melting is first performed to prepare the master ingots of Cu-Gd binary or Cu-Gd-Ag ternary alloy in an arc furnace under an argon atmosphere. The applied instrument is the Centorr Series 5 Bell Jar Single Arc Furnace, as shown in Figure 3.9. The operation current of the device is about 200 ~ 300 A.

Before starting the arc melting process, in order to avoid the occurrence of crystallization due to oxygen impurities, the argon gas needs to be continuously purged into the arc furnace to flush the oxygen and then to achieve a low oxygen atmosphere environment inside the furnace. The process should be repeated several times to ensure high vacuum inside the furnace to protect from oxidization. In order to increase the heat exchange rate, cold water needs to be poured into and flowing through the bottom of the copper mold. Finally, the elements of alloy placed on the bottom of the copper mold will be melted by a high voltage arc under a Ti-gettered argon atmosphere in a water-cooled copper mold. It should be repeated several times for alloy ingots to confirm compositional homogeneity.

3.2.2 Induction melting

The $Mg_{65}Cu_{25}Gd_{10}$ and $Mg_{65}Cu_{15}Ag_{10}Gd_{10}$ alloys are first prepared with induction melting by a conventional copper mold method under an argon atmosphere. After the Cu-Gd or Cu-Gd-Ag alloy ingots are melted several times by arc melting, the Cu-Gd or Cu-Gd-Ag alloy ingots are then remelted with pure Mg in a Fe crucible placed in an induction furnace and then poured into the rectangular-shaped Cu mold under an argon atmosphere. The cold water needs to be poured into and flowing through the Cu mold to reach the high cooling rate so that increase the heat exchange rate to make the liquid alloy rapidly quenched. The process of beforehand casting could ensure complete mixing between elemental components and is favorable to fabricate the BMGs by injection casting method due to the master alloys prepared by first casting could decrease the melt temperature during injection casing.

In addition, in order to suppress the generation of Mg vapor and the loss of the constituent accuracy, the argon atmosphere is maintained at 1 atm passive pressure. And the crucible needs to be sprayed a thin boron nitride layer to prevent the alloy from interacting with the crucible at high temperatures.

3.2.3 Injection casting

The master bulk metallic glass rods of $Mg_{65}Cu_{25}Gd_{10}$ and $Mg_{65}Cu_{15}Ag_{10}Gd_{10}$ will be fabricated by using a conventional copper mold casting method in an argon atmosphere. This method is a generally recognized the most convenient way to fabricate the bulk metallic glass.

The processing procedures are similar to the first casting method. First, the

Mg-Cu-Gd-Ag master alloys fabricated by first casting are taken appropriate amount and placed in a quartz tube, and the quartz tube needs to spray a thin layer of boron nitride to avoid the interaction between alloy and quartz tube at high temperatures. The quartz tube is placed in an induction furnace controlled by the high frequency system, and the argon atmosphere is added to 1 atm in order to suppress the generation of magnesium vapor. Similar to the arc melting process, the gas pouring and flushing step is performed several times to ensure the high vacuum before injection casting.

Then the alloys are melted homogeneously by induction melting in an induction furnace under the argon atmosphere, the melt is injected an argon atmosphere into a copper mold that has internal rod-shaped cavities to fabricate the Mg-Cu-Gd-Ag bulk metallic glasses. The $Mg_{65}Cu_{25}Gd_{10}$ and $Mg_{65}Cu_{15}Ag_{10}Gd_{10}$ bulk metallic glass rods with the different diameters from 3 to 8 mm are prepared.

3.3 Property measurements and analyses

3.3.1 X-ray diffraction

The amorphous nature of the $Mg_{65}Cu_{25}Gd_{10}$ and $Mg_{65}Cu_{15}Ag_{10}Gd_{10}$ BMG rods fabricated by the conventional copper mold casting methods will be examined by X-ray diffraction (XRD). The SIEMENS D5000 X-ray Diffractometer with Cu K_α radiation (λ = 1.5406 $\overset{o}{A}$) at 40 kV and 30 mA, equipped with 0.02 mm graphite monochrometer, is utilized. The range of the diffraction angle 2θ is within 20^o to 80^o at scanning rate of 0.1^o per four seconds. To verify the amorphous structure of the alloy rod, the rod is cut from the center to expose the center cross-section portion for XRD.

3.3.2 Qualitative and Quantitative constituent analysis

In order to identify the constituent component and confirm the composition percentage of the bulk metallic glasses, the samples are characterized with a scanning electron microscope (SEM) with energy dispersive X-ray spectrometer (EDS). The cross-sectional surface of alloys cut from bulk metallic glass rods is selected to examine the quantity of the designed compositions by EDS.

3.3.3 DSC thermal analysis

Glass forming ability parameters associated with the glass transition temperature (T_g), the crystallization temperature (T_x), the supercooled liquid region (ΔT_x), the solidus temperature (T_m) and the liquidus temperature (T_l) are determined by differential scanning calorimeter (DSC). In this study, the thermal behavior of the Mg-Cu-Gd-Ag bulk metallic glasses is analyzed using a SETARAM DSC131 differential scanning calorimeter under an argon atmosphere, at the constant heating rates of 0.33 K/s, and 0.67 K/s and the heating range from 300 K to 900 K.

In addition, in order to prevent the oxidation and magnesium vapor liberated during heating from polluting the chamber, the samples are placed on the Cu crucibles and tightly sealed with nickel ring in a protective argon atmosphere. The pre-presence air in the DSC chamber is flushed by pure Ar and it is keep the positive Ar pressure while heating

3.3.4 Density measurement

Form the simple and reliable points of view, the well-know principle of Archimedes is used as an appropriate means to measure the density of amorphous alloys. In this technique, the specimen contained in a vessel is weighted in air and gets a value of mass W_1. Then, the specimen is weighted in a liquid of known density β and gets a value of mass W_2. Therefore, the density of amorphous alloy can be evaluated by the following equation :

$$\rho = \frac{W_1}{W_1 - W_2/\beta} \quad . \tag{3-1}$$

The atomic configurations of amorphous alloys are different from those for the crystalline alloys. It is expected that the short-range atomic configuration changes the density of the new amorphous alloys. Normally, the densities would increase when amorphous phase transform into structural relaxation or crystallization.

3.3.5 Microhardness testing

The microhardness testing of the samples are conducted using a SHIMADZU HMV-2000 Vicker’s Microhardness tester. The samples cut from the BMG rods to expose the center cross-section portion and the samples need to be ground by silicon carbide abrasive papers with water before the microhardness testing. The tests apply a load of 200 g and a duration time of 15 seconds; the hardness values of each sample are averaged from 10 datum points chosen randomly. The microhardness data on the Mg-Cu-Gd-Ag BMGs could be used to imply whether the substitution of Cu by Ag would cause a dense atomic structure or not, as compared with the Mg-Cu-Gd amorphous alloy.

3.3.6 Compression testing

The mechanical properties of the bulk metallic glasses in term of compression testing are reported in this study. The compressive strength, observed elastic modulus and compressive strain will be evaluated by using an Instron 5582 universal testing machine and the cylindrical specimens fabricated by the Cu mold casting method with a diameter of 4 mm and different heights. The compression specimens are cut from the $Mg_{65}Cu_{25}Gd_{10}$ and $Mg_{65}Cu_{15}Ag_{10}Gd_{10}$ BMG rods with height to diameter ratios (h/d) of 2:1 and 1:1, respectively. In addition, in order to verify the effect of thin size on the mechanical properties of BMGs, the specimens with the diameter of 4 mm and as thin as height of 2 and 1 mm also are prepared for compression testing. Hence, room temperature compression tests are conducted on the specimens with various height to diameter ratios from 2:1, 1:1, 1:2 to 1:4.

All cut surfaces are ground by silicon carbide abrasive papers with water and polished. Before the compression specimen is fixed into the crossheads of the Instron machine, the BN are used as lubricant to decrease the friction between test samples and the compression platens. The specimens are compressed between hard BN platens under a displacement control with a strain rate of 5×10^{-4} s^{-1} at room temperature. The fracture surface morphologies of the deformed specimens will be to observe by SEM. In Ag containing Mg-based alloy, it is expected to see if there is any improvement in the strength and ductility.

3.3.7 Thermal mechanical and dynamic mechanical analyzer

The mechanical characterization will also be examined by the Perkin Elmer Instruments Pyris diamond thermomechanical analyzer (TMA) and dynamic mechanical analyzer (DMA). The Pyris Diamond TMA is a combination of the following: (1) thermal stress-strain analyzer used to measure the stress and strain of the samples and display the resulted in terms of time and temperature; and (2) thermomechanical Analyzer used to measure thermal mechanical characteristics such as thermal expansion, thermal contraction and softening.

TMA could measure the change in the dimensions of a sample such as expansion or contraction as a function o temperature, time and force applied to the sample. The sample is held by chucks attached to the sample tube and the probe. Force is applied to the sample, and the resulting changes in sample length are detected by an independently connected differential transformer and core under an inert atmosphere.

DMA could measure changes of rheological behavior under dynamic conditions such as storage modulus, E’, loss modulus, E’’, loss tangent, tanδ (= E’’ / E’) and glass transition temperature (T_g). It could fully analyze the characteristics of elastic, viscous and viscoelastic properties of materials as a function of time and temperature, stress or a combination of these parameters. The glass transition is determined by the maximum peak of the loss modulus curve or the inflection point of storage modulus curve. Generally, the T_g measured by DMA is more precise than that measured by DSC due to the measuring environment is under dynamic condition. In addition, the samples could be analyzed by DMA in various deformation modes, including bending, 3 point bending, tension, compression and so on.

The samples will pre–run test before the actual measurement to confirm an appropriate sample shape. The compression mode will be conducted to analyze the thermal mechanical properties of BMGs at different temperature. Once the test is complete, the position of samples in the measurement range could be displayed. The instrument is maintained under inert atmosphere to protect the chamber from polluting.

3.3.8 Microstructure examination

The fracture surface morphologies of BMG specimens after mechanical testing are also observed by JEOL JSM-6400 scanning electron microscopy (SEM). So far several investigations on uniaxial tension, compression, three point bending, and fatigue were reported to reveal the mechanisms of strain localization, elastic and plastic deformation, crack and initiation and propagation. Hence, the different fracture features after compression testing will be observed in order to study the deformation mechanisms for BMG. In addition, the possible deformation mechanisms in specimens of different geometry shapes will be discussed according to the microstructure observations.

Chapter 4 Results

4.1 Sample preparations

Before injection casting, the $Mg_{65}Cu_{25}Gd_{10}$ and $Mg_{65}Cu_{15}Ag_{10}Gd_{10}$ alloys prepared via first casting by induction melting show that both of the $Mg_{65}Cu_{25}Gd_{10}$ and $Mg_{65}Cu_{15}Ag_{10}Gd_{10}$ alloy ingots reveal very shining part around cast mold wall and the thickness of the shining part measures about 1 to 2 mm. The difference between the amorphousness and crystallization is obviously observed. As the above description, it implies that the $Mg_{65}Cu_{25}Gd_{10}$ and $Mg_{65}Cu_{15}Ag_{10}Gd_{10}$ alloys possess the good glass forming ability to allow us to fabricate bulk metallic glasses with a large critical diameter.

The rods of the $Mg_{65}Cu_{25}Gd_{10}$ and $Mg_{65}Cu_{15}Ag_{10}Gd_{10}$ alloy with different diameters from 3 to 8 mm were fabricated by copper mold casting under an argon atmosphere in ISU University, as shown in Figures 4.1 and 4.2. The surface appearances of injection cast $Mg_{65}Cu_{25}Gd_{10}$ rods with different diameter from 3 to 6 mm and the $Mg_{65}Cu_{15}Ag_{10}Gd_{10}$ rods with the diameter from 3 to 6 mm all show lustrous and smooth surface. This indicates that complete filling of the cavities was obtained during injection casting. In addition, the injection cast $Mg_{65}Cu_{25}Gd_{10}$ rods with the diameter of 8 mm show the coarse surface appearances and a small amount of cavities are observed from the cross-sectional surface. From the cross-sectional view, the injection cast $Mg_{65}Cu_{25}Gd_{10}$ rods with different diameters from 3 to 6 mm all show no obvious pore existence as shown in Figure 4.3, but the 8 mm $Mg_{65}Cu_{25}Gd_{10}$ rods does not. It obviously has different microstructures between the specimens with diameters of 3-6 mm and 8 mm for the $Mg_{65}Cu_{25}Gd_{10}$ rods.

4.2 SEM/EDS observations

The quantity analyses of the injection cast $Mg_{65}Cu_{25}Gd_{10}$ and $Mg_{65}Cu_{15}Ag_{10}Gd_{10}$ rods with different diameters were identified by SEM/EDS. The composition of the injection cast $Mg_{65}Cu_{25}Gd_{10}$ and $Mg_{65}Cu_{15}Ag_{10}Gd_{10}$ rods with the diameter from 3 to 6 mm are confirmed by EDS. It is noted that the polished cross-sectional surface of the injection cast $Mg_{65}Cu_{25}Gd_{10}$ and $Mg_{65}Cu_{15}Ag_{10}Gd_{10}$ BMGs are all analyzed by EDS under low magnifications. As a result from EDS, all the composition of the $Mg_{65}Cu_{25}Gd_{10}$ and $Mg_{65}Cu_{15}Ag_{10}Gd_{10}$ rods are close to the designed composition.

In order to confirm the absence of any crystalline phase over the whole sample, the SEM/BEI composition image are taken from the polished cross-sectional surface of the injection cast $Mg_{65}Cu_{25}Gd_{10}$ and $Mg_{65}Cu_{15}Ag_{10}Gd_{10}$ rods, as shown in Figures 4.4 (a) and 4.5 (a). It could be found that no contrast of any precipitate due to crystallization or non-uniformly melting is seen over the whole sample, indicating the injection cast $Mg_{65}Cu_{25}Gd_{10}$ and $Mg_{65}Cu_{15}Ag_{10}Gd_{10}$ rods show homogeneous microstructure. Furthermore, the mapping image of the injection cast $Mg_{65}Cu_{25}Gd_{10}$ and $Mg_{65}Cu_{15}Ag_{10}Gd_{10}$ rods was examined by SEM. The elements of Cu, Gd and Ag are uniformly dispersed in the Mg matrix, as shown in Figures 4.4 (b) and 4.5 (b). The SEM/BEI and mapping image shows that the Mg, Cu, Gd, and Ag elements of the Mg-Cu-Gd-Ag alloys distribute homogeneously.

4.3 XRD analyses

The glassy structure of the $Mg_{65}Cu_{25}Gd_{10}$ and $Mg_{65}Cu_{15}Ag_{10}Gd_{10}$ alloy rods fabricated by copper mold cast method was identified by XRD. Figure 4.6 shows the XRD patterns of the injection cast $Mg_{65}Cu_{25}Gd_{10}$ alloy rods with diameters from 3 to 6 mm, consisting of a broad diffraction peak characteristic of amorphous structure without any crystalline phases. This indicates the $Mg_{65}Cu_{25}Gd_{10}$ alloy rods are all of a single glassy phase. Furthermore, the XRD pattern of the injection cast $Mg_{65}Cu_{15}Ag_{10}Gd_{10}$ alloy rods with diameters from 3 to 6 mm is shown in Figure 4.7. Only a broad diffused amorphous hump occurs and no obvious crystalline peak is observed in such injection cast $Mg_{65}Cu_{15}Ag_{10}Gd_{10}$ alloy rods.

In addition, Figures 4.6 shows that the XRD pattern of the injection casting $Mg_{65}Cu_{25}Gd_{10}$ alloy rods with a diameter of 8 mm consists of the some sharp diffraction peaks and amorphous diffused hump located at 30^o to 40^o, indicating that this sample exhibits the presence of crystalline phases in the amorphous matrix. The sharp diffraction peaks are identified as the Mg_2Cu phase by JCPDS card in the injection cast 8 mm $Mg_{65}Cu_{25}Gd_{10}$ alloy rod. To sum up the above descriptions, the injection cast $Mg_{65}Cu_{25}Gd_{10}$ and $Mg_{65}Cu_{15}Ag_{10}Gd_{10}$ bulk metallic glasses with the diameters up to 6 mm can be fabricated by conventional copper mold method.

4.4 DSC analyses

The thermal properties of the injection cast $Mg_{65}Cu_{25}Gd_{10}$ and $Mg_{65}Cu_{15}Ag_{10}Gd_{10}$ BMGs were examined by DSC with the heating rates of 0.33 K/s (20 K/min) and 0.67 K/s (40 K/min), as shown in Figures 4.8 and 4.9. The DSC traces with a heating rate of 0.67 K/s for the systems with Cu replaced by Ag in the Mg-Cu-Gd BMGs are systematically combined in Figure 4.10. The glass transition temperature (T_g), the onset crystallization temperature (T_x), the solidus temperature (T_m) and the liquidus temperature (T_l) are all marked by arrows in the DSC traces. All the samples exhibit distinct T_g and T_x, followed by a wide supercooled liquid region and then the exothermic reactions due to crystallization followed by the endothermic reactions due to melt. In addition, the appearance of several exothermic peaks implies that the injection cast $Mg_{65}Cu_{15}Ag_{10}Gd_{10}$ BMGs possesses the complicated crystallization upon heating.

Figure 4.8 shows the DSC traces obtained from the injection casting $Mg_{65}Cu_{25}Gd_{10}$ BMGs with the heating rates of 0.33 K/s and 0.67 K/s. The crystallization exothermic reactions for the $Mg_{65}Cu_{25}Gd_{10}$ BMGs in the DSC curves appear as one single peak, indicating one major phase was induced during DSC heating (namely, the Mg_2Cu). The T_g, T_x, T_m and T_l of the $Mg_{65}Cu_{25}Gd_{10}$ BMGs at a heating rate of 0.33 K/s are 414 K, 482 K, 681 K and 727 K, respectively. Also, the DSC result of T_g, T_x, T_m and T_l of the $Mg_{65}Cu_{25}Gd_{10}$ BMGs at a higher heating rate of 0.67 K/s are 421 K, 490 K, 684 K and 738 K, respectively.

With the replacement of Cu by the Ag addition in the $Mg_{65}Cu_{25}Gd_{10}$ BMGs, the DSC traces are obtained from the injection cast $Mg_{65}Cu_{15}Ag_{10}Gd_{10}$ BMGs with the heating rates of 0.33 K/s and 0.67 K/s, as shown in Figure 4.9. The crystallization reactions for the $Mg_{65}Cu_{15}Ag_{10}Gd_{10}$ BMGs in the DSC curves appear as three exothermic peaks, indicating several phases were induced during DSC heating. The T_g, T_x, T_m and T_l of the $Mg_{65}Cu_{15}Ag_{10}Gd_{10}$ BMGs at a heating rate of 0.33 K/s are 417 K, 461 K, 686 K and 720 K, respectively. The DSC result of T_g, T_x, T_m and T_l of the $Mg_{65}Cu_{15}Ag_{10}Gd_{10}$ BMGs at a higher heating rate of 0.67 K/s are 429 K, 472 K, 688 K and 728 K, respectively. The thermal characteristics of the injection casting $Mg_{65}Cu_{25}Gd_{10}$ and $Mg_{65}Cu_{15}Ag_{10}Gd_{10}$ BMGs at the heating rates of 0.67 K/s are summarized in Table 4.1.

From the DSC summary in Table 4.1, with the Ag addition in the Mg-Cu-Gd BMGs, the T_g increases from 421 K for the $Mg_{65}Cu_{25}Gd_{10}$ BMGs to 429 K for the $Mg_{65}Cu_{15}Ag_{10}Gd_{10}$ BMGs, and then the T_x decreases from 490 K for the $Mg_{65}Cu_{25}Gd_{10}$ BMGs to 472 K for the $Mg_{65}Cu_{15}Ag_{10}Gd_{10}$ BMGs. As a result, the ΔT_x decreases from 69 K for the $Mg_{65}Cu_{25}Gd_{10}$

BMGs to 43 K for the $Mg_{65}Cu_{15}Ag_{10}Gd_{10}$ BMGs. The degradation of ΔT_x for the $Mg_{65}Cu_{15}Ag_{10}Gd_{10}$ BMGs implies that it will reduce the thermal stability in Ag containing BMGs.

The melting behaviors of the injection cast $Mg_{65}Cu_{25}Gd_{10}$ and $Mg_{65}Cu_{15}Ag_{10}Gd_{10}$ BMGs are also determined by using DSC with the heating rates of 0.33 K/s and 0.67 K/s. From the DSC summary of Table 4.1, the onset and offset temperatures of the melting designed by T_m and T_l are 684 K and 738 K for $Mg_{65}Cu_{25}Gd_{10}$ BMGs at the heating rate of 0.67 K/s, or $\Delta T_l = T_l - T_m = 54$ K. The T_m and T_l for $Mg_{65}Cu_{15}Ag_{10}Gd_{10}$ BMGs are 688 K and 728 K at the heating rate of 0.67 K/s, $\Delta T_l = 40$ K. These results indicate that the $Mg_{65}Cu_{15}Ag_{10}Gd_{10}$ BMGs are closer to the eutectic composition.

Thermal properties of the injection cast $Mg_{65}Cu_{25}Gd_{10}$ and $Mg_{65}Cu_{15}Ag_{10}Gd_{10}$ BMGs are combined for compare for the effects of Ag addition, as shown in Figure 4.10. Furthermore, the ratio of the glass transition temperature T_{rg} and the γ value are often used as a parameter to estimate the glass forming ability. From the DSC summary of Table 4.1, the T_{rg} and the γ values for the $Mg_{65}Cu_{25}Gd_{10}$ BMGs at the heating rate of 0.67 K/s are 0.570 and 0.423, respectively. In contrast, the T_{rg} and the γ values for the $Mg_{65}Cu_{15}Ag_{10}Gd_{10}$ BMGs are 0.589 and 0.408, respectively. Although the T_{rg} parameter for $Mg_{65}Cu_{15}Ag_{10}Gd_{10}$ (0.589) is higher than that for $Mg_{65}Cu_{25}Gd_{10}$ BMGs (0.570), recently it is more often to use the γ value to estimate the glass forming ability of BMGs and it is found that the dependence of glass forming ability for BMGs is more precise. According to this argument, the γ value for $Mg_{65}Cu_{25}Gd_{10}$ is higher than that for $Mg_{65}Cu_{15}Ag_{10}Gd_{10}$, indicating that the replacement of Cu by Ag will degrade the glass forming ability. It is obvious that the effects of the replacement of Cu by Ag on the thermal behaviors in the Mg-Cu-Gd-Ag alloys are distinct.

4.5 Density measurements

The simplest method to detect whether the volume is changed is to measure the density. Table 4-2 shows the density results obtained by means of the Archimedean theorem. The $Mg_{65}Cu_{25}Gd_{10}$ BMG has the smaller density value of 3.75 g/cm^3, and the density value for $Mg_{65}Cu_{15}Ag_{10}Gd_{10}$ is 3.94 g/cm^3. As shown in Table 4-2, the density of $Mg_{65}Cu_{15}Ag_{10}Gd_{10}$ is higher than that of $Mg_{65}Cu_{25}Gd_{10}$, consist with the trend for the theoretical value in Table 4-2, indicating that the atomic configuration in $Mg_{65}Cu_{15}Ag_{10}Gd_{10}$ BMG possesses a more densely packed structure.

4.6 Microhardness tests

The hardness of the injection cast $Mg_{65}Cu_{25}Gd_{10}$ and $Mg_{65}Cu_{15}Ag_{10}Gd_{10}$ BMGs are measured by using the HMV-2000 microhardness tester. Ten positions are randomly chosen for each samples, then the Vickers hardness (H_v) are obtained by indenting each sample at the load of 200 g and with the duration time of 15 second.

Figure 4.11 shows the microhardness test results of the injection cast $Mg_{65}Cu_{25}Gd_{10}$ and $Mg_{65}Cu_{15}Ag_{10}Gd_{10}$ BMGs. The replacement of Cu by 10 at% of Ag would raise the H_v level. The H_v value of 232 for $Mg_{65}Cu_{25}Gd_{10}$ BMGs is lower than that of 255 for $Mg_{65}Cu_{15}Ag_{10}Gd_{10}$ BMGs. It could be found that the H_v is sensitive to the addition of Ag. The microhardness results are often considered to reflect more accurately the overall bulk property. The current results suggest that the Ag addition can improve the BMGs hardness. From the DSC results, the higher glass transition temperature implies the stronger bonding force among atoms due to the larger negative heat of mixing in multicomponent systems. Hence, the stronger bonding force among atoms will enhance the ability of material against deformation.

4.7 TMA/DMA analyses

4.7.1 TMA analysis

The variation of the relative displacement (ΔL) for the $Mg_{65}Cu_{25}Gd_{10}$ BMG obtained by TMA operated under the compressive mode at 50 mN stress and a heating rate of 0.17 K/s is shown in Figure 4.12. One can be seen that with increasing temperature, the sample show the tendency to the change in displacement. Before reaching the T_g temperature, the relative displacement is almost constant. However, with increasing loading temperature the relative displacement is enhanced appreciably, especially approaching the T_g temperature when the glass structure becomes viscous matter. The relative displacement is enlarged from -0.1% to –6.3% over the transition temperature interval of ~420 to ~475 K.

It could be more clearly seen from the derivative of the displacement with respect to time or the DTMA curve, also as shown in Figure 4.12. The temperature interval in which a rapid change in displacement occurs is close to the supercooled region of the $Mg_{65}Cu_{25}Gd_{10}$ BMG at a heating rate of 0.17 K/s.

Furthermore, the thermal expansion behavior of the $Mg_{65}Cu_{25}Gd_{10}$ BMG is studied in the temperature range from 350 K to 600 K, as shown in Figure 4.13. Before T_g, the linear coefficient of thermal expansion (CTE) for amorphous solid is α_g = 2.09 x 10^{-6} m/m^{o}C. Above T_x, the CTE for crystal solid is α_c = 5.73 x 10^{-6} m/m^{o}C, suggesting that the CTE is in agreement with the common Mg alloys. Especially, in the temperature range of supercooled liquid, the CTE for viscous flow is α_v = -201.35 x 10^{-6} m/m^{o}C. It is of great interest why the reason for the phenomenon of the negative CTE? Processing deformation or free volume effects? It needs to be studied further in the future.

4.7.2 DMA analysis

The changes of rheological behavior under dynamic conditions such as the storage modulus, E', loss modulus, E'', loss tangent, tanδ (= E'' / E') and glass transition temperature (T_g) are measured by DMA. As shown in Figure 4.14, before reaching the T_g temperature, the elastic modulus is almost constant due to the applied load is too low for the BMGs. The elastic modulus will tend to decrease significantly while the glass structure matter changes to viscous matter for amorphous alloys during heating. Afterwards, the occurrence of crystallization will lead that the viscous matter changes to the crystalline matter, this will make the elastic modulus increase. Hence, the E' decreases at temperature near T_g due to the change into viscous matter and then increases due to the occurrence of crystallization.

The tanδ means that the ability of losing energy for the deformation of sample while heating. The viscous matter is deformed easily, so the tanδ will increase when the temperature reach the T_g, i.e., the softer and weaker matter will cause the larger loss of energy for deformation. From the tanδ curve, the value of tanδ gradually increases when the glass matter changes to viscous matter, followed by gradual decrease as a result of the occurrence of crystallization. The tanδ will tend to the constant after the viscous matter gradually changes to crystalline matter.

4.8 Compression testing

The compressive mechanical properties at room temperature of the injection cast $Mg_{65}Cu_{25}Gd_{10}$ BMGs have been measured by using an Instron 5582 type machine. Compression tests are conducted on specimens with various height to diameter ratios (h/d) from 2:1, 1:1, 1:2 to 1:4.

The compressive stress-strain curve for the injection cast $Mg_{65}Cu_{25}Gd_{10}$ BMGs with the highest h/d ratio of 2:1 (h = 8 mm and d = 4 mm) at strain rate of 5×10^{-4} s^{-1} is shown in Figure 4.15. The compressive fracture strength and fracture elongation are ~806 MPa and ~1.97% for $Mg_{65}Cu_{25}Gd_{10}$ BMG and the plastic strain is almost zero. The $Mg_{65}Cu_{25}Gd_{10}$ BMG shows no evidence of macroscopic yielding and plasticity, as reported for the most Mg-based BMGs. In addition, the compressive stress-strain curves for the injection cast $Mg_{65}Cu_{25}Gd_{10}$ BMGs with various h/d ratios from 2 to 0.25 at a strain rate of 5×10^{-4} s^{-1} are shown in Figures 4.16. With decreasing h/d ratio, the compressive fracture strength and fracture elongation at the strain rate of 5×10^{-4} s^{-1} are ~679 MPa and ~4.15% for specimen with h/d = 1, ~848 MPa and ~11.53% for specimen with h/d = 0.5, and ~911 MPa and ~16.99% for specimen with h/d = 0.25.

As can be seen from Figures 4.16, all samples do not reveal a distinct yielding behavior before fracture. For specimens with higher h/d ratios such as 2:1 and 1:1, the fracture elongation arises from elastic deformation, indicating that the brittle nature of Mg-based BMGs. However, for specimens with lower h/d ratios from 1:2 to 1:4, the stress-strain curves seem to be tougher as compared with the specimens with higher h/d ratios. Hence, the specimen geometry effects will influence the mechanical response of amorphous alloys. The compressive mechanical properties of the $Mg_{65}Cu_{25}Gd_{10}$ BMGs are summarized in Table 4.3.

In this study, the compressive strength and density of the $Mg_{65}Cu_{25}Gd_{10}$ BMG are 806

MPa and 3.75 g/cm^3, respectively. Therefore, the specific strength (strength to density ratio) of the $Mg_{65}Cu_{25}Gd_{10}$ BMG is 215 MPa·cm^3/g, as compared to the commercial AZ91 alloy (147 MPa·cm^3/g). From the industrial needs of developing high strength materials with light weight, the Mg-based BMG is promising for future development of a lightweight structural material with high specific strength.

4.9 Compressive fracture characteristics

The outer appearance and fracture surface morphologies of $Mg_{65}Cu_{25}Gd_{10}$ samples are observed after compression testing by using SEM, as shown in Figures 4.17-4.35. Figure 4.17 shows the angle of the fracture plane inclination for the specimens with the h/d ratio of 2 at a strain rate of 5 x 10^{-4} s^{-1} is ~54^o. Figure 4.18 shows the fracture surface morphology for the specimens with the h/d ratio of 2 after compression testing, from the overview, the fracture surface reveals the brittle fracture. Furthermore, in an enlarged magnification, Figure 4.19 shows that the fracture surface for specimen with the h/d ratio of 2 consists mostly of the cleavage feature characteristics of brittle fracture without apparent vein structures.

In addition, the angle of the fracture plane inclination for the specimens with the h/d ratio of 1 at a strain rate of 5 x 10^{-4} s^{-1} decreases to ~46^o, as shown in Figure 4.20. Figure 4.21 show the fracture surface morphology for the specimens with the h/d ratio of 1 after compression testing, from the overview, the fracture surface reveals the similar features like the specimens with the h/d ratio of 2. However, in an enlarged micrograph (as marked by arrows in Figure 4.21), it is found that the fracture surface for specimen with the h/d ratio of 1 exhibits the mixture features of the cleavage characteristics and vein-like patterns, as shown in Figures 4.22 and 4.23. The characteristic of vein-like patterns is attributed to a local change of viscosity in the fracture along shear band in metallic glasses. According to Figure

4.23, it could show the evidence for shear band propagation during compression testing. The fracture surface morphology for metallic glasses commonly shows the unique feature of vein-like patterns spreading over the fracture surface along the propagation of the shear bands, indicating that the experimental results agree with the amorphous characteristics. Furthermore, Figure 4.23 shows the intermittent fine striation regions like ridge among the vein-like patterns are observed (as marked by arrow), indicating the intermittent gradation of shear bands sliding are contained.

With decreasing the h/d ratio, the outer appearance for the specimens with the h/d ratio of 0.5 at a strain rate of 5 x 10^{-4} s^{-1} is shown in Figure 4.24. The specimen still maintains the circular plate and no violent fracture occurs after compression testing, so it will not observe any angle for the fracture plane inclination. In an enlarged micrograph (as marked by square in Figure 4.24), the plate surface exhibits no obvious change after compression testing, as shown in Figure 4.25. Equally, in an enlarged micrograph (as marked by arrow in Figure 4.24), it could be clearly observed the vein-like characteristics, as shown in Figure 4.26. Figure 4.27 shows that the fracture surface morphology consists mostly of vein-like patterns without any cleavage feature at a higher magnification, indicating that the deformation occurred is due to the propagation of shear band. In addition, Figure 4.28 shows the cross-sectional surface from the whole specimen after compression testing. Figure 4.29 also shows that cross-sectional surface consists of vein-like characteristics.

For the specimens with the h/d ratio of 0.25 at a strain rate of 5 x 10^{-4} s^{-1}, Figure 4.30 shows the outer appearance. It is similar to the specimens with the h/d ratio of 0.5, the specimen still maintains the circular plate and no violent fracture occurs after compression testing due to the specimen is as thin as thin sheet, so it reveals no angle for the fracture plane inclination. In an enlarged micrograph (as marked by square in Figure 4.30), the plate surface exhibits no obvious change after compression testing, as shown in Figure 4.31. Equally, in an enlarged micrograph (as marked by arrow in Figure 4.30), it could be clearly observed the vein-like characteristics without any cleavage feature, as shown in Figure 4.32. In addition, it is found that the vein-like characteristics are denser as compared with Figure 4.27, indicating that the propagation of shear band is more intense and complicated. Furthermore, Figure 4.33 shows the cross-sectional surface from the whole specimen after compression testing. In an enlarged micrograph (as marked by square in Figure 4.33), it could be clearly observed the vein-like characteristics spreading over the cross-sectional surface, as shown in Figure 4.34. Figure 4.35 shows that cross-sectional view of vein-like characteristics at a higher magnification. As compared with Figure 4.29, it is could be found that the vein-like characteristics are denser spreading over the entire fracture surface. There are some structures that seem to be formed by piling up several vein-like structures.

In addition, another characteristic for the compression tests is that flow layers or liquid droplets (as marked by arrows in Figure 4.36) could be seen on the fracture surface. These flow layers occur on the fracture surface and cover some vein-like structures. A localized melted region is observed on the fracture surface, indicating that localized melting occurred during the final fracture along the shear band.

Chapter 5 Discussions

5.1 The effects of the Ag addition on the Mg-Cu-Ag-Gd alloy system

On the basis of the empirical BMG formation criteria, the formation of bulk metallic glasses should satisfy: (1) the multicomponent alloy systems consisting of more than three elements; (2) large differences in atomic size between the constituent elements; (3) negative heat of mixing among the major elements; and (4) alloy compositions close to the deep eutectic point. In accordance with these rules for achieving high GFA, one of the important factors for the formation of the amorphous phase is related to a large difference in atomic size among the main constituents. According to the Table 3.2, the fourth additional element Ag has an atomic size of 0.14447 nm that is larger than that of Cu (0.12780 nm). The atomic size differences of Mg and Gd to Ag are 10.87 % and 24.72 %, respectively. The element Ag has a significant atomic size difference, above 10%, compared to Mg and Gd constituent elements. This is in agreement with the first and second rules for the empirical BMG formation criteria. However, according to the argument for the size effect, the effect of the replacement of Cu by Ag is not proper for the Mg-Cu-Ag-Gd alloy.

On the other hand, regarding the differences in negative heat of mixing between the components, as shown in Table 5.1, another important factor needs to be considered. The value of the heat of mixing is −3 kJ/mol for Cu–Mg, −22 kJ/mol for Cu–Gd, compared to the −10 kJ/mol for Ag–Mg and −29 kJ/mol for Ag–Gd. Hence, the negative heat of mixing of Ag–Mg and Ag–Gd is larger than that of Cu–Mg and Cu–Gd. According to the DSC results, the Ag addition can lead to the lower T_l, resulting in the decrease of ΔT_l and the increase of T_{rg}. This indicates that the alloy is closer to the eutectic point. To sum up the above description, the success of making BMGs is primarily attributed to three main characteristics: a multiple system consisting of at least three elements with a deep eutectic point; significant difference in atomic size ratios and large negative heats of mixing between the three main constituent elements. Therefore, the Ag containing alloy should be exhibited a good GFA for the formation of BMGs.

In addition, the absolute values of heats of mixing for Ag with Mg and Gd are larger than those for Cu with Mg and Gd. Therefore, the more negative heats of mixing for Ag with Mg and Gd allow us to presume that the bonding forces among Mg, Cu, Ag and Gd elements are stronger than those among Mg, Cu and Gd elements. This might result in the increase of the T_g for Ag containing alloys, so that it is more difficult to deform the Ag containing alloy than Ag-free alloy. As shown in Figure 4.11, the $Mg_{65}Cu_{25}Gd_{10}$ BMG has the lower H_v value (232), while the $Mg_{65}Cu_{15}Ag_{10}Gd_{10}$ BMGs are harder (255), suggesting that the $Mg_{65}Cu_{25}Gd_{10}$ BMG could be improved on hardness by Ag addition.

On the basis of density measurement, as shown in Table 4-2, The $Mg_{65}Cu_{25}Gd_{10}$ BMG has the smaller density value 3.75 g/cm^3 and the density value for $Mg_{65}Cu_{15}Ag_{10}Gd_{10}$ is 3.94 g/cm^3. The density increases by the addition of Ag in Mg-Cu-Ag-Gd, indicating that the atomic configuration in the $Mg_{65}Cu_{15}Ag_{10}Gd_{10}$ BMG possesses a more densely packed structure. Hence, the denser structure would enhance the ability of material against deformation, resulting in the increase of hardness. Hence, it would be useful to improve the hardness for the Ag containing alloy.

5.2 The glass forming ability of the Mg-Cu-Ag-Gd BMGs

The glass formation and thermal properties of the $Mg_{65}Cu_{25}Gd_{10}$ and $Mg_{65}Cu_{15}Ag_{10}Gd_{10}$

BMGs were investigated by XRD and DSC experiments, respectively. They show good glass forming ability and thermal stability. At the present time in this study, the maximum diameters for fully amorphous structure are both 6 mm for the $Mg_{65}Cu_{25}Gd_{10}$ alloy and the $Mg_{65}Cu_{15}Ag_{10}Gd_{10}$ alloys.

The interval of supercooled liquid region ΔT_x (43 K) for the $Mg_{65}Cu_{15}Ag_{10}Gd_{10}$ amorphous alloy is lower than the ΔT_x (69 K) for $Mg_{65}Cu_{25}Gd_{10}$, indicating that the $Mg_{65}Cu_{15}Ag_{10}Gd_{10}$ amorphous alloy has a lower thermal stability than $Mg_{65}Cu_{25}Gd_{10}$ amorphous alloy. As comparing the ternary Ag-free alloy with the quaternary Ag containing alloy, the fourth additional element would cause the stronger bonding force between atoms, resulting in the increase of the T_g. However, the interaction between more elements would lead to the increase of the probability for crystallization, indicating that it would decrease the T_x by adding the fourth element. Hence, it is believed that the quaternary alloy by the Ag addition would have the lower thermal stability than the Mg-based ternary alloy.

On the other hand, the partial replacement of Cu by Ag in the $Mg_{65}Cu_{15}Ag_{10}Gd_{10}$ alloy leads to approximately 10 K lower liquidus temperature than $Mg_{65}Cu_{25}Gd_{10}$. Similarly, the $Mg_{65}Cu_{15}Ag_{10}Y_{10}/Er_{10}$ alloy has a lower T_m and T_l than $Mg_{65}Cu_{25}Y_{10}/Er_{10}$ [9,56]. The lower liquidus temperature indicates the higher stability of liquid phase for this alloy. This would be useful to fabricate metallic glasses.

According to Table 5.3, the T_{rg} for $Mg_{65}Cu_{15}Ag_{10}Gd_{10}$ alloy is 0.589, which is higher than that for $Mg_{65}Cu_{25}Gd_{10}$ alloy (0.570). The higher T_{rg} value is considered to be the origin for the larger GFA. On the contrary, the γ value for $Mg_{65}Cu_{15}Ag_{10}Gd_{10}$ alloy is 0.408, which is lower than that for $Mg_{65}Cu_{25}Gd_{10}$ alloy (0.423). On the basis of other references on the effect by Ag addition, the improvement of GFA has been reported while Cu is partially replaced with Ag in the Mg-based alloy [9,56]. Hence, the increase of the GFA by the partial replacement of Cu by Ag could be explained by the larger negative heat of mixing for Ag-Mg and Ag-Gd and the lower the liquid temperature for Ag containing alloy to form metallic glass rapidly.

It could be found that the GFA of the quaternary Ag containing system does not agree with the criterion of the γ parameter. In contrast, the GFA of the quaternary Ag containing system has the higher tendency corresponding to the T_{rg} parameter. Maybe, since the data are limited (only for ternary alloy system) to consider the relationship between D_{max} and GFA, so it is difficult to evaluate the correlation of the parameter with GFA in the quaternary Ag containing alloy system. This suggests that the GFA parameters obtained so far are not ready to justify the GFA in the Mg-based alloy with the addition of Ag.

Furthermore, in order to clarify the inter-atomic effect on the GFA and thermal stability for the BMGs, the electronegativity difference (ΔX) and atomic size parameter (δ) of multicomponent are used to explain the GFA of the Mg-based alloys. Generally, the larger the electronegativity difference and atomic size parameter would be, the wider temperature interval of supercooled liquid region and higher the glass forming ability it becomes.

As described above, according to the result of the electronegativity difference (ΔX) for the Mg-Cu-Ag-Gd alloys, as shown in Table 5.2, the Ag containing alloys would cause the degradation of supercooled liquid region with Ag increasing. According to the result of the atomic size parameter (δ) of the Mg-Cu-Ag-Gd alloys, it is opposite to the result of the electronegativity difference for the Mg-Cu-Ag-Gd alloys. However, it seems that the product of the electronegativity difference (ΔX) and atomic size parameter (δ) shows the partial substitution of Cu by Ag would increase the GFA. Referring Table 5.3, the $Mg_{65}Cu_{15}Ag_{10}Y_{10}$

alloy has a higher T_g and lower T_x, T_m and T_l so that it exhibits good GFA to fabricate the BMGs with larger critical diameter than the $Mg_{65}Cu_{25}Y_{10}$ alloy. Similarly, it could have the same effects to add Ag into the Mg-Cu-Er alloy. It is assumed that the γ values for the Mg-Cu-Ag-Y, Mg-Cu-Ag-Gd and Mg-Cu-Ag-Er alloys are irregular. Though the critical diameters are both 6 mm for the $Mg_{65}Cu_{25}Gd_{10}$ and $Mg_{65}Cu_{15}Ag_{10}Gd_{10}$ alloys, it is considered that the substitution of Cu by Ag on BMG formation of Mg-Cu-Y, Mg-Cu-Gd and Mg-Cu-Er alloys could increase the critical diameter size.

5.3 Thermal mechanical properties of the $Mg_{65}Cu_{25}Gd_{10}$ BMG

5.3.1 TMA analysis

The temperature dependence of the relative displacement of the $Mg_{65}Cu_{25}Gd_{10}$ BMG is obtained by TMA operated in the compression mode at the constant stress and a heating rate 0.17 K/s. By closer comparison as shown in Figure 5.1, for the $Mg_{65}Cu_{25}Gd_{10}$ ribbon, the transition temperature region ΔT ($=T_f - T_s$, where T_f and T_s are the finishing and starting temperatures for such displacement transition) shown in the TMA curve is slightly smaller than the ΔT_x data obtained from the DSC trace at the same heating rate. For example, ΔT is about 50 K based on the TMA curve, and ΔT_x is about 70 K based on the DSC curve. The narrower transition temperature interval is probably due to the stress enhanced crystallization under the TMA loading. Furthermore, for the $Mg_{65}Cu_{25}Gd_{10}$ BMG (not ribbon as in Figure 5.1), the narrower transition temperature interval is observed, too (ΔT is about 50 K).

However, it is found that the transition temperature interval for the $Mg_{65}Cu_{25}Gd_{10}$ BMG is shifted to high temperatures as compared with that for the $Mg_{65}Cu_{25}Gd_{10}$ ribbon. For bulk materials, the message is detected from the whole sample, resulting in that the response of material behavior would be performed to the higher temperature. On the contrary, for ribbons or thin films, the response of the message is quicker than that for bulk materials.

Furthermore, it is assumed that small variations in relative displacement below T_g are due to sample/probe alignment. The DTMA curve is obtained from the derivative of the displacement with respect to time. It could be more clearly seen that the obvious change in displacement occurs in the supercooled region. The relative displacement contracts significantly above the glass-transition temperature, indicating that the easy deformability of the glassy alloy in the supercooled liquid region.

5.3.2 DMA analysis

It is interesting to study how the structural change affects the dynamic mechanical properties of the $Mg_{65}Cu_{25}Gd_{10}$ BMG with the continuous heating. During the dynamic mechanical testing, a stress at the constant frequency is applied to the specimen, the resulting stress developed in the sample is measured, and complex modulus could be determined. The complex modulus is a measure of the materials resistance to deformation. It includes both of the in-phase and out-phase responses of the sample by calculating the storage modulus, E', loss modulus, E'', loss tangent, tanδ (=E''/E'). The elastic modulus, or storage modulus, E', is a measure of the elastic energy stored and the viscous modulus, or loss modulus, E'', is a measure of the energy lost. Loss tangent, tanδ, corresponds to the internal friction. The temperature dependence of the storage modulus, loss modulus, and loss tangent for the $Mg_{65}Cu_{25}Gd_{10}$ BMG is combined in Figure 5.2. In addition, the DSC results are also shown for comparison, as shown in Figure 5.2.

For the $Mg_{65}Cu_{25}Gd_{10}$ BMG, E' keeps constant at the low temperature while E'' and tanδ increase gradually from room temperature to 460 K. Subsequently, E’ decreases rapidly from 460 K to 490 K, indicating that the high temperature relaxation. It could be found that is exhibits the strong softening point at about 490 K. For bulk materials, the message is detected from the whole sample, resulting in that the response of material behavior would be performed to the higher temperature, which is the same with TMA. Therefore, from the DSC curve, it is could be seen that the glass transition and crystallization reaction take place in this temperature interval. The combination for the results of DSC, TMA, and DMA is show in Table 5.4. It could be seen that the temperature interval (~50 K) in the TMA and DMA curves is narrower than that (64 K) in the DSC curve, suggesting that the mechanical response to the ΔL is often slower than the thermal response to the ΔC_p. In addition, the narrower transition temperature interval is probably due to the stress induced crystallization under the applied stress with the constant frequency for the dynamic load. With further increasing temperature, E’ enhances gradually due to the crystallization processes. The corresponding E’’ and tanδ show a broad peak from 460 K to 500 K. the temperature interval is also located at the glass transition and crystallization processes. It implies that the glass transition and crystallization processes contribute to the energy lost in this temperature range.

During heating, the glass solid in amorphous state changes to viscous matter in the supercooled state from the room temperature to glass transition temperature. For the storage modulus, at lower temperatures ($<T_g$), the alloy is in its amorphous state with higher modulus. With increasing the temperature, the alloy undergoes softening, resulting in the decrease of the modulus. It is found that the modulus will tend to decrease significantly while the glass solid changes to viscous liquid for amorphous alloy during heating. Hence, it is inferred that the drop in the modulus is associated with atomic motion as the alloy changes from the glass solid state to the viscous liquid state in the supercooled region. Afterwards, as the temperature increases, the occurrence of crystallization will lead that the viscous liquid changes to the

crystalline solid. This will cause the modulus increase due to the precipitate of dispersion nano-crystals or clusters. Hence, as above description, the E’ decreases at nearly T_g due to the change of viscous liquid and then increases due to the occurrence of crystallization, followed by the E’ gradually tend to constant due to the reaction of crystallization.

The same tendency to structural changes depended on temperature is seen in the corresponding E’’ and tanδ curves. During heating, the glass solid changes to viscous liquid, indicating that this will cause the increase of E’’ value resulted in the increase of viscosity. Afterwards, with increasing the temperature, the precipitations of nanocrystals due to crystallization will reduce the viscosity, and thereby reduce the energy lost. It is found that the loss modulus represents the energy lost during relaxation processes, such as the atomic rearrangements and the movements of atomic groups.

5.4 Compressive mechanical properties of the $Mg_{65}Cu_{25}Gd_{10}$ BMG with various specimen height to diameter ratios

Figure 4.16 shows that the compression testing of the $Mg_{65}Cu_{25}Gd_{10}$ BMG exhibits no evidence of plastic yielding before fracture, as reported for the most Mg-based BMGs. Normally, no BMG with distinct plastic strain is obtained for Mg-based alloy systems. The closer observation of the fracture surfaces for the specimen has been also conducted. For specimen with the h/d ratio of 2, this is the common geometry ratio for BMG; it is found that the fracture surface reveals the brittle fracture. Furthermore, at an enlarged magnification, it could be seen that the fracture surface for specimen with the h/d ratio of 2 consists mostly of the cleavage feature characteristics of brittle fracture without vein structures. This explains why the $Mg_{65}Cu_{25}Gd_{10}$ BMG exhibits elastic deformation, indicating that the brittle nature of Mg-based BMGs.

During room temperature compression tests, Pd-based and Zr-based BMGs normally demonstrate a pure shear fracture process and can deform with certain plasticity. The limited compressive plasticity is caused by localized shear bands and characterized by serrated plastic flow. The compressive fracture morphology commonly exhibits the vein-like structures spreading over the whole surfaces along the propagation of the shear band. And the fracture angle is normally closed to 45^o [57]. But the compression tests of the $Mg_{65}Cu_{25}Gd_{10}$ BMG for the specimen with h/d of 2:1 in this study, it show the different observations for the violent brittle features: (1) no macroscopic compressive plasticity (i.e., the serrated flow) is seen, (2) the fracture angle is greater than 45^o, and (3) the morphologies of cleavage structure appears. It suggests that the mechanism of the brittle Mg-based BMGs is different with that of the tougher Pd-based or Zr-based BMGs. The in-depth fracture mechanisms will be examined in my Ph.D. study.

Furthermore, as the h/d ratio decreases, for the specimen with h/d = 1:1, different observations have been seen: (1) elastic fracture is also seen and the stress is lower than that for the specimen with h/d = 2:1 (2) the fracture angle is less than 45^o, and (3) the morphologies exhibits the mixture of cleavage and vein-like structure. It is considered that since the h/d ratio of 1:1 is lower than that of 2:1, the specimen with h/d = 2:1 allows more the generation of shear bands and the shear band propagation is much easier than that for specimen with h/d = 1:1. In contrast, for the specimen with h/d = 1:1, the shear band propagation appears to be retarded and constrained. Under this condition, the fracture occurs more violent surpassed the specimen with h/d of 2:1. Hence, the specimen can not afford to support to cause the more violent fracture, suggested that the response to stress reduction and it would cause the decrease of the fracture angle. In addition, since the shear band propagation appears to be retarded and constrained, it probably promotes the interaction between shear bands, resulting in the vein-like characteristic on the fracture surface.

With decreasing the h/d ratio, the response for the specimen with the h/d value of 1:2 and 1:4 is more distinct. Since the specimen is too thin so that the specimen is always to be constrained during compression testing. Hence, the specimen still maintains the circular plate and no violent fracture occurs after compression testing, resulting in that no fracture angle is observed. Interestingly, especially for the specimen with h/d = 1:4, it is observed that the vein-like characteristic shows the densest packing spreading over the whole fracture surface. Even, some vein-like structure on the fracture surface suffers through condensing to lead to the structural deformation. On the other hand, in an enlarged micrograph from compressive stress-strain curve for the specimen with h/d of 1:4, Figure 4.37 shows that the serrated flow phenomenon is observed (as marked by circularity in Figure 4.37), indicating the deformation of BMG occurs by the generation and propagation of multiple and inhomogeneous shear bands. As mentioned above, it could distinctly elucidate that the shear band propagation is retarded and constrained under this specimen size. The encounter of the propagation of shear bands results in shear band interaction. Under a large number of shear band interaction, it results in the numerous vein-like structure spreading over the fracture surface. These results suggest that the deformation is no longer a simple mechanism. In this study, the different compression properties and deformation mechanisms for the $Mg_{65}Cu_{25}Gd_{10}$ BMG in specimens of different geometry shapes could be seen.

Furthermore, according to the observation in this study, it is found that the direction of vein-like characteristic spread nearly parallels to the shear force direction, i.e., shear bands align parallel with the fracture plane. In addition, another characteristic for the compression tests is that flow layers or liquid droplets could be seen on the fracture surface. In most of the BMGs, local temperature increase could cause remelting inside the shear band at the final stage of compressive fracture. Therefore, re-solidified droplets or a large area of flow layers are often observed on the fracture surface of the BMG after compressive testing. As shown in Figure 4.36, these flow layers occur on the fracture surface and cover some vein-like structures.

It is believed that different specimen geometries and testing methods will have the constraint effects on shear-banding processes and influence the mechanical properties of BMGs. In some constrained geometries, such as uniaxial compression, multiple shear bands may form, resulting in the behavior that is apparently ‘elastic-perfectly plastic’ [58,59]. The specimen geometry, such as the dimension, imposes geometry constraints on the shear band propagation during compression. In this study, it is found that the mechanical behavior of BMG depends on the specimen geometry.

Conner et al. [60] studied the relationship between the shear band spacing and shear offset spacing with the specimen thickness. In Zr-based BMGs, it is found that with increasing specimen thickness, both the shear band and shear offset spacing increased proportionally with the plate thickness. The increase of the shear band spacing is attributed to the strain relaxation in the neighborhood of the shear band at the surface. Under bending, the shear displacements in the shear band scaled with the shear band length and the plate thickness, causing cracks to be initiated in thicker plates at small bending strains. If the thickness was kept well below 1 mm, the shear offsets in the shear bands might be insufficient to initiate cracks [60].

Schroers et al. [61] performed bend tests on the $Pt_{57.5}Cu_{14.7}Ni_{5.3}P_{22.5}$ BMG in term of bars with different thicknesses, around mandrels of radii of 60, 12.7, 9.5, and 6.35 mm. The 1.8 mm thick sample does not fracture during bending over all four mandrels, showing a maximum strain of 15.7%. But the strain to fracture of the 4 mm specimen is only 3%, as shown in Figure 5.3. As proposed by Conner et al. [60], usually, metallic glasses with an aspect ratio (the height to the diameter ratio of a rounded specimen) less than 1.5:1 could deform in an elastic–perfectly plastic manner in compression tests, resulting from geometrical constraints on shear band propagation, while those with aspect ratios in excess of 1.5:1 show little or no plastic deformation.

On the other hand, Jiang et al. [62] conducted quasistatic compression tests on $Zr_{52.5}Cu_{17.9}Ni_{14.6}Al_{10.0}Ti_{5.0}$ specimens with different h/d ratios. The plasticity reached almost 80% for the specimens with the h/d ratio of 0.5, which is much higher than the 2% plasticity for the specimens with the h/d ratio of 2, as shown in Figures 5.4 and 5.5. They attributed the difference to the specimen-dimensional effect where the platen can hinder the excessive propagation of shear bands, avoiding the premature fracture. The same trend is seen in this study. For $Mg_{65}Cu_{25}Gd_{10}$ BMG specimens with h/d less than 0.5, the deformation strain is significantly enlarged to over 15%. The Mg-based BMGs shows a lower strain which is related to the lower Poisson’s ratio.

Although it is realized that differences in specimen testing geometries change the shear band initiation and propagation processes and the mechanical behavior of metallic glasses, the physical mechanism of the geometry effect in metallic glasses needs to be further elucidated. However, in this study it is found that when the BMGs with a h/d ratio less than 1.5:1, especially for lower h/d ratios, the apparent modulus from the recorded stress-strain curve is not in agreement with the nature of materials. Further studies are needed.

Chapter 6 Conclusions

(1) The $Mg_{65}Cu_{25}Gd_{10}$ and $Mg_{65}Cu_{15}Ag_{10}Gd_{10}$ BMGs with different rod diameters from 3 to 6 mm were successfully fabricated by copper mold casting under an argon atmosphere. No obvious pores are observed from the cross-sectional surfaces of the $Mg_{65}Cu_{25}Gd_{10}$ and $Mg_{65}Cu_{15}Ag_{10}Gd_{10}$ BMGs.

(2) For the thermal properties of the Mg-Cu-Ag-Gd BMGs, the replacement of Cu by Ag will degrade the thermal stability and the γ value for the $Mg_{65}Cu_{15}Gd_{10}Ag_{10}$ BMG. The supercooled liquid region ΔT_x and glass forming criterion γ decreases from 69 K and 0.423 for the $Mg_{65}Cu_{25}Gd_{10}$ BMG to 43 K and 0.408 for the $Mg_{65}Cu_{15}Gd_{10}Ag_{10}$ BMG. On the other hand, Ag addition can enhance T_{rg} from 0.570 for $Mg_{65}Cu_{25}Gd_{10}$ to 0.589 for $Mg_{65}Cu_{15}Gd_{10}Ag_{10}$.

(3) The addition of Ag can increase the density from 3.75 g/cm^3 for $Mg_{65}Cu_{25}Gd_{10}$ to 3.94 g/cm^3 for $Mg_{65}Cu_{15}Gd_{10}Ag_{10}$ due to the denser atomic arrangement.

(4) The addition of Ag can increase the hardness from 232 H_v for the $Mg_{65}Cu_{25}Gd_{10}$ BMG to 255 H_v for the $Mg_{65}Cu_{15}Gd_{10}Ag_{10}$ BMG.

(5) The variation of relative displacement ΔL for the $Mg_{65}Cu_{25}Gd_{10}$ BMG in TMA reveals obvious change in the supercooled liquid region. According to the coefficient of thermal expansion (CTE) of the $Mg_{65}Cu_{25}Gd_{10}$ BMG, the CTE for amorphous solid is $\alpha_g = 2.09 \times 10^{-6}$ m/m^oC and for crystal solid is $\alpha_c = 5.73 \times 10^{-6}$ m/m^oC. Especially, in the supercooled liquid region, the CTE for viscous flow is $\alpha_v = -201.35 \times 10^{-6}$ m/m^oC.

(6) Based on the DMA analysis for the $Mg_{65}Cu_{25}Gd_{10}$ BMG, the E', E'', and tan δ change with increasing temperature. During heating, the glass solid changes to viscous liquid and then change to crystal solid, the structural changes as a function of temperature affect the thermal mechanical properties.

(7) In compression tests of the $Mg_{65}Cu_{25}Gd_{10}$ BMG, for the specimen with h/d of 2:1, the fracture strength and elongation are ~806 MPa and 1.97 %, respectively. The $Mg_{65}Cu_{25}Gd_{10}$ BMG shows no evidence of macroscopic yielding and plasticity, as reported for the most of the Mg-based BMGs.

(8) With decreasing h/d ratios from 2:1, 1:1, 1:2 to 1:4, the mechanical properties are seen to vary systematically for $Mg_{65}Cu_{25}Gd_{10}$ BMG. For specimens with h/d value of 2:1 or 1:1, the compression response is similar to most reports. In contrast, for specimens with lower h/d ratios, especially at h/d of 1:4, the fracture strength and elongation are ~911 MPa and 17 %, respectively. The shear band propagation appears to be constrained to cause different mechanical behavior.

(9) In this study, the compressive strength and density of the $Mg_{65}Cu_{25}Gd_{10}$ BMG are 806 MPa and 3.75 g/cm^3, respectively. Therefore, the specific strength of the $Mg_{65}Cu_{25}Gd_{10}$ BMG is 215 $MPa\cdot cm^3/g$. It is promising for future development of a lightweight structural material with high specific strength.

References

[1] 吳學陞, 工業材料, 149 (1999), pp. 154-165.

[2] N.H. Pryds, Mater. Sci. Eng. A, 375-377 (2004), pp. 186-193.

[3] A. Inoue, Mater. Sci. Eng. A, 304-306 (2001), pp. 1-10.

[4] G. Yuan and A. Inoue, J. Alloys Compd., 387 (2005), pp. 134-138.

[5] A. Inoue, A. Kato, T. Zhang, S.G. Kim and T. Masumoto, Mater. Trans. JIM, 32 (1991), pp. 609-616.

[6] A. Inoue, T. Nakamura, N. Nishiyama and T. Masumoto, Mater. Trans. JIM, 33 (1992), pp. 937-945.

[7] G. Shao, B. Lu, Y.Q. Liu and P. Tsakiropoulos, Intermetallics, 13 (2005), pp. 409-414.

[8] C.T. Liu and Z.P. Lu, Intermetallics, 13 (2005), pp. 415-418.

[9] E.S. Park, H.G. Kang, W.T. Kim and D.H. Kim, J. Non-Cryst. Solids, 279 (2001), pp. 154-160.

[10] K. Amiya and A. Inoue, Mater. Trans. JIM, 41 (2000), pp. 1460-1462.

[11] H. Men, Z.Q. Hu and J. Xu, Scripta Mater., 46 (2002), pp. 699-703.

[12] G. Yuan, T. Zhang and A. Inoue, Mater. Lett., 58 (2004), pp. 3012-3016.

[13] X.K. Xi, D.Q. Zhao, M.X. Pan and W.H. Wang, Intermetallics, 13 (2005), pp. 638-641.

[14] X.K. Xi, R.J. Wang, D.Q. Zhao, M.X. Pan and W.H. Wang, J. Non-Cryst. Solids, 344 (2004), pp. 105-109.

[15] H. Men, W.T. Kim and D.H. Kim, J. Non-Cryst. Solids, 337 (2004), pp. 29-35.

[16] G. Yuan, K. Amiya and A. Inoue, J. Non-Cryst. Solids, 351 (2005), pp. 729-735.

[17] W. Klement, R. H. Williams and P. Duwez, Nature, 187 (1960), pp. 869-870.

[18] H.S. Chen and D. Turnbull, Acta Metall., 17 (1969), pp. 1021-1031.

[19] H.S. Chen. Acta Metall., 22 (1974), pp. 1505-1511.

[20] H.W. Kui, A.L. Greer and D. Turnbull, Appl. Phys. Lett., 45 (1984), pp. 615-616.

[21] A. Inoue, T. Zhang and T. Masumoto, Mater. Trans. JIM, 30 (1989), pp. 965-972.

[22] A. Inoue, A. Kato, T . Zhang, S.G. Kim and T. Masumoto, Mate. Trans. JIM, 32 (1991), pp. 609-616.

[23] T. Zhang, A. Inoue and T. Masumoto, Mater. Trans. JIM, 32 (1991), pp. 1005-1010.

[24] A. Inoue, N. Nishiyama, and H. Kimura, Mater. Trans. JIM, 38 (1997), pp.179-183.

[25] C. Fan, A. Takeuchi and A. Inoue, Mater. Trans. JIM, 40 (1999), pp. 42-51.

[26] H.S. Chen and C.E. Miller, Rev. Sci. Instrum, 41 (1970), pp. 1237-1238.

[27] H.H. Liebermann and C.D. Graham, IEEE Trans. Magn., MAG-12 (1976), pp. 921-926.

[28] A. Inoue, Acta Mater., 48 (2000), pp. 279-306.

[29] D. Turbbull and J.C. Fisher, J. Chem, Physics, 17 (1949), pp. 71-73.

[30] Z.P. Lu, H. Tan, Y. Li and S.C. Ng, Scripta Mater., 42 (2000), pp. 667-673.

[31] T.A. Waniuk, J. Schroers and W.L. Johnson, Appl. Phys. Lett., 78 (2001), pp. 1213-1215.

[32] A. Inoue, W. Zhang, T. Zhang and K. Kurosaka, Acta Mater., 29 (2001), pp. 2645-2652.

[33] T.D. Shen and R.B. Schwarz, J. Mater. Res., 14 (1999), pp. 2107-2115.

[34] B. S Murty and K. Hono, Mater. Trans. JIM, 41 (2000), pp. 1538-1544.

[35] Z.P. Lu and C.T. Liu, Acta Mater., 50 (2002), pp. 3501-3512.

[36] T. Egami, Mater. Sci. Eng. A, 226 (1997), pp. 261-267.

[37] C.H. Shek, Y.M. Wang and C. Dong, Mater. Sci. Eng. A, 291 (2000), pp. 78-85.

[38] S. Fang, X. Xiao, L. Xia, W. Li and Y. Dong, J. Non-Cryst. Solids, 321 (2003), pp.120-125.

[39] W. Chen, Y. Wang, J. Qiang and C. Dong, Acta Mater., 51 (2003), pp. 1899-1907.

[40] T. Zhang and A. Inoue, Mater. Trans. JIM, 39 (1998), pp. 857-862.

[41] A. Inoue, Bulk Amorphous Alloys. Trans. Tech. Publications, Zurich, 1998.

[42] Y. Yokoyama, N. Nishiyama, K. Fukaura, H. Sunada and A. Inoue, Mater. Trans. JIM, 40 (1999), pp. 696-699.

[43] Y. Yoshizawa, S. Oguma and K. Yamauchi, J. Appl. Phys., 64 (1988), pp. 6044-6046.

[44] T.D. Shen and R.B. Schwarz, Acta Mater., 49 (2001), pp. 837-847.

[45] K. Asami and A. Inoue, Mater. Sci. Eng. A, 375–377 (2004), pp. 235-239.

[46] T. Shoji and A. Inoue, J. Alloys Compd., 292 (1999), pp. 275-280.

[47] K. Isogai, T. Shoji, H.M. Kimura and A. Inoue, Mater. Trans. JIM, 41 (2000), pp. 1486-1486.

[48] A. Inoue, Bulk Amorphous Alloys, Trans. Tech. Publications, Zurich, 1998-1999.

[49] Z.P. Lu, G. Wang, J. Shen, J.F. Sun, Z.H. Stachurski and B.D. Zhou, Mater. Sci. Eng. A, 398 (2005), pp. 82-87.

[50] 鄭振東，非晶質金屬漫談，建宏出版社，Taipei，Taiwan，1990.

[51] X.S. Xiao, S.S. Fang, L. Xia, W.H. Li, Q. Hua, Y.D. Dong, J. Non-Cryst. Solids, 330 (2003), pp. 242-247.

[52] M. Kusy, U. Kuhn, A. Concustell, A. Gebert, J. Das, J. Eckert, L. Schultz, M.D. Baro, Intermatillcs, (2006), pp.1-5, in press.

[53] C. Fan, L.J. Kecskes, D.C. Qiao, H. Choo, P.K. Liaw, J. Non-Cryst. Solids, 352 (2006), pp. 174-179.

[54] C.A. Schuh, A.C. Lund, T.G. Nieh, Acta Mater., 52 (2004), pp. 5879-5891.

[55] Y.T. Cheng, MS Thesis, NSYSU, Taiwan, 2005.

[56] W.Y. Liu, H.F. Zhang, Z.Q. Hu, H. Wang, J. Alloys Compd., 397 (2005), pp. 202-206.

[57] Z.F. Zhang, J. Eckert, J. Schultz, Acta Mater., 51 (2003), pp. 1167-1179.

[58] T.C. Hufnagel, P. Deiry, R.P. Vinci, Scripta Mater, 43 (2000), pp. 1071-1075.

[59] T.C. Hufnagel, C. Fan, , J. Lia, S. Brennan, Intermetallics, 10 (2002), pp. 1163-1166.

[60] R.D. Conner, Y. Li, W.D. Nix, W.L. Jonson, Acta Mater, 52 (2004), pp. 2429-2434.

[61] J. Schroers, W.L. Johnson, Phys. Rev. Lett., 93 (2004), 255506.

[62] W.H. Jiang, G.J. Fan, H. Choo, P.K. Liaw. Materials letters, (2006), in press.

Table 1.1 Fundamental properties and application fields of bulk amorphous and nanocrystalline alloys [3].

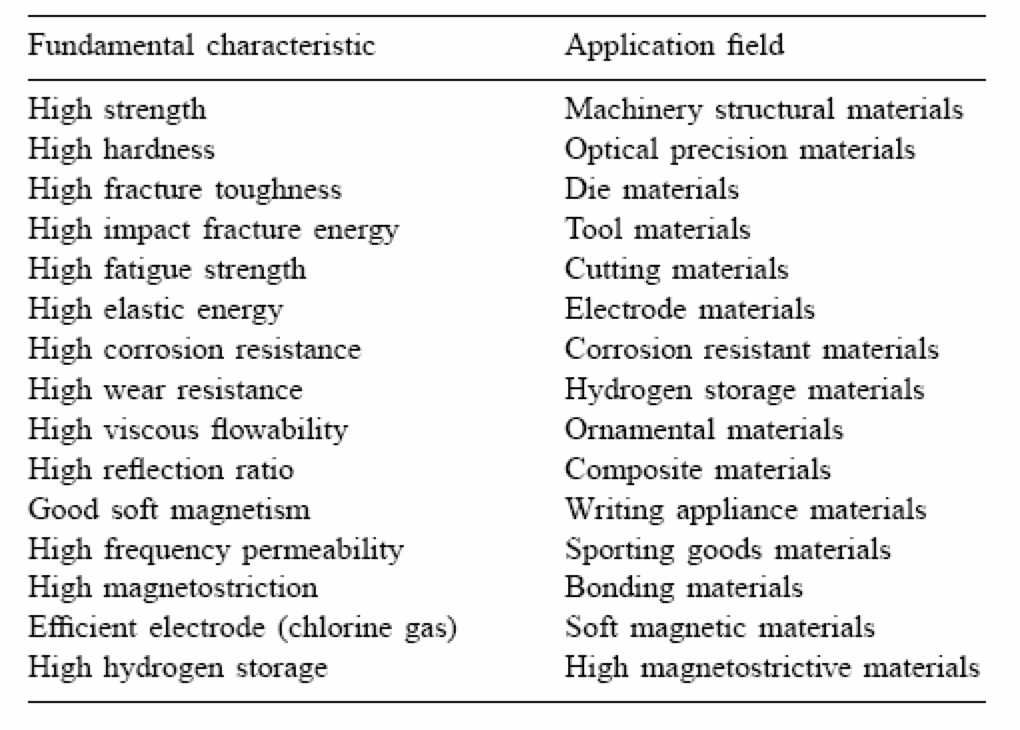

Fundamental characteristic	Application field
High strength	Machinery structural materials
High hardness	Optical precision materials
High fracture toughness	Die materials
High impact fracture energy	Tool materials
High fatigue strength	Cutting materials
High elastic energy	Electrode materials
High corrosion resistance	Corrosion resistant materials
High wear resistance	Hydrogen storage materials
High viscous flowability	Ornamental materials
High reflection ratio	Composite materials
Good soft magnetism	Writing appliance materials
High frequency permeability	Sporting goods materials
High magnetostriction	Bonding materials
Efficient electrode (chlorine gas)	Soft magnetic materials
High hydrogen storage	High magnetostrictive materials

Table 2.1 The classification of amorphous alloy systems [28].

1. Nonferrous metal base	Years
Mg-Ln-M (Ln = Lanthanide metal, M = Ni, Cu or Zn)	1988
Ln-Al-TM; Ln-Ga-TM (TM = VI~ VIII group transition metal)	1989
Zr-Al-TM; Zr-Ti-AL-TM	1990
Ti-Zr-TM; Zr-Ti-TM-Be	1993
Zr-(Nb,Pd)-Al-TM	1995
Pd-Cu-Ni-P; Pd-Ni-Fe-P	1996
Pd-Cu-B-Si	1997
Ti-Ni-Cu-Sn	1998
2. Ferrous group metal base	
Fe-(AL,Ga)-(P,C,B,Si,Ge); Fe-(Nb,Mo)-(Al,Ga)-(P,B,Si)	1995
Co-(Al,Ga)-(P,B,Si); Fe-(Zr,Hf,Nb)-B; Co-Fe-(Zr,Hf,Nb)-B; Ni-(Zr,Hf,Nb)-(Cr,Mo)-B	1996
Fe-Co-Ln-B	1998
Fe-(Nb,Cr,Mo)-(P,C,B); Ni-(Nb,Cr,Mo)-(P,C)	1999

Table 2.2 The classification of amorphous alloy systems [28].

I	ETM(or Ln) + Al + LTM	Zr-Al-Ni、Zr-Al-Cu、Zr-Al-Ni-Cu、Zr-Ti-Al-Ni-Cu、Zr-Nb-Al-Ni-Ln、Zr-Ga-Ni
		Ln-Al-Ni、Ln-Al-Cu、Ln-Al-Ni-Cu、Ln-Ga-Ni、Ln-Ga-Cu
II	LTM + ETM + Metalloid	Fe-Zr-B、Fe-Hf-b、Fe-Zr-Hf-B、Fe-Co-Ln-B、Co-Zr-Nb-B
III	LTM(Fe) + Al or Ga + Metalloid	Fe-(Al, Ga)-Metalloid
IV	Mg + Ln +LTM	Mg-Ln-Ni、Mg-Ln-Cu
	TM(Zr or Ti) + Be + LTM	Zr-Ti-Be-Ni-Cu
V	LTM + Metalloid	Pd-Ni-P、Pd-Cu-Ni-P、Pt-Ni-p

ETM = IVB~VIB Group Transition Metal.

LTM = VIIB~VIIIB Group Transition Metal.

Table 2.3 Mechanisms for the stabilization of supercooled liquid and the high glass-forming ability for the multicomponent alloys which satisfy the three empirical rules [28].

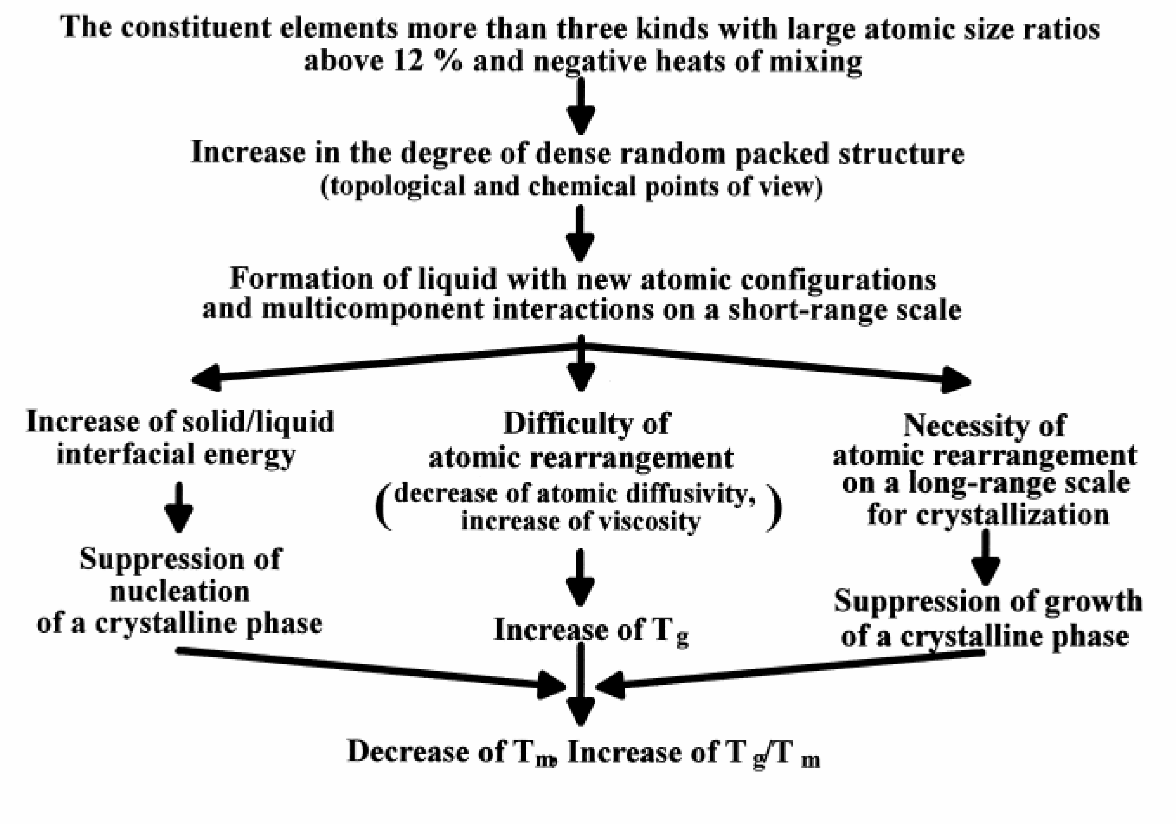

Table 2.4 Summary of Δ T_x, T_{rg}, γ, critical cooling rate R_c and critical section thickness *Zc* for typical BMGs [35].

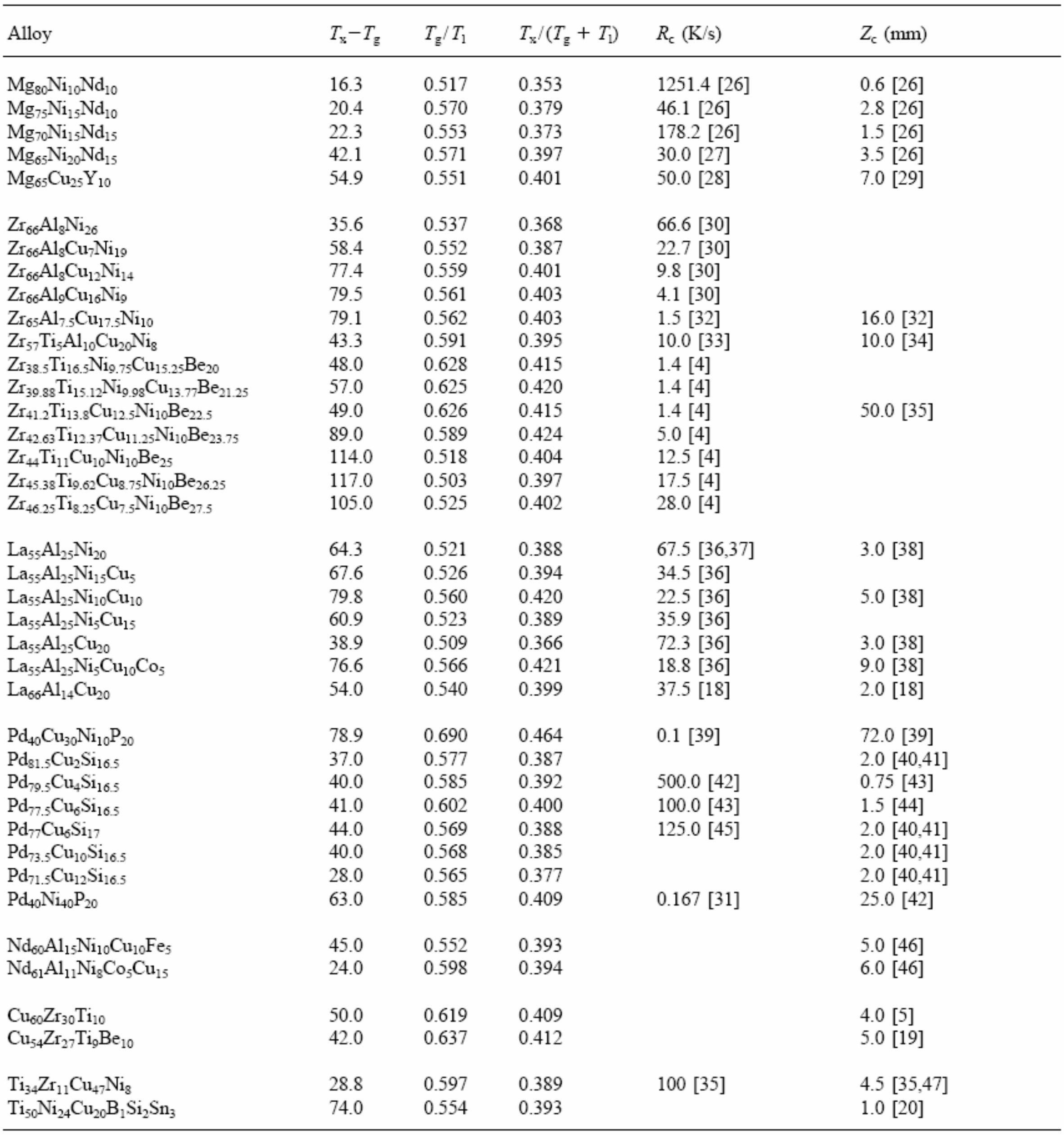

Alloy	$T_x - T_g$	T_g/T_l	$T_x/(T_g + T_l)$	R_c (K/s)	Z_c (mm)
$Mg_{80}Ni_{10}Nd_{10}$	16.3	0.517	0.353	1251.4 [26]	0.6 [26]
$Mg_{75}Ni_{15}Nd_{10}$	20.4	0.570	0.379	46.1 [26]	2.8 [26]
$Mg_{70}Ni_{15}Nd_{15}$	22.3	0.553	0.373	178.2 [26]	1.5 [26]
$Mg_{65}Ni_{20}Nd_{15}$	42.1	0.571	0.397	30.0 [27]	3.5 [26]
$Mg_{65}Cu_{25}Y_{10}$	54.9	0.551	0.401	50.0 [28]	7.0 [29]
$Zr_{66}Al_8Ni_{26}$	35.6	0.537	0.368	66.6 [30]	
$Zr_{66}Al_8Cu_7Ni_{19}$	58.4	0.552	0.387	22.7 [30]	
$Zr_{66}Al_8Cu_{12}Ni_{14}$	77.4	0.559	0.401	9.8 [30]	
$Zr_{66}Al_9Cu_{16}Ni_9$	79.5	0.561	0.403	4.1 [30]	
$Zr_{65}Al_{7.5}Cu_{17.5}Ni_{10}$	79.1	0.562	0.403	1.5 [32]	16.0 [32]
$Zr_{57}Ti_5Al_{10}Cu_{20}Ni_8$	43.3	0.591	0.395	10.0 [33]	10.0 [34]
$Zr_{38.5}Ti_{16.5}Ni_{9.75}Cu_{15.25}Be_{20}$	48.0	0.628	0.415	1.4 [4]	
$Zr_{39.88}Ti_{15.12}Ni_{9.98}Cu_{13.77}Be_{21.25}$	57.0	0.625	0.420	1.4 [4]	
$Zr_{41.2}Ti_{13.8}Cu_{12.5}Ni_{10}Be_{22.5}$	49.0	0.626	0.415	1.4 [4]	50.0 [35]
$Zr_{42.63}Ti_{12.37}Cu_{11.25}Ni_{10}Be_{23.75}$	89.0	0.589	0.424	5.0 [4]	
$Zr_{44}Ti_{11}Cu_{10}Ni_{10}Be_{25}$	114.0	0.518	0.404	12.5 [4]	
$Zr_{45.38}Ti_{9.62}Cu_{8.75}Ni_{10}Be_{26.25}$	117.0	0.503	0.397	17.5 [4]	
$Zr_{46.25}Ti_{8.25}Cu_{7.5}Ni_{10}Be_{27.5}$	105.0	0.525	0.402	28.0 [4]	
$La_{55}Al_{25}Ni_{20}$	64.3	0.521	0.388	67.5 [36,37]	3.0 [38]
$La_{55}Al_{25}Ni_{15}Cu_5$	67.6	0.526	0.394	34.5 [36]	
$La_{55}Al_{25}Ni_{10}Cu_{10}$	79.8	0.560	0.420	22.5 [36]	5.0 [38]
$La_{55}Al_{25}Ni_5Cu_{15}$	60.9	0.523	0.389	35.9 [36]	
$La_{55}Al_{25}Cu_{20}$	38.9	0.509	0.366	72.3 [36]	3.0 [38]
$La_{55}Al_{25}Ni_5Cu_{10}Co_5$	76.6	0.566	0.421	18.8 [36]	9.0 [38]
$La_{66}Al_{14}Cu_{20}$	54.0	0.540	0.399	37.5 [18]	2.0 [18]
$Pd_{40}Cu_{30}Ni_{10}P_{20}$	78.9	0.690	0.464	0.1 [39]	72.0 [39]
$Pd_{81.5}Cu_2Si_{16.5}$	37.0	0.577	0.387		2.0 [40,41]
$Pd_{79.5}Cu_4Si_{16.5}$	40.0	0.585	0.392	500.0 [42]	0.75 [43]
$Pd_{77.5}Cu_6Si_{16.5}$	41.0	0.602	0.400	100.0 [43]	1.5 [44]
$Pd_{77}Cu_6Si_{17}$	44.0	0.569	0.388	125.0 [45]	2.0 [40,41]
$Pd_{73.5}Cu_{10}Si_{16.5}$	40.0	0.568	0.385		2.0 [40,41]
$Pd_{71.5}Cu_{12}Si_{16.5}$	28.0	0.565	0.377		2.0 [40,41]
$Pd_{40}Ni_{40}P_{20}$	63.0	0.585	0.409	0.167 [31]	25.0 [42]
$Nd_{60}Al_{15}Ni_{10}Cu_{10}Fe_5$	45.0	0.552	0.393		5.0 [46]
$Nd_{61}Al_{11}Ni_8Co_5Cu_{15}$	24.0	0.598	0.394		6.0 [46]
$Cu_{60}Zr_{30}Ti_{10}$	50.0	0.619	0.409		4.0 [5]
$Cu_{54}Zr_{27}Ti_9Be_{10}$	42.0	0.637	0.412		5.0 [19]
$Ti_{34}Zr_{11}Cu_{47}Ni_8$	28.8	0.597	0.389	100 [35]	4.5 [35,47]
$Ti_{50}Ni_{24}Cu_{20}B_1Si_2Sn_3$	74.0	0.554	0.393		1.0 [20]

Table 3.1 The constituent contents of the elements in this study.

$Mg_{65}Cu_{25-X}Ag_XGd_{10}$	Mg		Cu		Gd		Ag	
	At%	Wt%	At%	Wt%	Wt%	At%	Wt%	At%
$Mg_{65}Cu_{25}Gd_{10}$	65	33.323	25	33.509	10	33.168	0	0
$Mg_{65}Cu_{22.5}$ $g_{2.5}Gd_{10}$	65	32.562	22.5	29.469	10	32.411	2.5	5.558
$Mg_{65}Cu_{20}Ag_5Gd_{10}$	65	31.835	20	25.610	10	31.687	5	10.868
$Mg_{65}Cu_{17.5}Ag_{7.5}Gd_{10}$	65	31.140	17.5	21.920	10	30.995	7.5	15.945
$Mg_{65}Cu_{15}Ag_{10}Gd_{10}$	65	30.474	15	18.387	10	30.333	10	20.806

Table 3.2 Fundamental data related to the elements in this study.

Symbol	Atomic weight	Structure	Electron-negativity	Atomic size (nm)	Melting point (^{o}C)	Density (g/cm^3)
Mg	24.305	HCP	1.31	0.16013	650.00	1.74
Cu	63.546	FCC	2.00	0.12780	1084.62	8.96
Ag	107.860	FCC	1.93	0.14447	961.78	10.05
Gd	157.250	HCP	1.20	0.18013	1311.20	7.89

The atomic size differences of Mg and Gd to Cu are 25.27 % and 40.92 %.

The atomic size differences of Mg and Gd to Ag are 10.87 % and 24.72 %.

Table 4.1 Summary of thermal properties for Mg-Cu-Gd-Ag alloys.

Alloys	Heating rate (K/s)	T_g (K)	T_x (K)	ΔT_x (K)	T_m (K)	T_l (K)	ΔT_l (K)	T_{rg}	γ
$Mg_{65}Cu_{25}Gd_{10}$	0.33	414	482	68	681	727	46	0.569	0.422
$Mg_{65}Cu_{15}Ag_{10}Gd_{10}$		417	461	44	686	720	34	0.579	0.405
$Mg_{65}Cu_{25}Gd_{10}$	0.67	421	490	69	684	738	54	0.570	0.423
$Mg_{65}Cu_{15}Ag_{10}Gd_{10}$		429	472	43	688	728	40	0.589	0.408

$\Delta T_x = T_x - T_g$

$\Delta T_l = T_l - T_m$

$T_{rg} = T_g / T_l$

$\gamma = T_g / (T_x + T_l)$

Table 4-2 Summary of the density for various Mg-based BMGs

BMG	Theoretical density d_t (g/cm^3)	Experimental density d_e (g/cm^3)	d_{exp}/d_{theo}
$Mg_{65}Cu_{25}Gd_{10}$	4.16	3.75	0.901
$Mg_{65}Cu_{15}Ag_{10}Gd_{10}$	4.31	3.94	0.914

Pure elements:

Mg: 1.74 g/cm^3; Cu: 8.96 g/cm^3; Ag: 10.50 g/cm^3; Gd: 7.89 g/cm^3.

Table 4.3 Summary of compressive mechanical properties for $Mg_{65}Cu_{25}Gd_{10}$ BMGs.

BMG type	h/d ratio (mm/mm)	Strain rate (s^{-1})	elastic Modulus (GPa)	Strength (MPa)	Elongation (%)	Fracture angle (°)
$Mg_{65}Cu_{25}Gd_{10}$	8/4	5×10^{-4}	45	806	1.97	54
$Mg_{65}Cu_{25}Gd_{10}$	4/4	5×10^{-4}	21	679	4.15	46
$Mg_{65}Cu_{25}Gd_{10}$	2/4	5×10^{-4}	9	848	11.53	----
$Mg_{65}Cu_{25}Gd_{10}$	1/4	5×10^{-4}	6	911	16.99	----

Table 4.4 Summary for the $Mg_{65}Cu_{25}Gd_{10}$ and $Mg_{65}Cu_{15}Ag_{10}Gd_{10}$ BMGs in this study.

composition	$Mg_{65}Cu_{25}Gd_{10}$	$Mg_{65}Cu_{15}Ag_{10}Gd_{10}$
T_g (K)	421	429
T_x (K)	490	472
ΔT_x (K)	69	43
T_m (K)	684	688
T_l (K)	738	728
ΔT_l (K)	54	40
T_{rg}	0.570	0.589
γ	0.423	0.408
D_{max} (mm)	6	6
Density (g/cm^3)	3.75	3.94
H_v	232	255
Strength (MPa)	806	---
Elongation (%)	1.97	---
Elastic modulus (GPa)	45	---
Specific strength ($MPa \cdot cm^3/g$)	215	---

Table 5.1 The negative heat of mixing of the Mg, Cu, Gd, and Ag elements.

	Mg	Cu	Gd	Ag
Mg		-3	-6	-10
Cu	-3		-22	2
Gd	-6	-22		-29
Ag	-10	2	-29	

Table 5.2 The electronegativity difference (ΔX) and atomic size parameter (δ) of the Mg-Cu-Ag-Gd alloys.

Compositions	ΔX	δ	ΔX ・δ
$Mg_{65}Cu_{25}Gd_{10}$	0.307	0.069	0.021
$Mg_{65}Cu_{20}Ag_5Gd_{10}$	0.301	0.074	0.022
$Mg_{65}Cu_{15}Ag_{10}Gd_{10}$	0.295	0.079	0.023

Table 5.3 The thermal properties obtained by DSC for the Ag containing alloys at the heating rate of 0.67 K/s.

Alloys	T_g (K)	T_x (K)	ΔT_x (K)	T_m (K)	T_l (K)	ΔT_l (K)	T_{rg}	γ	D_{max}	Ref.
$Mg_{65}Cu_{25}Y_{10}$	426	494	68	728	750	22	0.568	0.420	4	[9]
$Mg_{65}Cu_{15}Ag_{10}Y_{10}$	428	475	47	688	707	19	0.605	0.418	6	[9]
$Mg_{65}Cu_{25}Er_{10}$	422	480	58	741	766	25	0.550	0.404	3	[56]
$Mg_{65}Cu_{15}Ag_{10}Er_{10}$	427	465	38	706	733	27	0.582	0.401	6	[56]
$Mg_{65}Cu_{25}Gd_{10}$	421	490	69	684	738	54	0.570	0.423	6	This study
$Mg_{65}Cu_{15}Ag_{10}Gd_{10}$	429	472	43	688	728	40	0.589	0.408	6	

Table 5.4 The combination of DSC, TMA, DMA for the $Mg_{65}Cu_{25}Gd_{10}$ BMG with a heating rate of 0.17 K/s.

Instrument	T_g (K)	T_x (K)	ΔT_x (K)
DSC	404	468	64
TMA	428	474	46
DMA	456	505	49

(1) The T_g points for TMA and DMA are taken from the onset point of the DTMA and tanδ curves, respectively.

(2) The T_x points for TMA and DMA are taken from the offset point of the DTMA and tanδ curves, respectively.

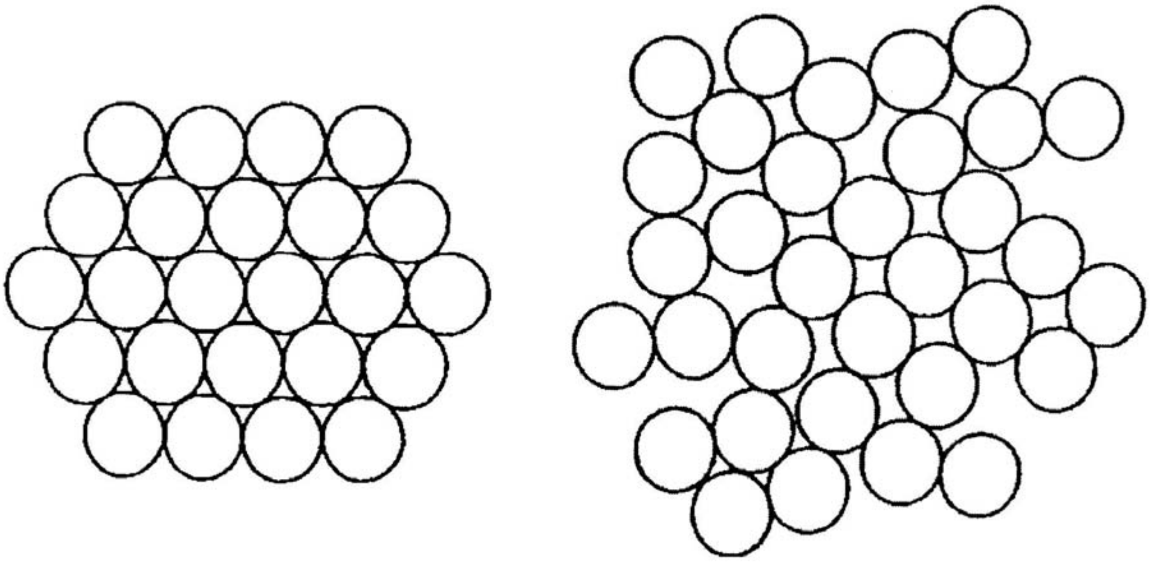

Figure 1.1 The atomic arrangements of crystal and amorphous alloy [1].

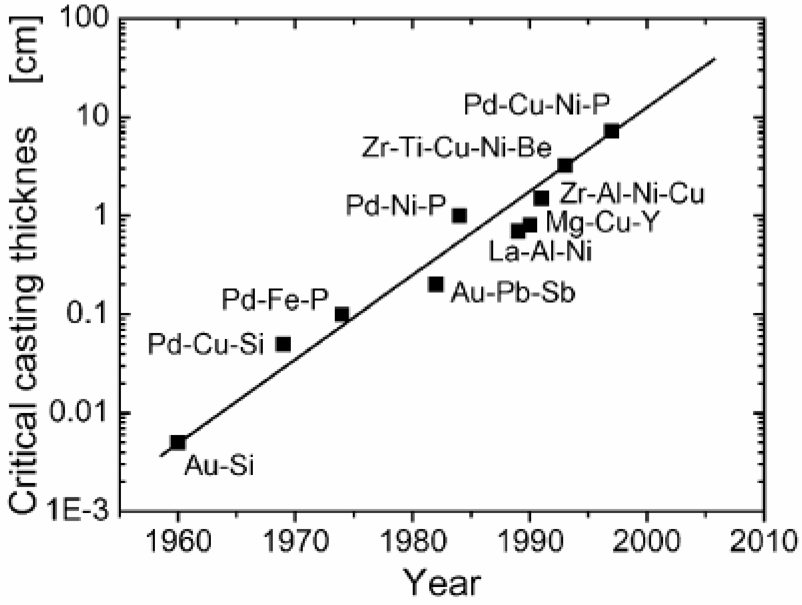

Figure 2.1 Critical casting thicknesses for glass formation as a function of the year the corresponding alloy has been discovered.

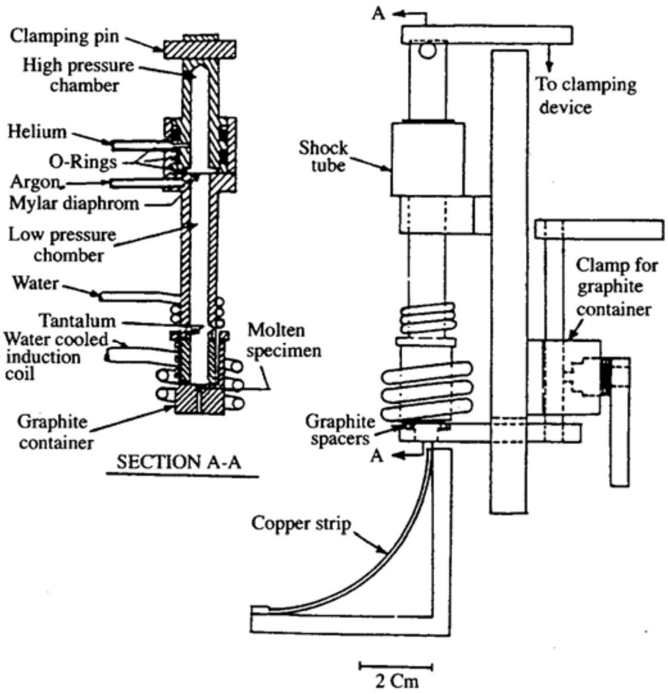

Figure 2.2 A schematic diagram of the splat quenching method [1].

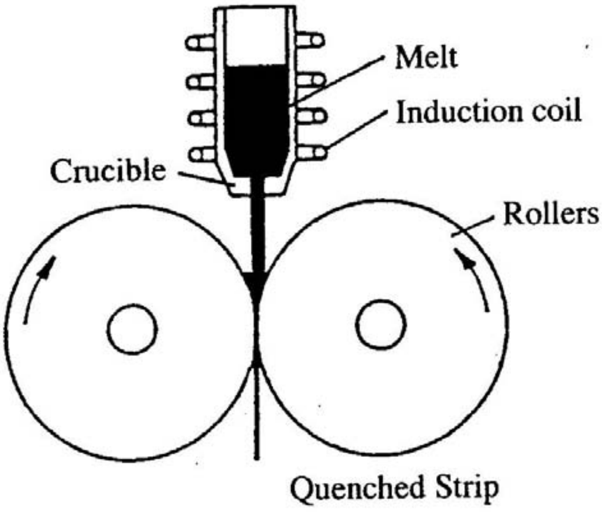

Figure 2.3 A schematic diagram of the two roller quenching method [1].

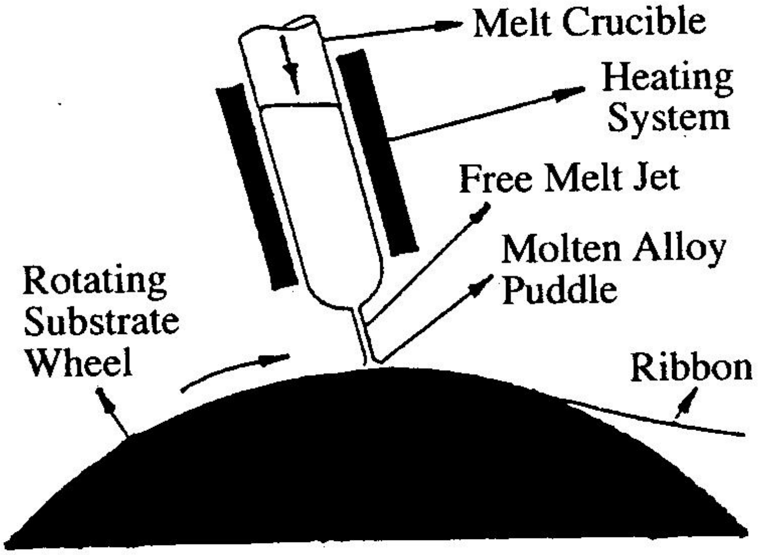

Figure 2.4 A schematic diagram of the chill block melt spinning [1].

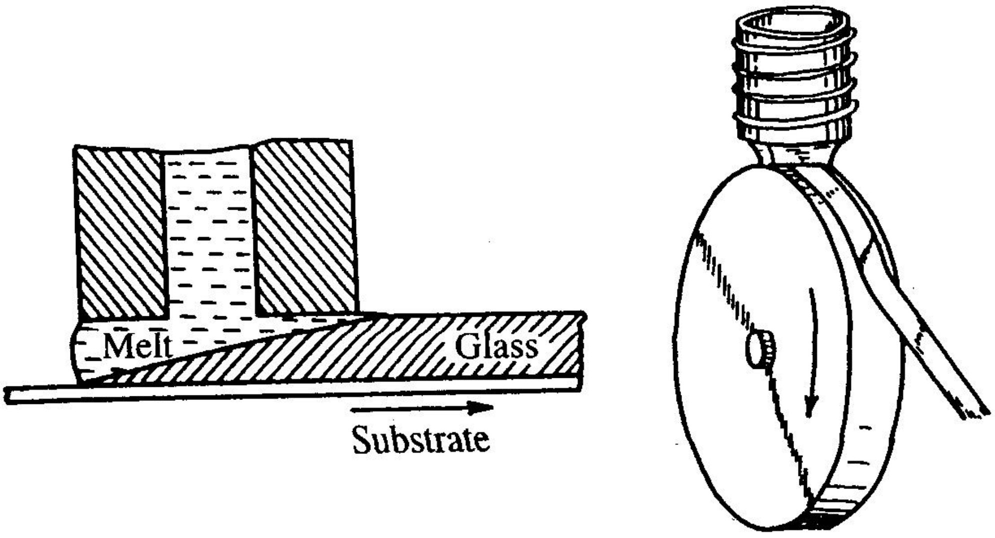

Figure 2.5 A schematic diagram of the planar flow casting process [1].

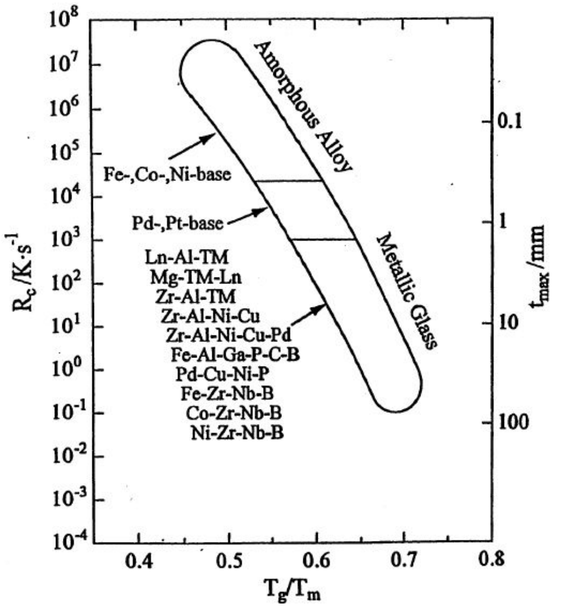

Figure 2.6 Relationship between the critical cooling rate (R_c), the maximum sample thickness (t_{max}) and reduced glass transition temperature (T_g/T_m) for bulk amorphous systems [28].

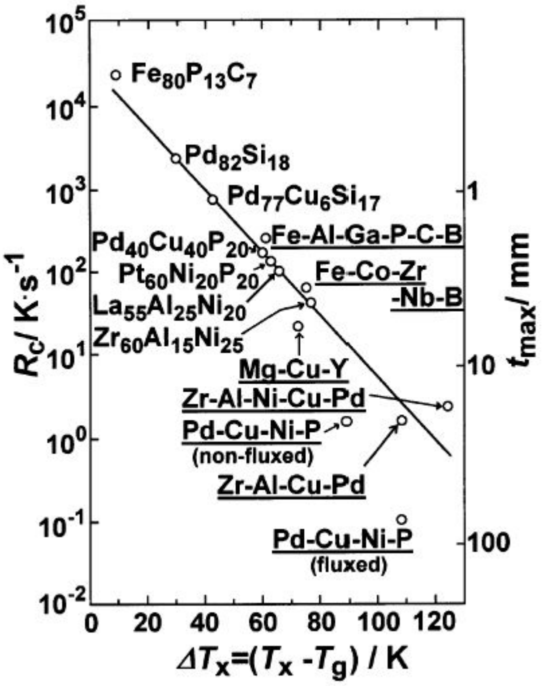

Figure 2.7 Relationship between the critical cooling rate (R_c) and the maximum sample thickness (t_{max}) for bulk amorphous alloy systems [28].

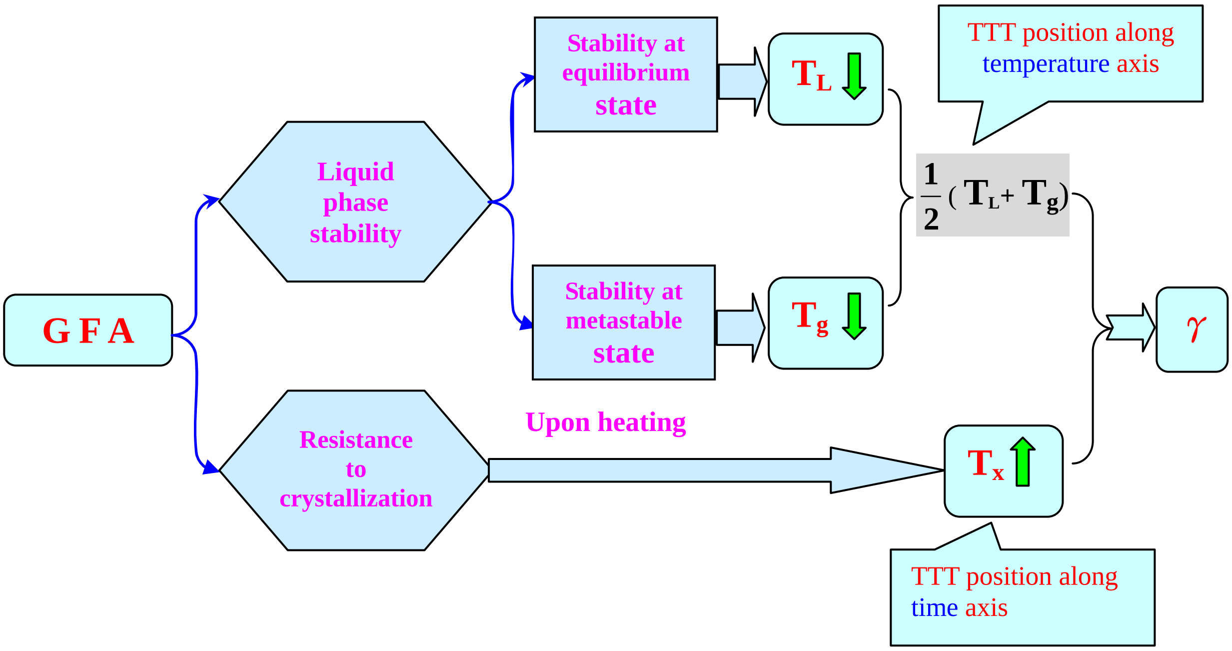

Figure 2.8 The parameter of γ for glass forming ability (GFA) [35].

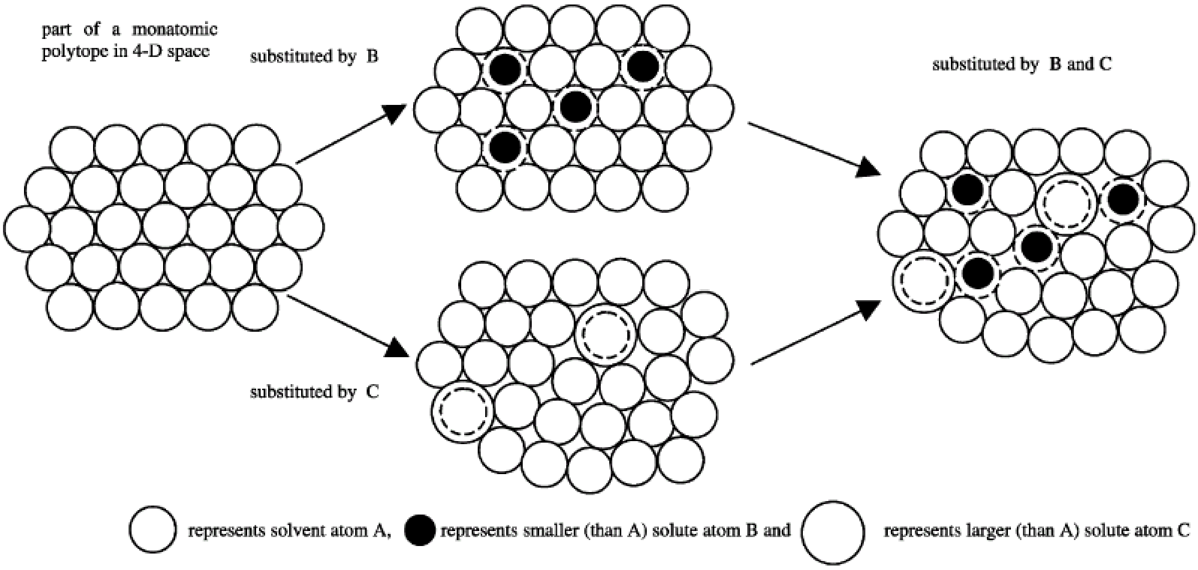

Figure 2.9 The atomic configuration of the different atomic size system .

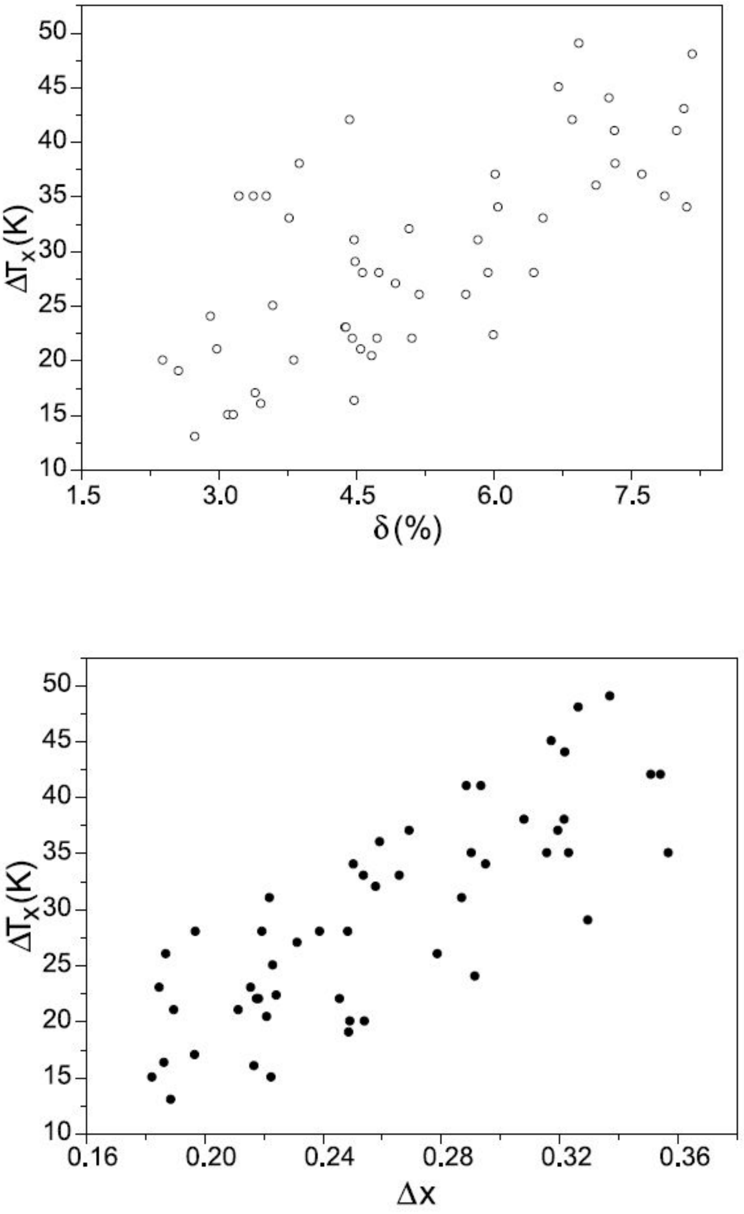

Figure 2.10 The relationship between the bond parameters, including electronegativity difference (ΔX) and atomic size parameters (δ), and the temperature interval of supercooled liquid region (ΔT_x) in Mg-Based bulk metallic glasses [38].

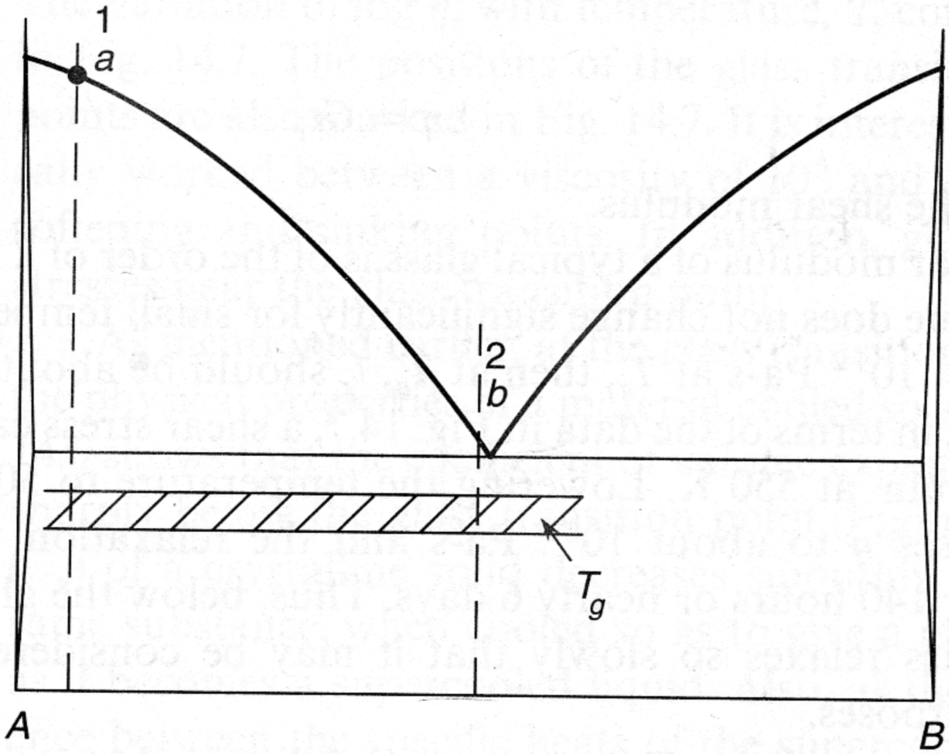

Figure 2.11 A binary phase diagram with a single deep eutectic point.

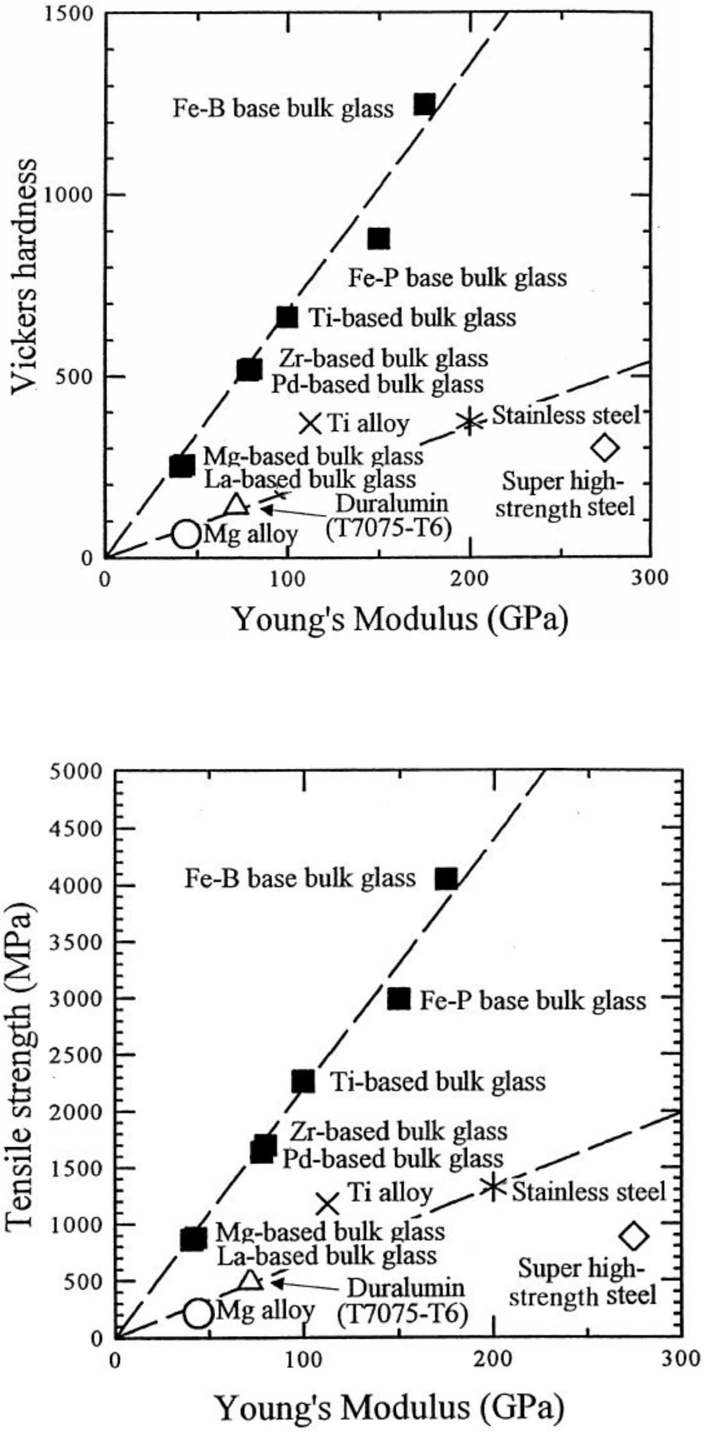

Figure 2.12 Relation between tensile fracture strength, Vickers hardness and Young's modulus for bulk amorphous alloys and conventional crystalline alloys [28].

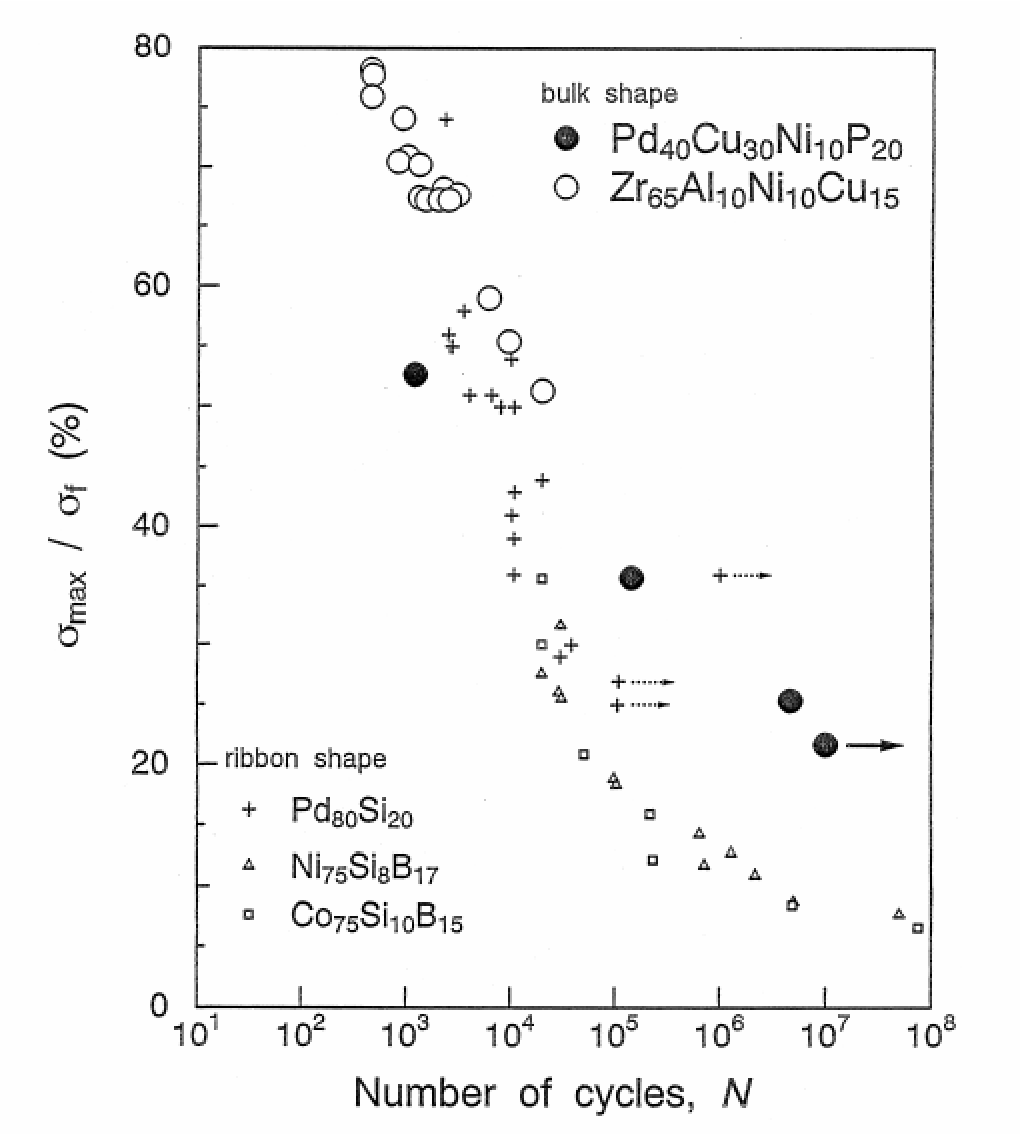

Figure 2.13 Maximum bending and rotating beam fatigue stress as a function of cyclic number up to failure for bulk amorphous $Zr_{65}Al_{10}Ni_{10}Cu_{15}$ and $Pd_{40}Cu_{30}Ni_{10}P_{20}$ alloys. The data for the melt-spun Pd-, Ni- and Co-based amorphous ribbons are also shown for comparison [42].

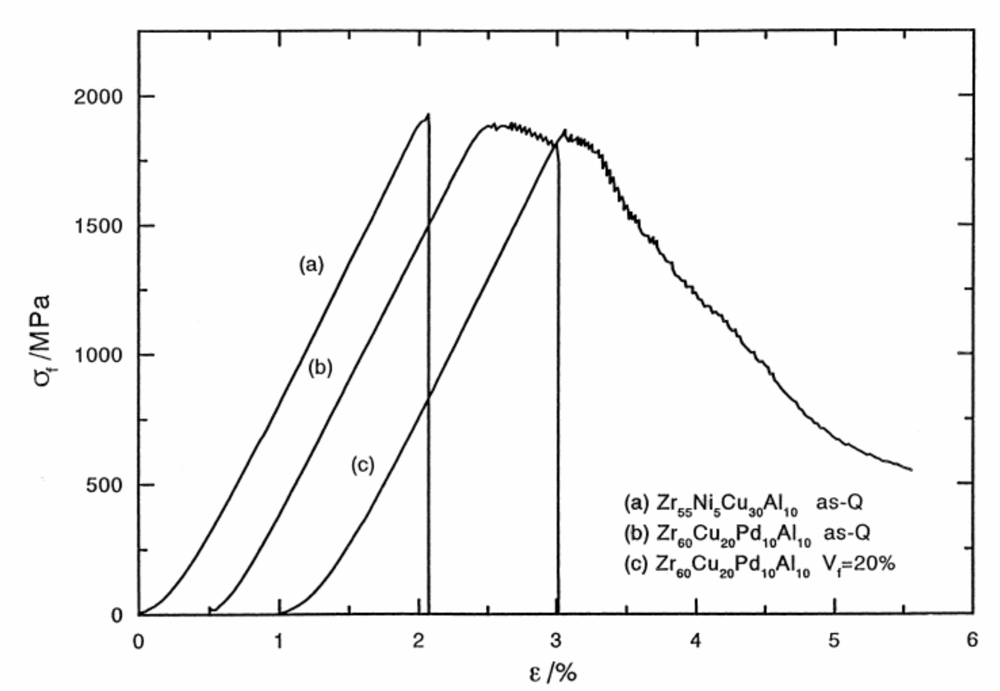

Figure 2.14 The compressive stress-strain curves for the bulk amorphous $Zr_{60}Al_{10}Cu_{20}Pd_{10}$ alloy rod with an amorphous single phase and a mixed structure of amorphous and 20 vol.% $Zr_2(Cu,Pd)$ compound [3].

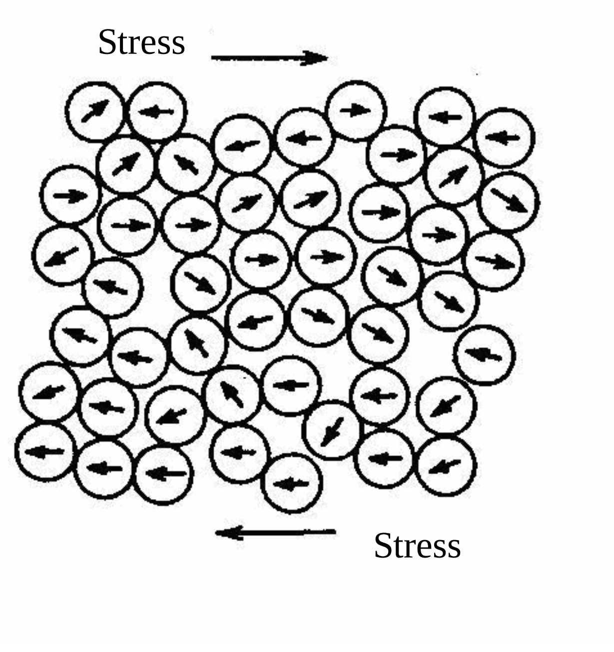

Figure 2.15 The phenomenon of amorphous alloy under an applied stress [49].

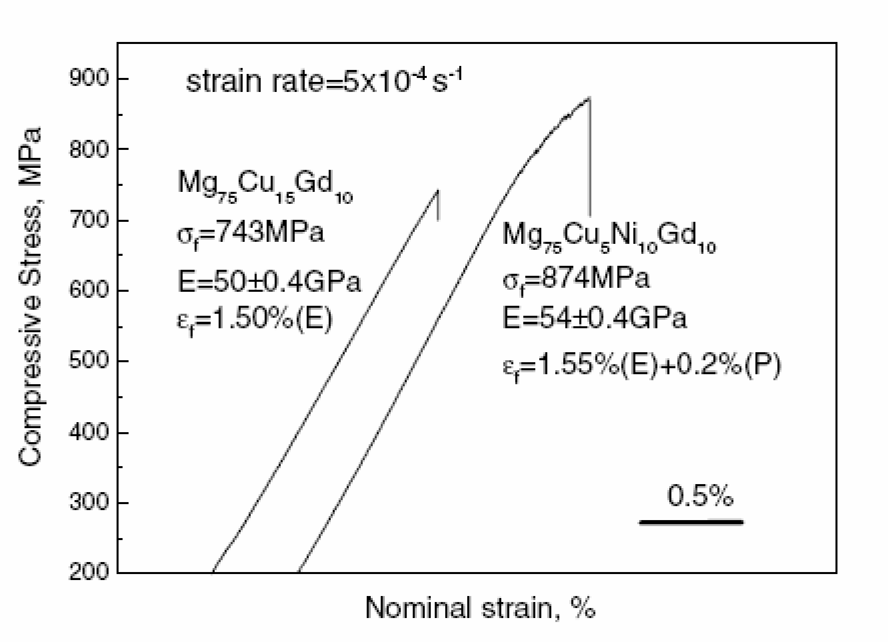

Figure 2.16 Compressive stress-strain curves of $Mg_{75}Cu_{15}Gd_{10}$ and $Mg_{75}Cu_5Ni_{10}Gd_{10}$ glassy rods with a diameter of 2 mm [16].

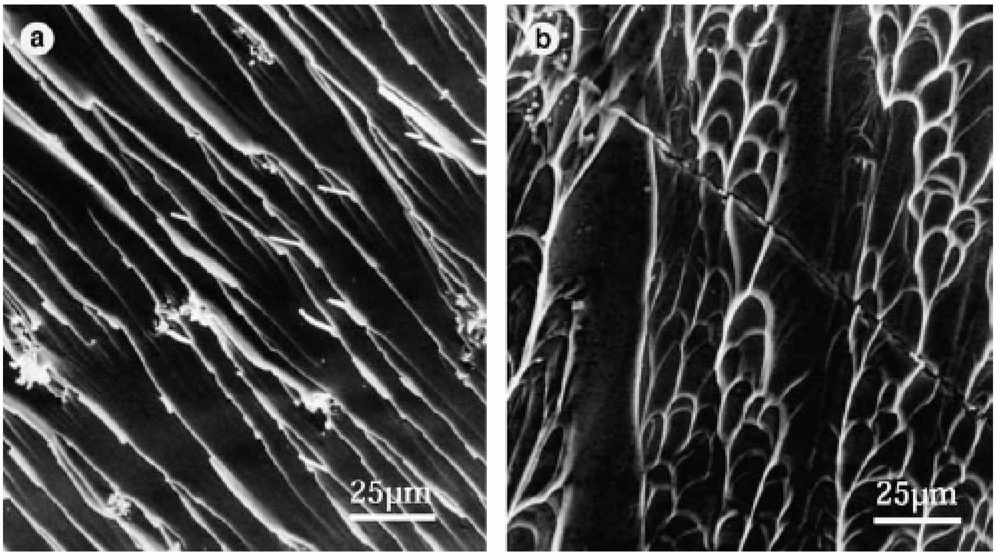

Figure 2.17 SEM revealing the fracture surface appearance of (a) $Mg_{75}Cu_{15}Gd_{10}$ and (b) $Mg_{75}Cu_5Ni_{10}Gd_{10}$ glassy rods [16].

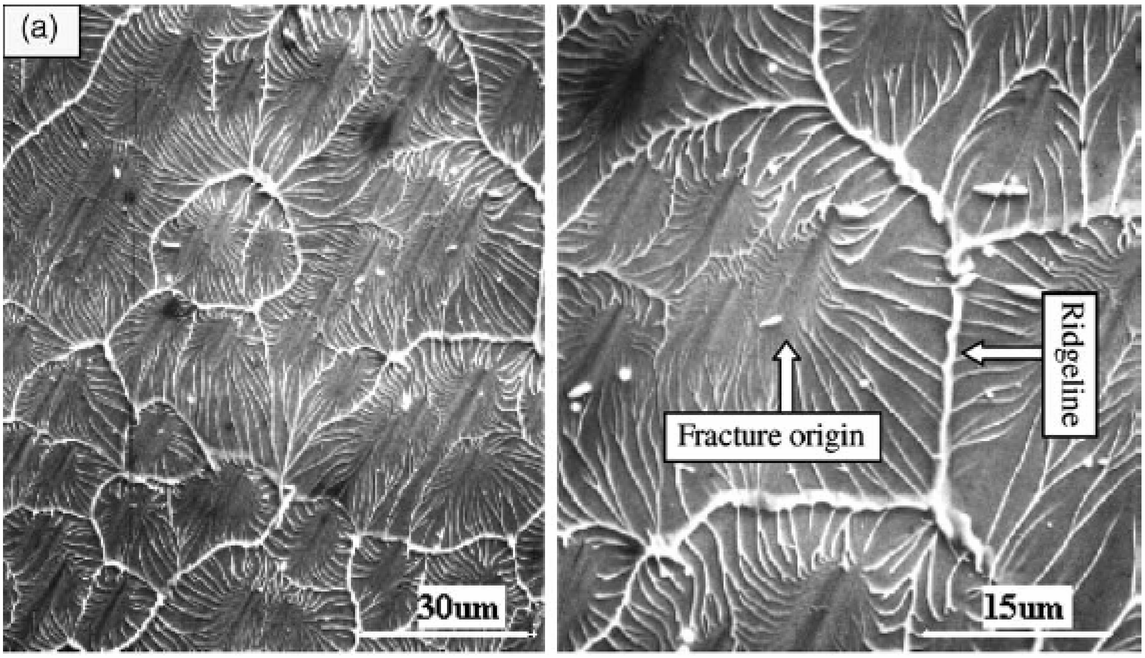

Figure 2.18 The fracture surface morphology of the $Zr_{52.5}Al_{10}Ni10Cu_{15}Be_{12.5}$ bulk metallic glass at low strain rates under the tensile deformation [51].

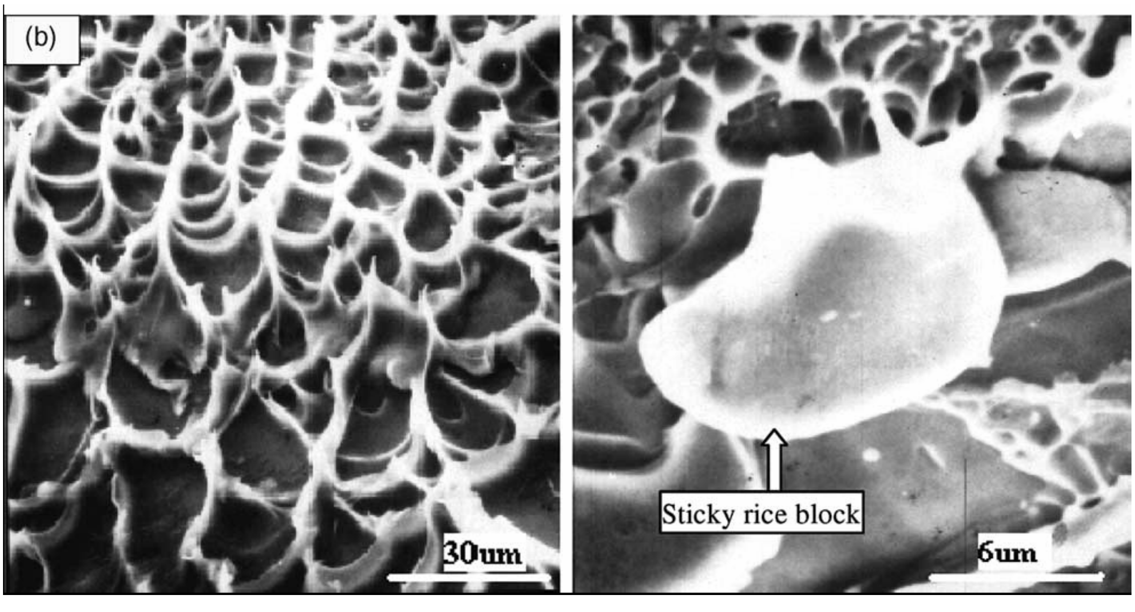

Figure 2.19 The fracture surface morphology of the $Zr_{52.5}Al_{10}Ni10Cu_{15}Be_{12.5}$ bulk metallic glass at high strain rates under the tensile deformation [51].

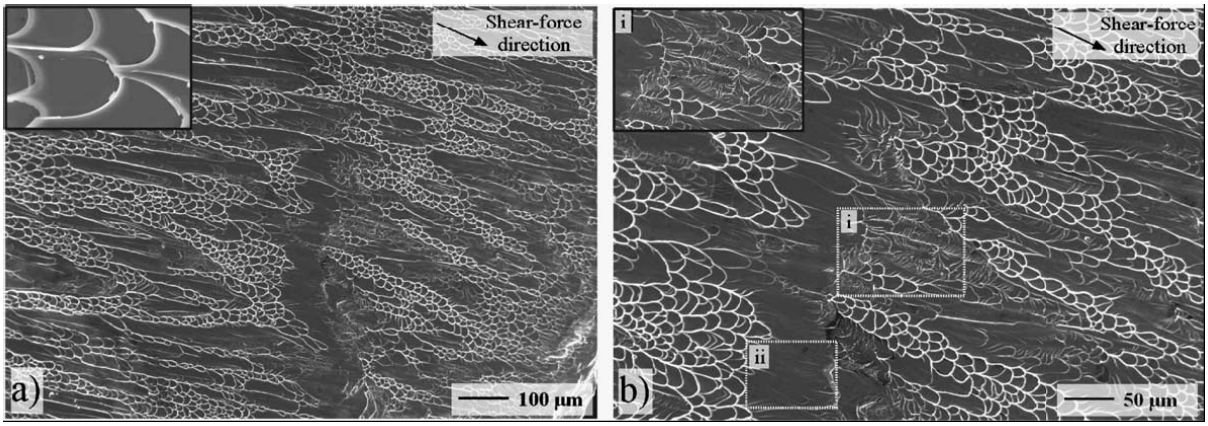

Figure 2.20 The fracture surface morphology of the $Zr_{61}Ti_4Nb_4Cu_{14}Ni_9A_{l9}$ BMGCs after compression test: (a) overview of the fracture surface with regions of different morphologies, the inset shows a detail of the vein-like pattern; (b) enlargement of a region with mixed fracture morphology—vein-like pattern, river-like pattern (frame i) and intermittent smooth regions (frame ii) [52].

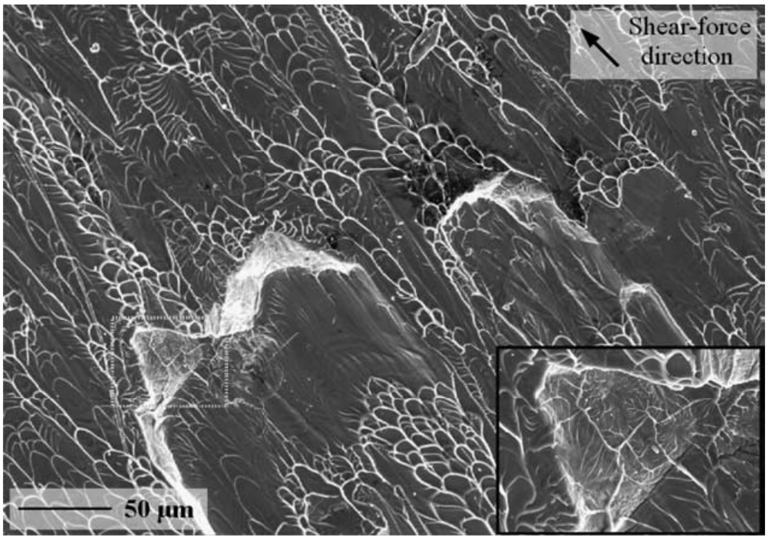

Figure 2.21 The fracture surface morphology of $Cu_{60}Zr_{20}Ti_{20}$ under compression testing. Inset shows the transversal step with the river-like morphology [52].

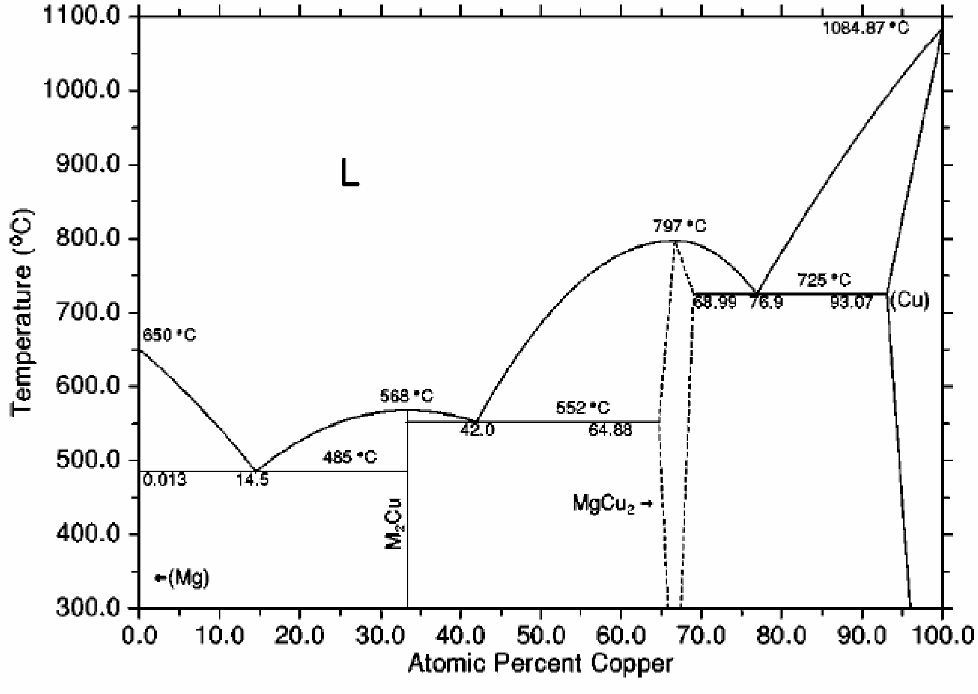

Figure 3.1 The Mg-Cu binary phase diagram.

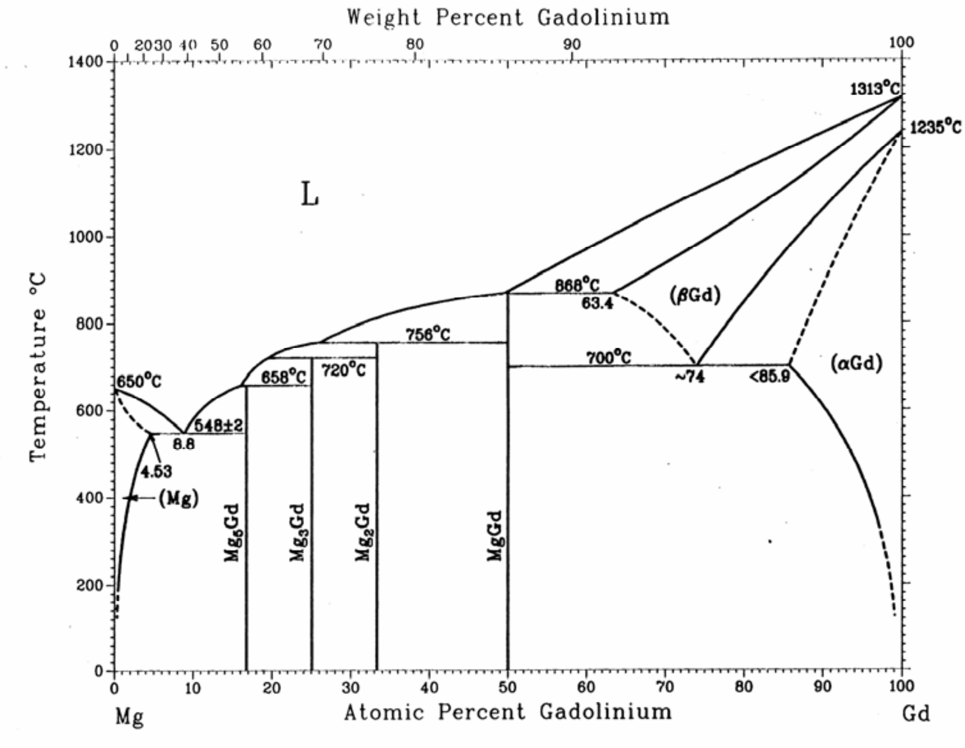

Figure 3.2 The Mg-Gd binary phase diagram.

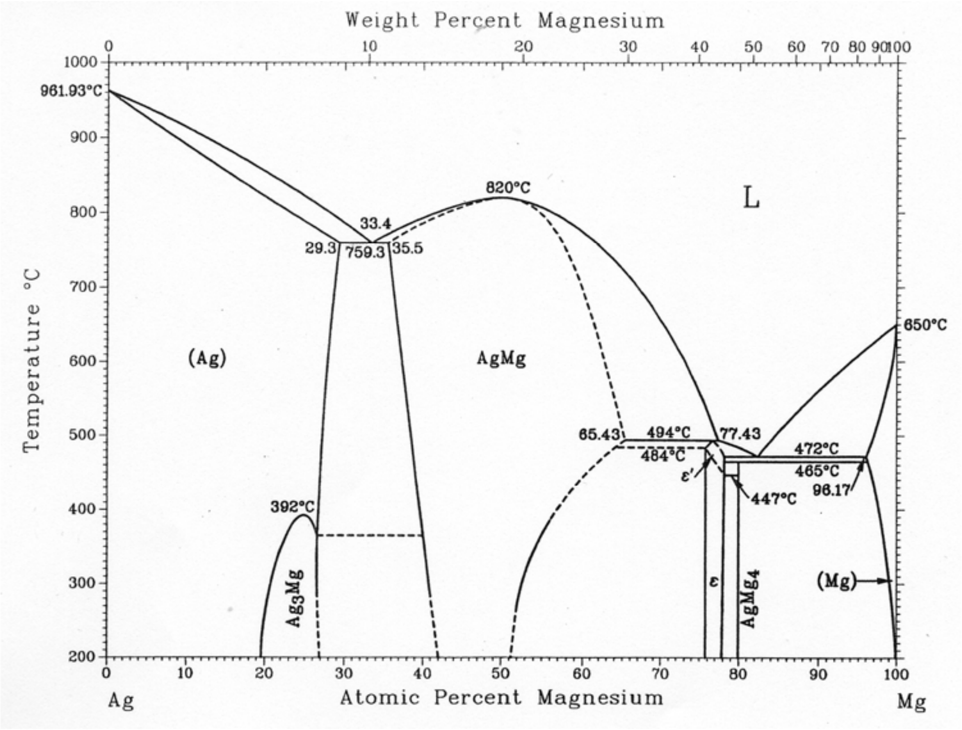

Figure 3.3 The Mg-Ag binary phase diagram.

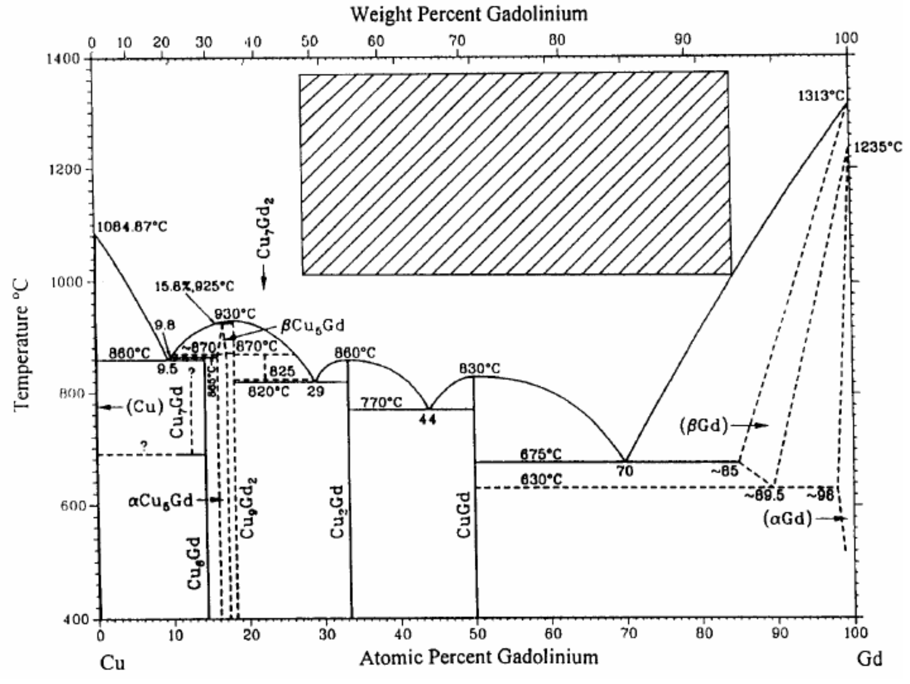

Figure 3.4 The Cu-Gd binary phase diagram.

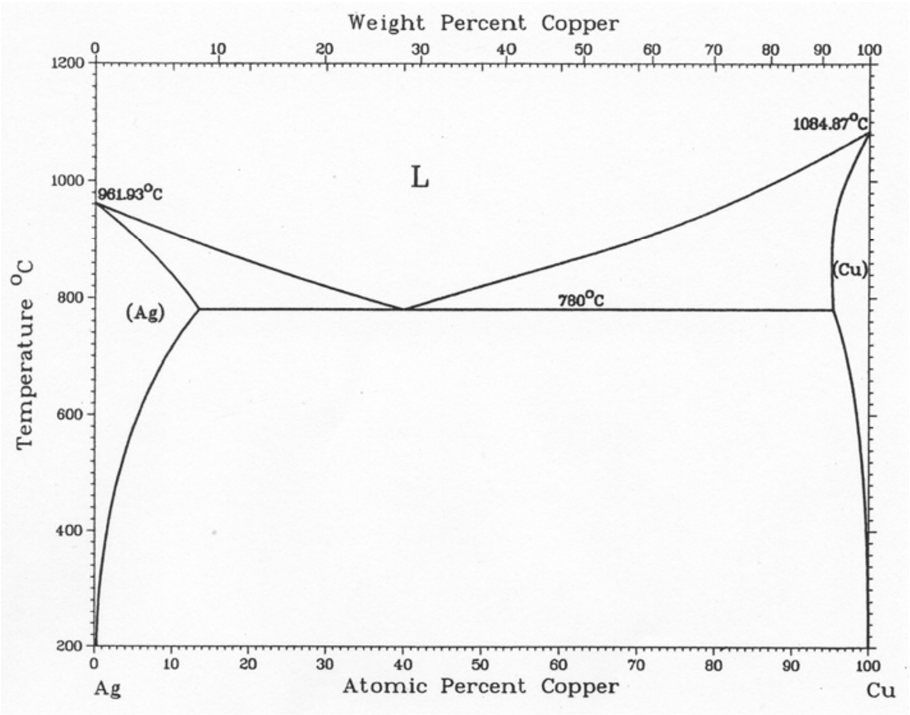

Figure 3.5 The Cu-Ag binary phase diagram.

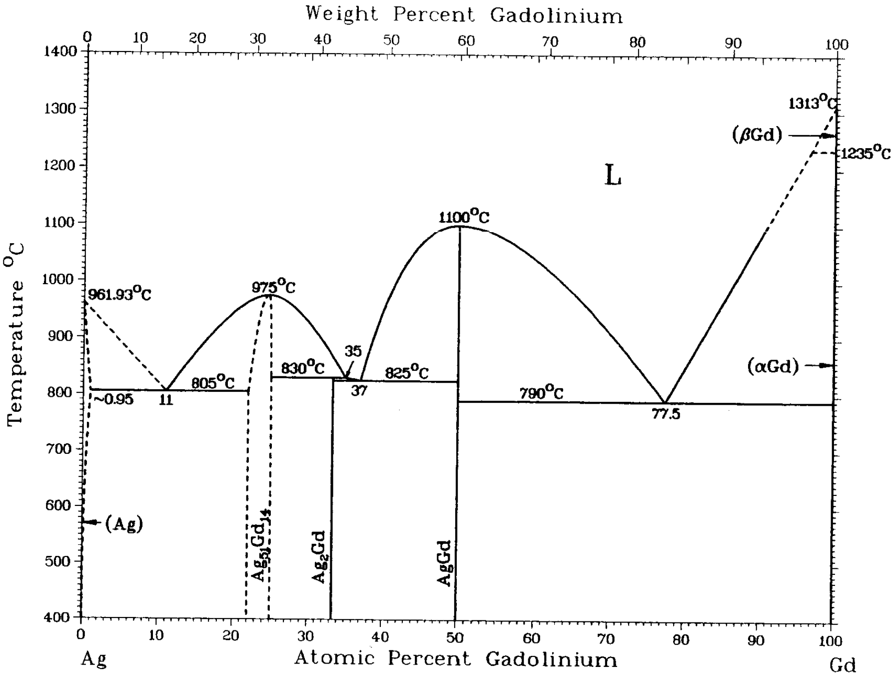

Figure 3.6 The Gd-Ag binary phase diagram.

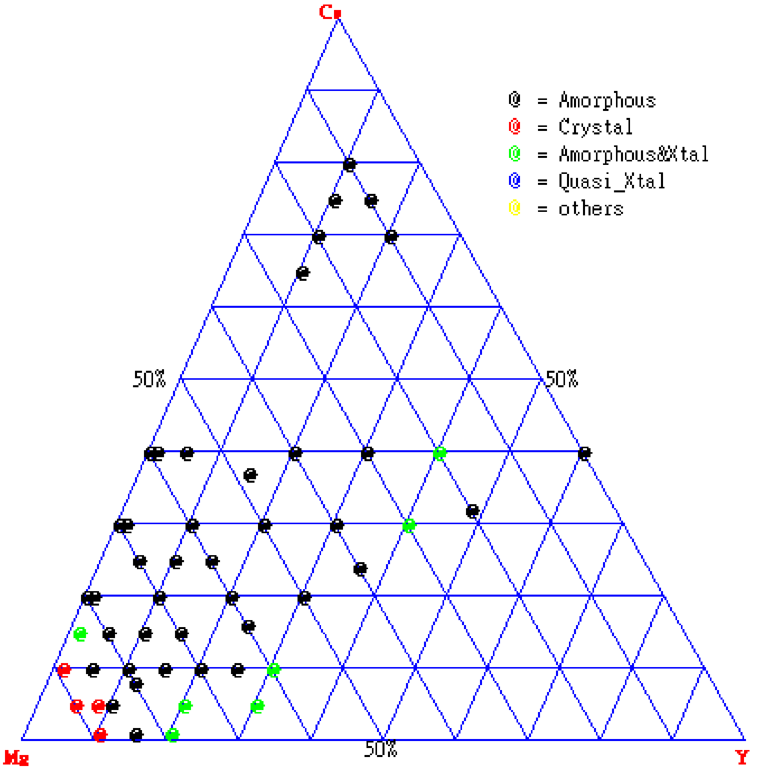

Figure 3.7 The amorphous ternary graphics of the Mg-Cu-Y system

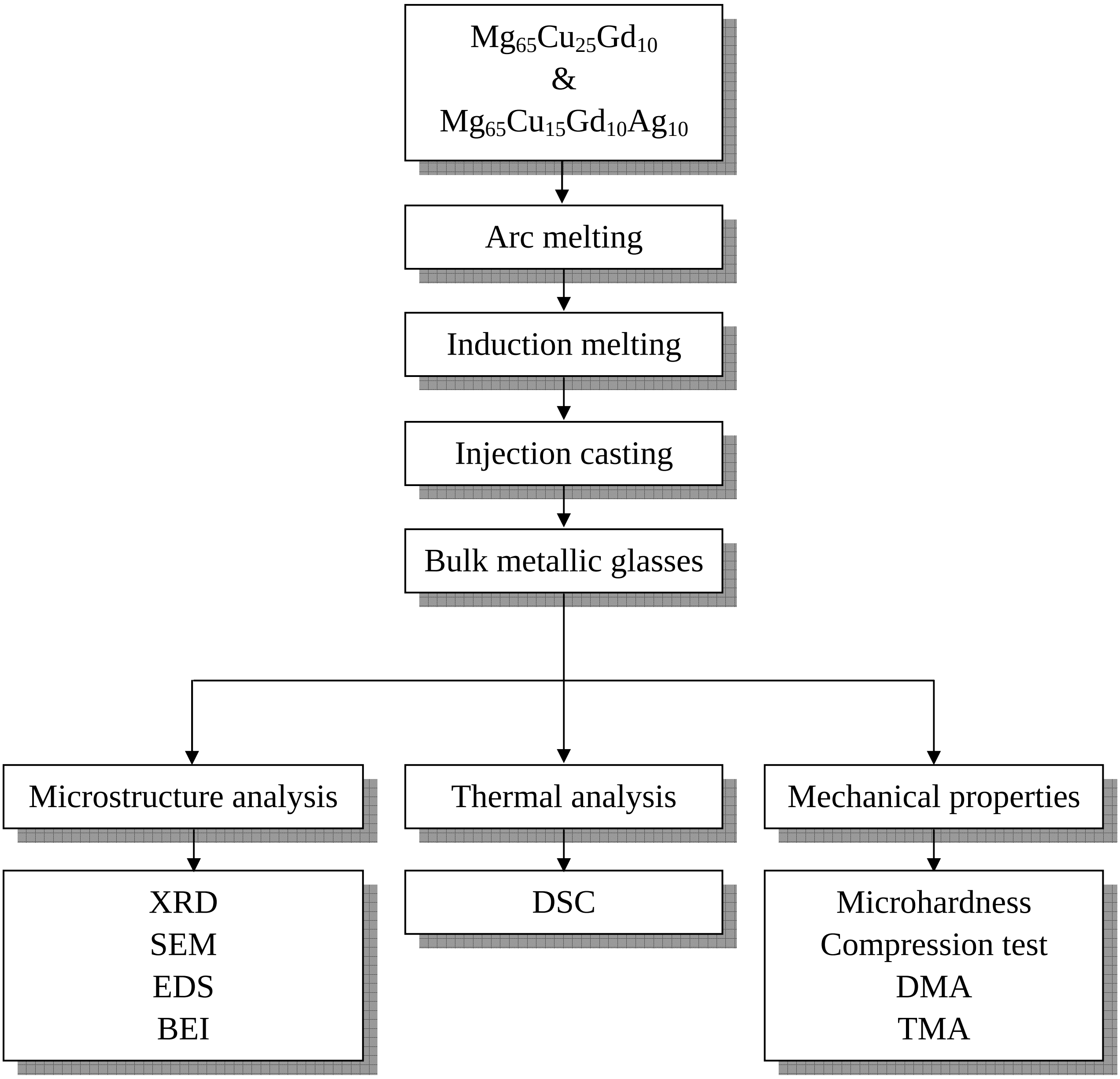

Figure 3.8 The flow chart of the experimental procedures.

Figure 3.9   Photograph of the arc melting device.

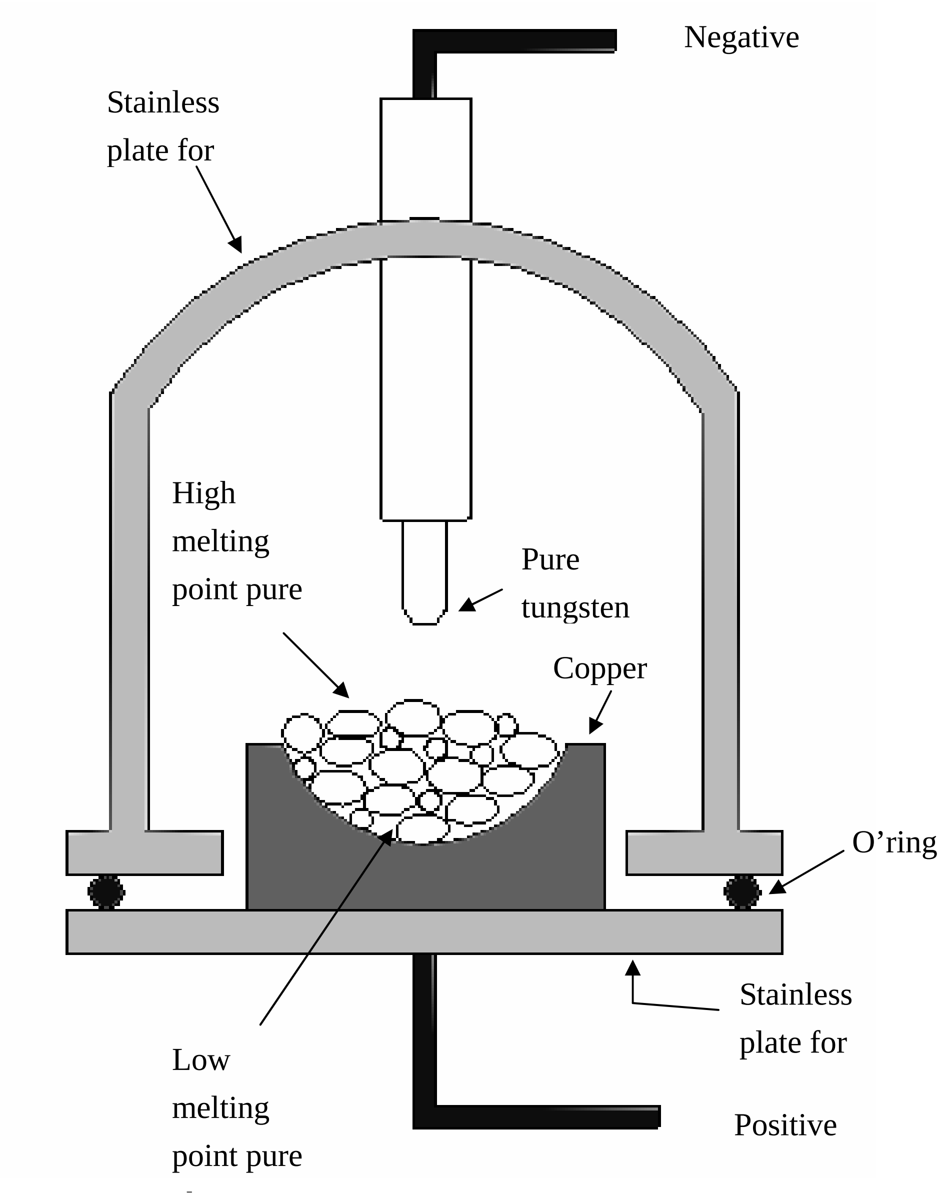

Figure 3.10 The schematic diagram of the arc melting device.

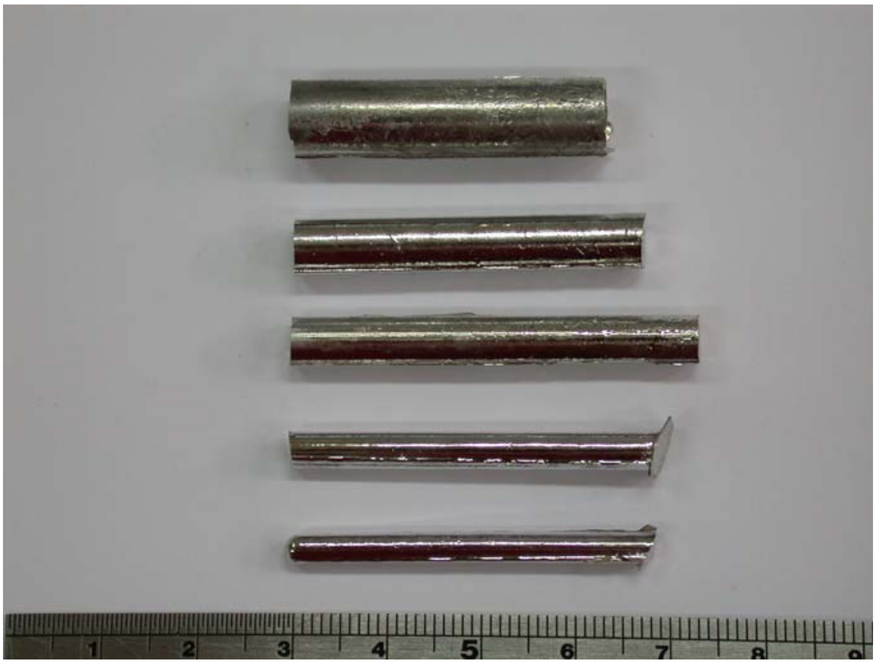

Figure 4.1 The surface appearance of the injection cast $Mg_{65}Cu_{25}Gd_{10}$ rods with the diameter from 3 to 8 mm.

Figure 4.2 The surface appearance of the injection cast $Mg_{65}Cu_{15}Ag_{10}Gd_{10}$ rods with the diameter from 3 to 6 mm.

Figure 4.3 The cross-sectional surface appearance of injection cast $Mg_{65}Cu_{25}Gd_{10}$ rods with the diameter of 4 mm.

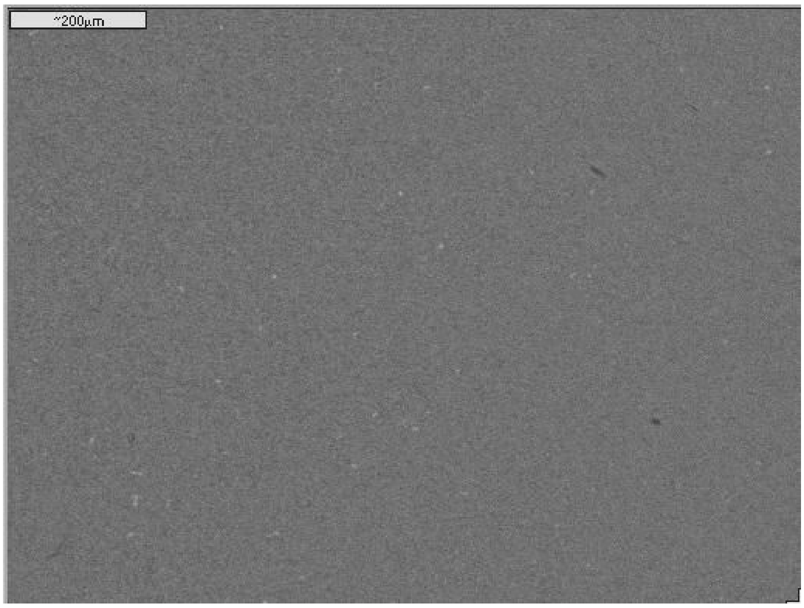

(a) BEI image (100X)

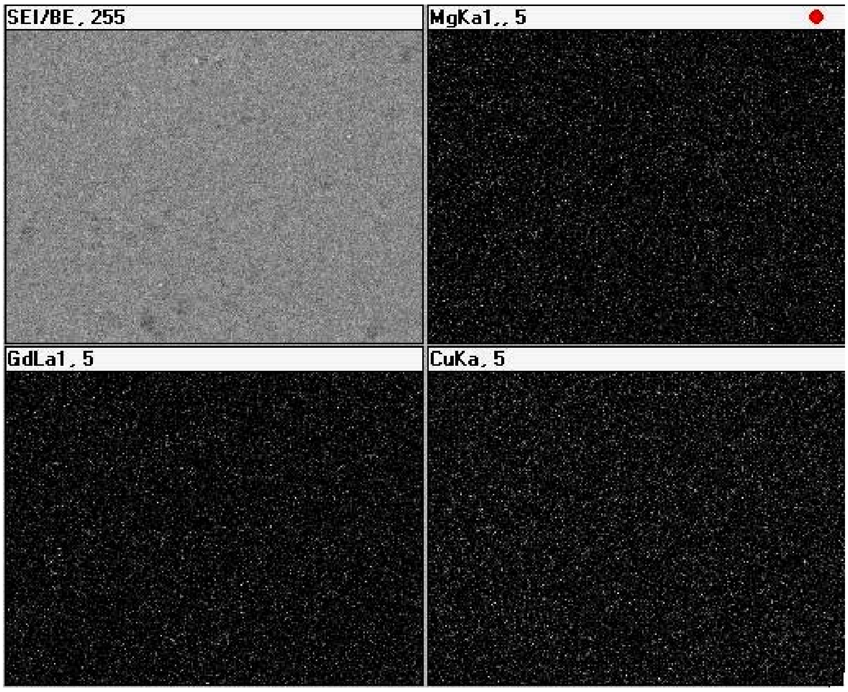

(b) Mapping image (100X)

Figure 4.4 The SEM morphology of the injection cast $Mg_{65}Cu_{25}Gd_{10}$ BMG with the diameter of 4 mm.

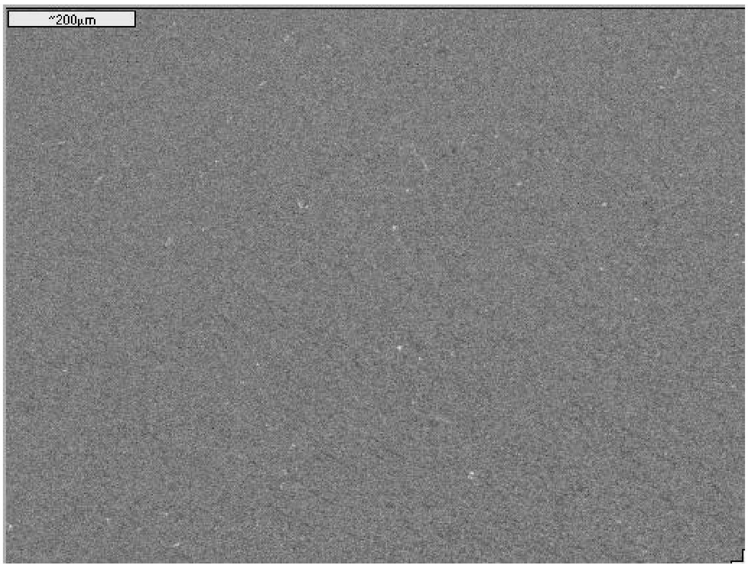

(a) BEI image (100X)

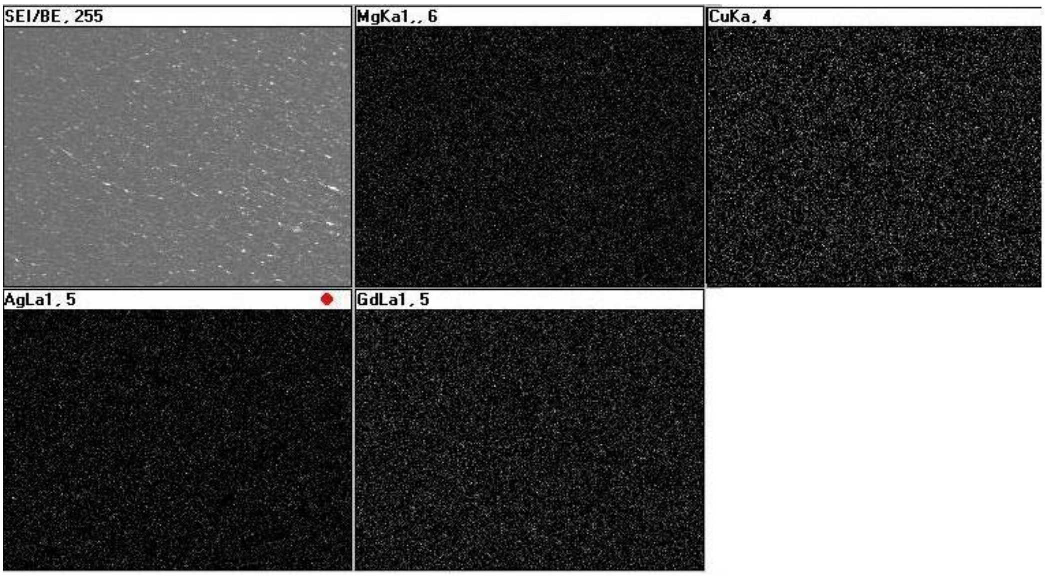

(b) Mapping image (100X)

Figure 4.5 The SEM morphology of the injection cast $Mg_{65}Cu_{15}Ag_{10}Gd_{10}$ BMG with the diameter of 4 mm.

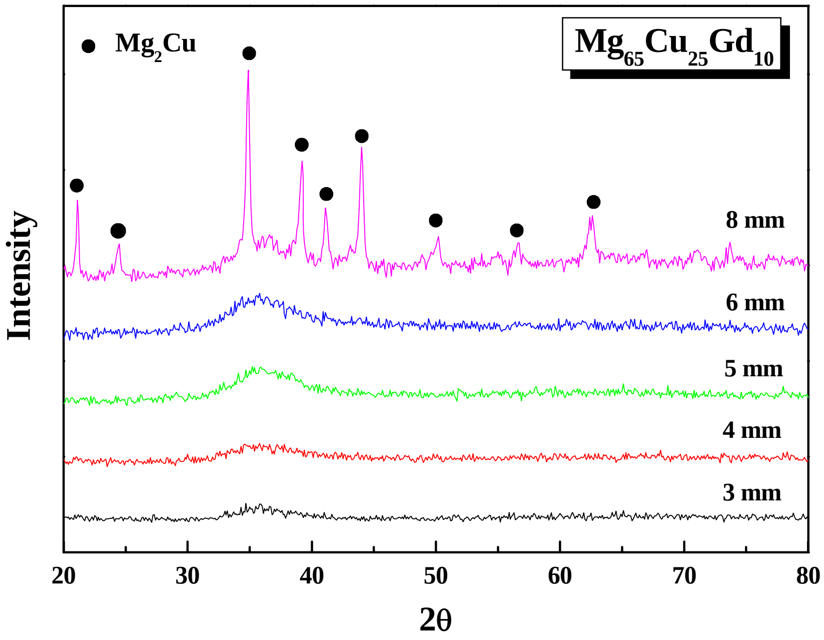

Figure 4.6 XRD patterns of the injection cast $Mg_{65}Cu_{25}Gd_{10}$ BMGs with the diameter from 3 to 8 mm.

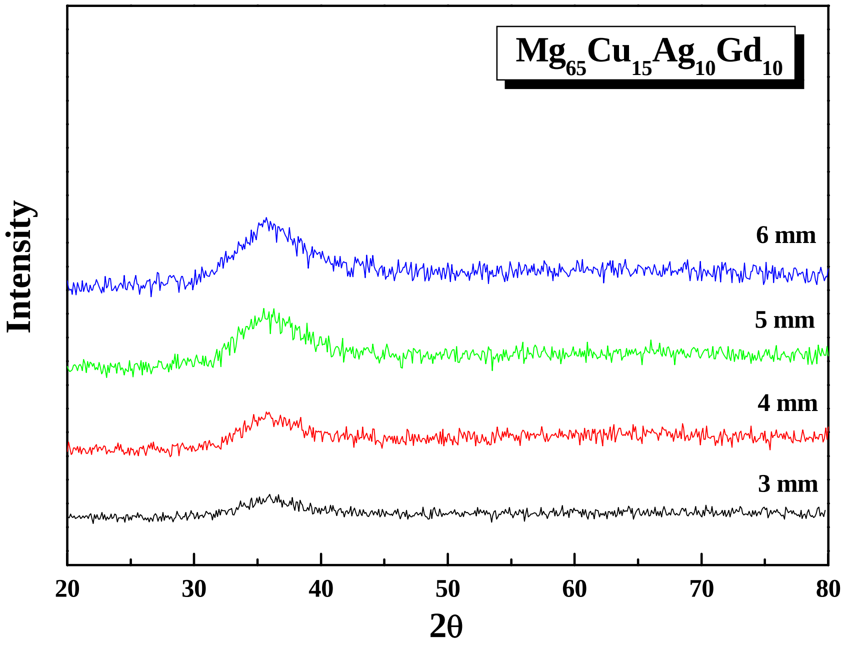

Figure 4.7 XRD patterns of the injection cast $Mg_{65}Cu_{15}Ag_{10}Gd_{10}$ BMGs with the diameter from 3 to 6 mm.

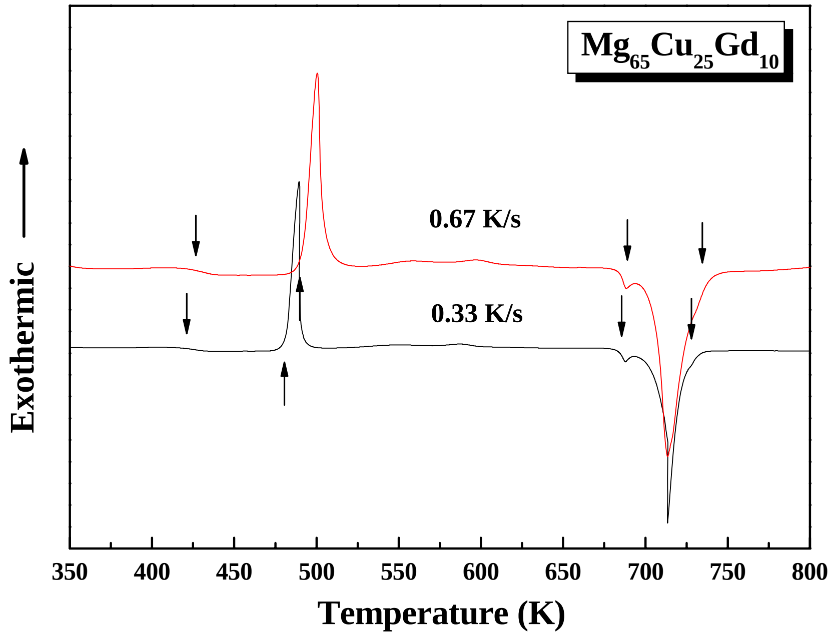

Figure 4.8 DSC traces of the injection cast $Mg_{65}Cu_{25}Gd_{10}$ BMGs.

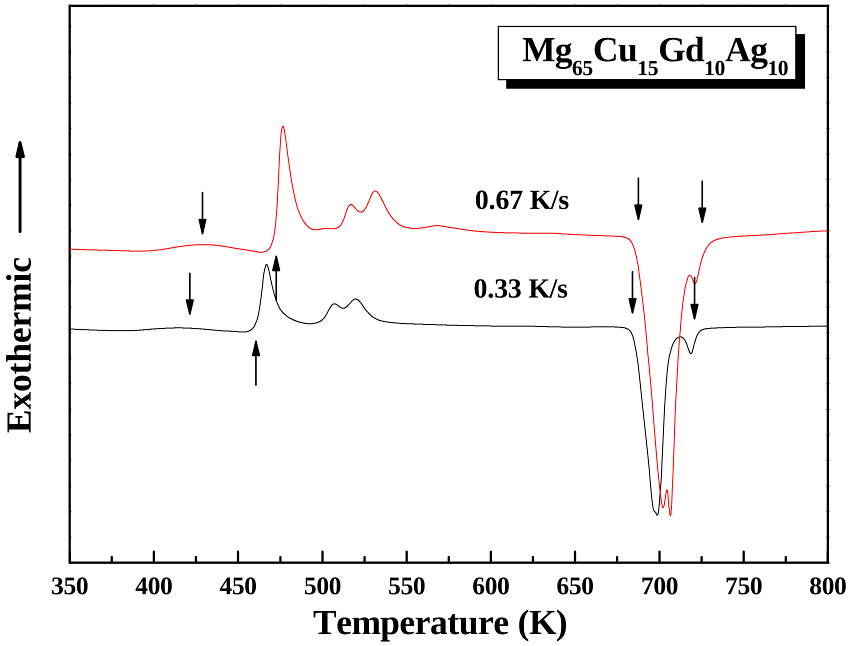

Figure 4.9 DSC traces of the injection cast $Mg_{65}Cu_{15}Ag_{10}Gd_{10}$ BMGs

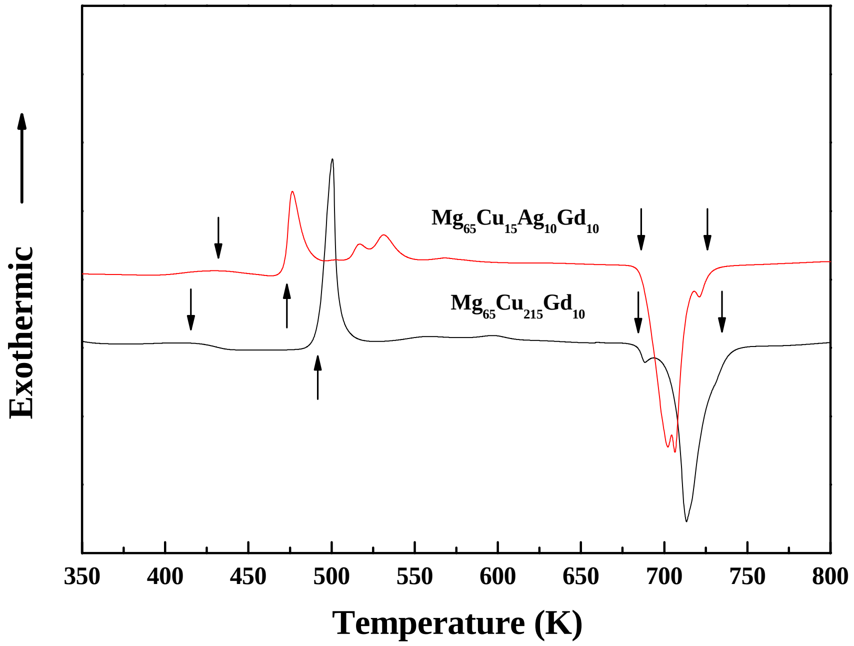

Figure 4.10 DSC traces of the injection cast $Mg_{65}Cu_{25}Gd_{10}$ and $Mg_{65}Cu_{15}Ag_{10}Gd_{10}$ BMGs at the heating rate of 0.67 K/s.

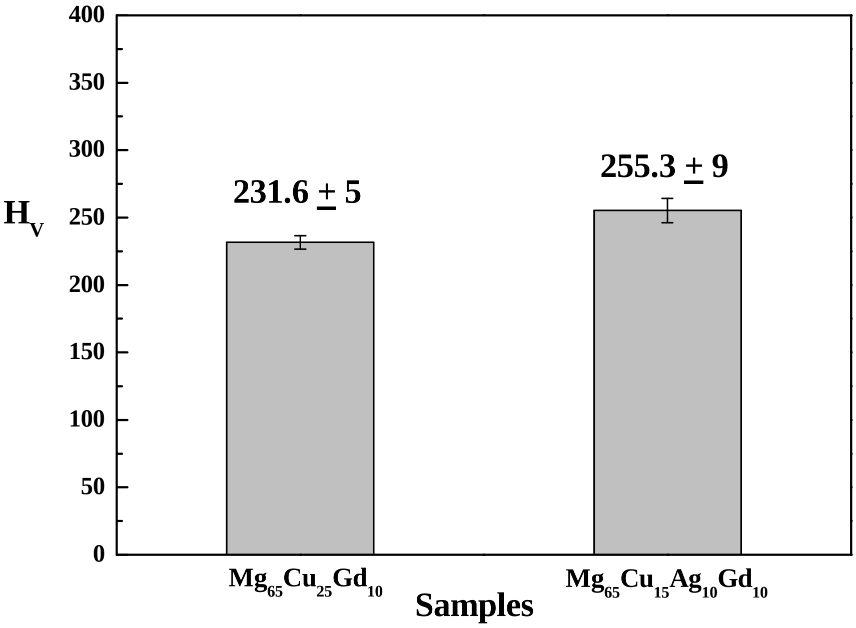

Figure 4.11 Hardness of the injection cast $Mg_{65}Cu_{25}Gd_{10}$ and $Mg_{65}Cu_{15}Ag_{10}Gd_{10}$ BMGs.

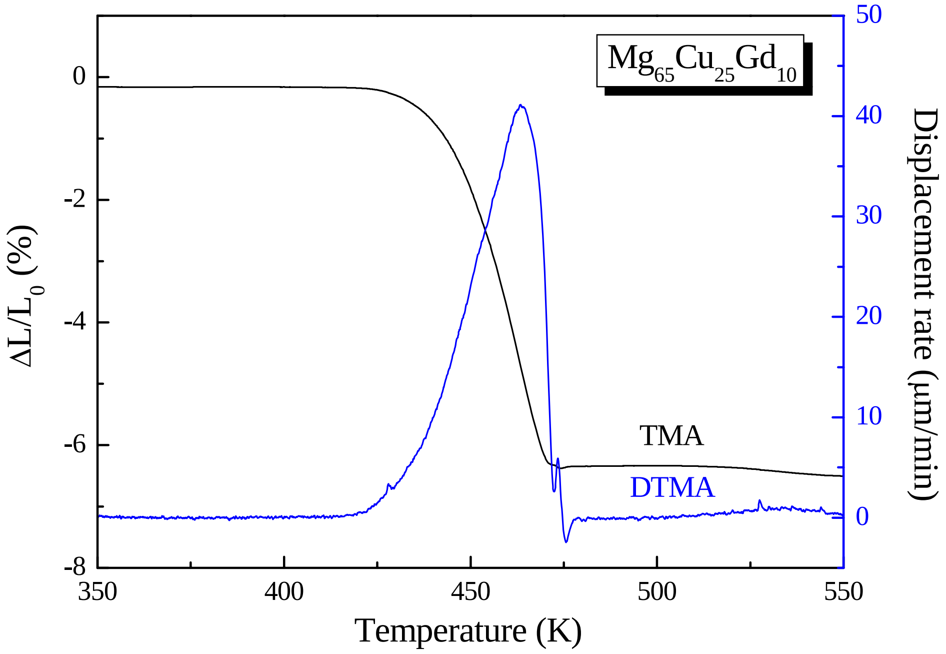

Figure 4.12 Typical TMA and DTMA curves of the injection cast $Mg_{65}Cu_{25}Gd_{10}$ BMGs.

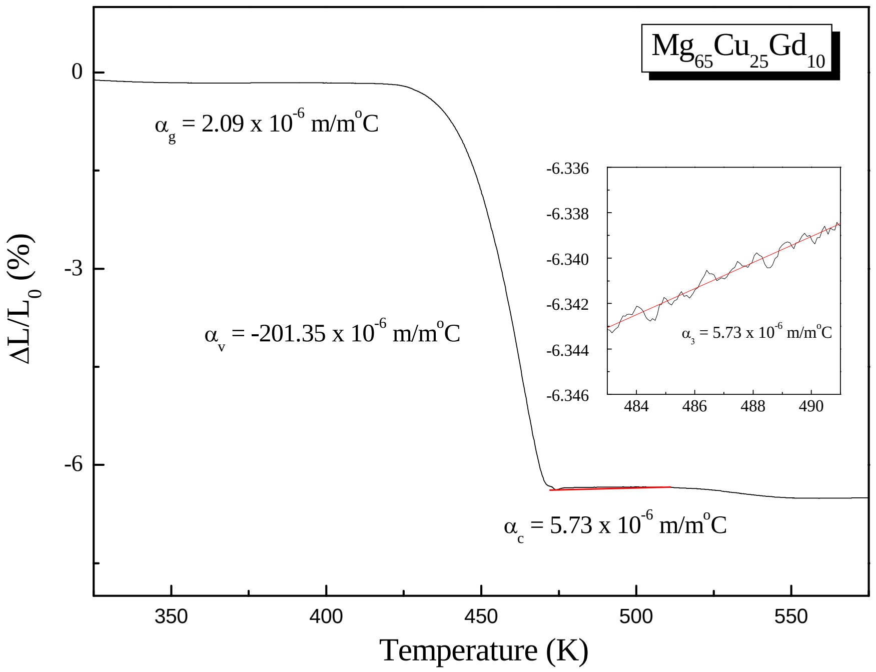

Figure 4.13 The thermal expansion behavior of the injection cast $Mg_{65}Cu_{25}Gd_{10}$ BMGs.

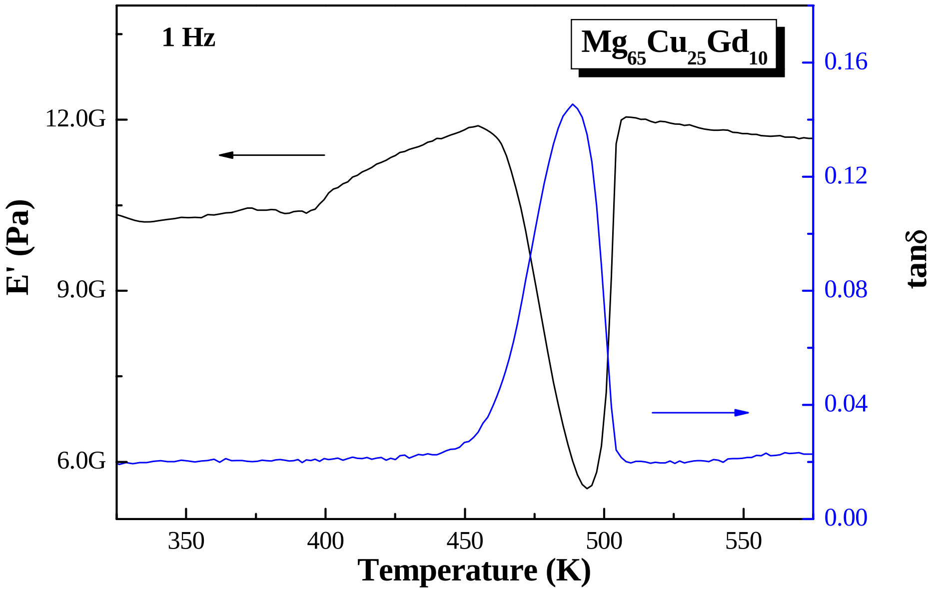

Figure 4.14 DMA curves of the injection cast $Mg_{65}Cu_{25}Gd_{10}$ BMGs.

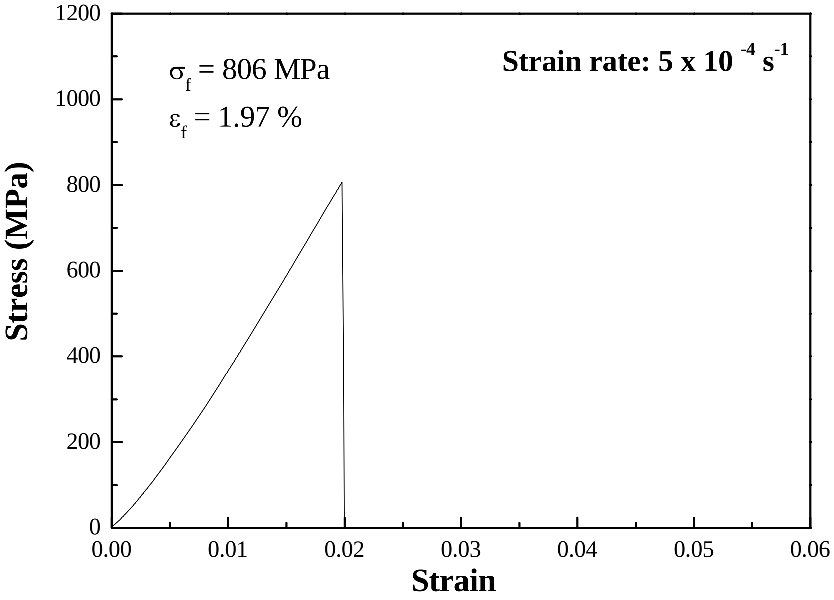

Figure 4.15 The compressive stress-strain curve of the injection cast $Mg_{65}Cu_{25}Gd_{10}$ BMGs with the h/d ratio of 2 (H = 8 mm and D = 4 mm) at strain rate of 5 x 10^{-4} s^{-1}.

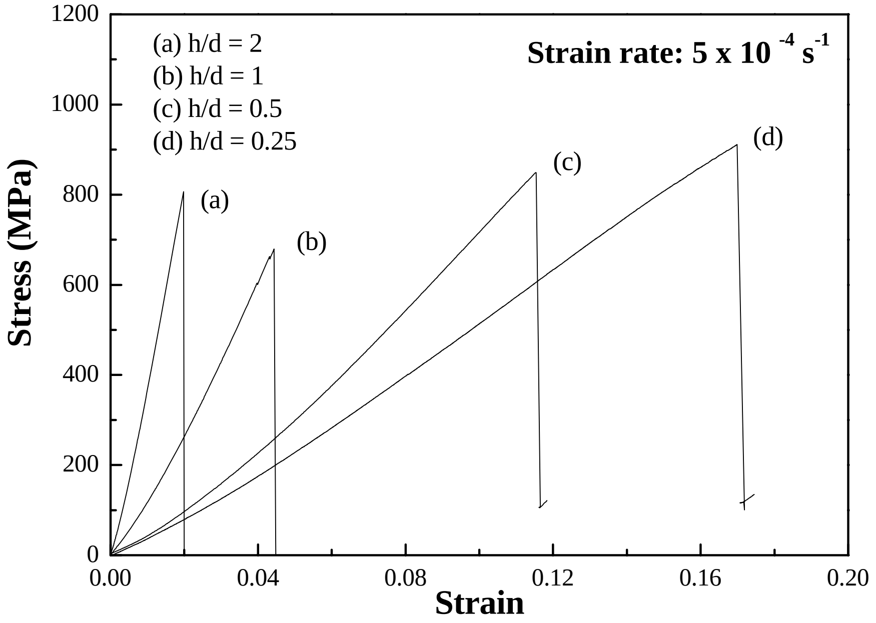

Figure 4.16 The compressive stress-strain curve of the injection cast $Mg_{65}Cu_{25}Gd_{10}$ BMGs with various h/d ratios from 2, 1, 0.5 to 0.25 at strain rate of 5 x 10^{-4} s^{-1}.

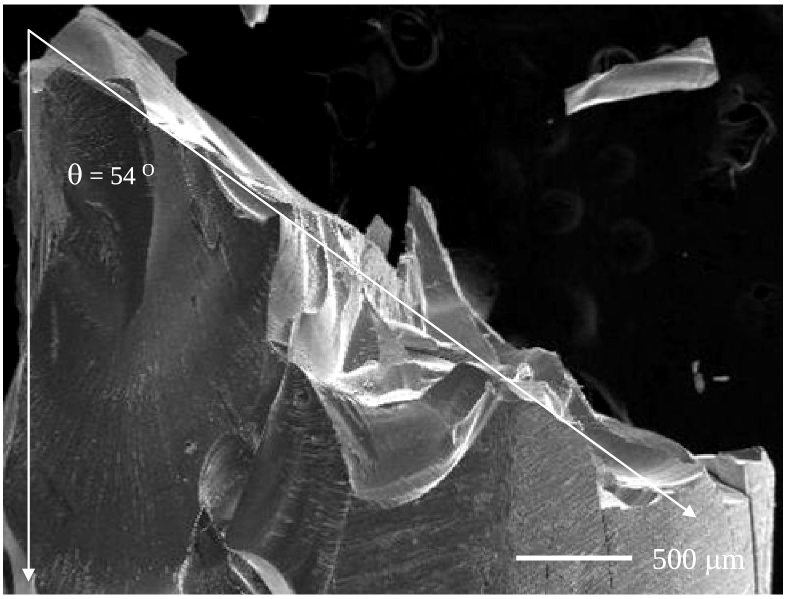

Figure 4.17 The outer appearance showing fracture plane inclination of the $Mg_{65}Cu_{25}Gd_{10}$ BMG with a h/d ratio of 2.

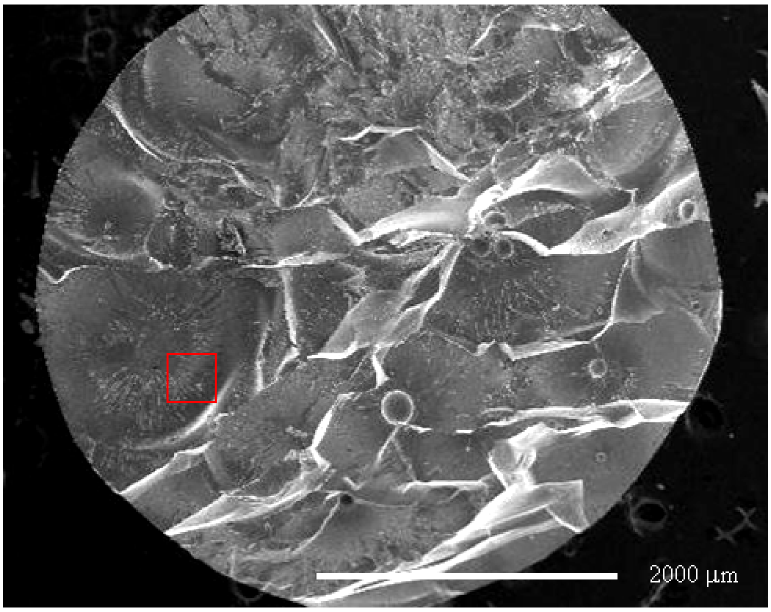

Figure 4.18 The fracture surface morphology of the $Mg_{65}Cu_{25}Gd_{10}$ BMG with a h/d ratio of 2.

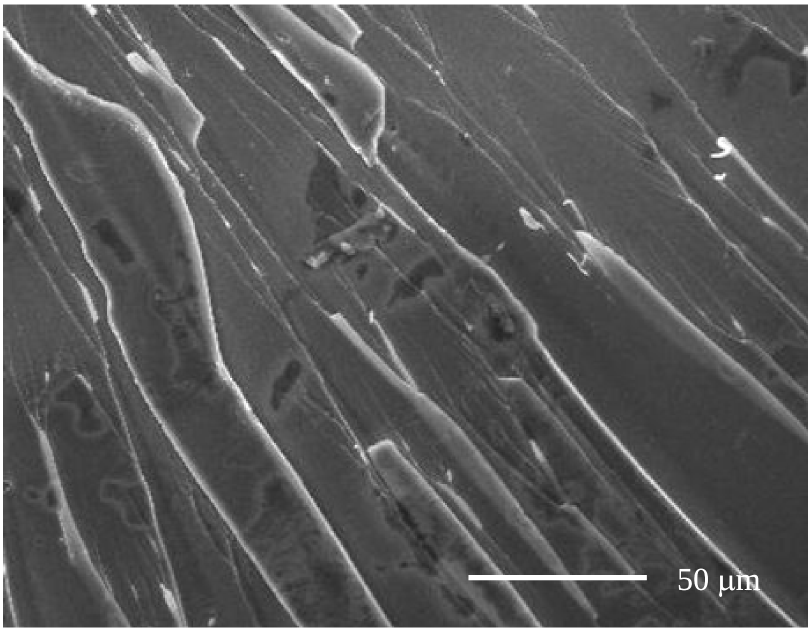

Figure 4.19 The fracture surface morphology of the $Mg_{65}Cu_{25}Gd_{10}$ BMG with a h/d ratio of 2.

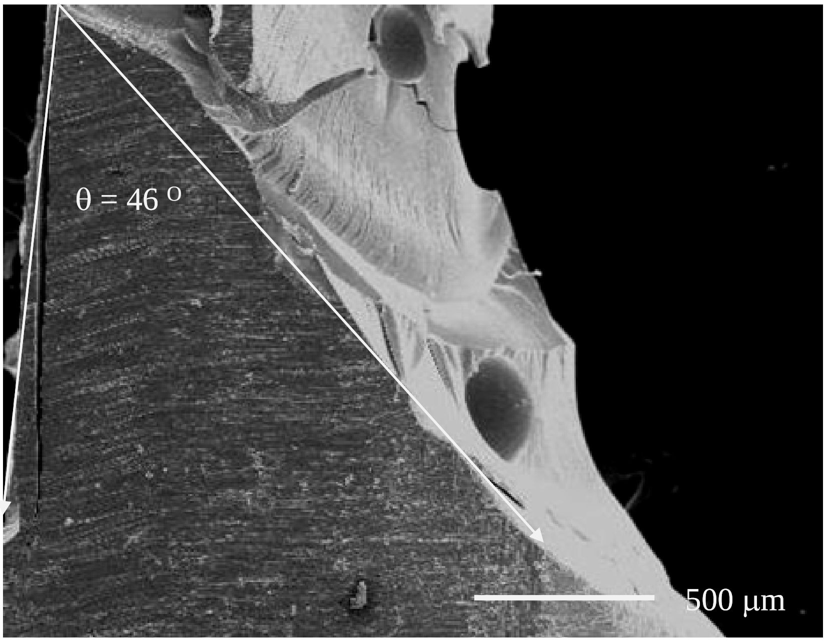

Figure 4.20 The outer appearance showing fracture plane inclination of the $Mg_{65}Cu_{25}Gd_{10}$ BMG with a h/d ratio of 1.

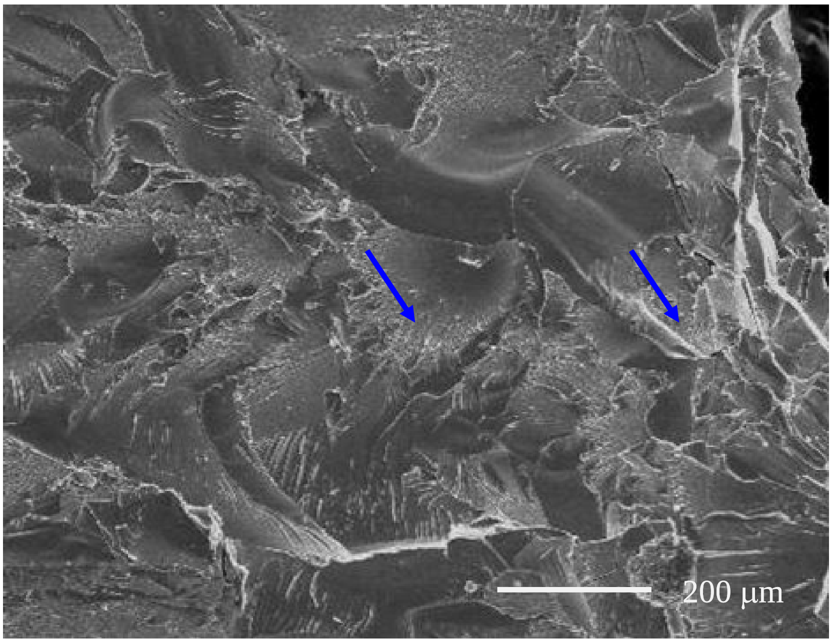

Figure 4.21 The fracture surface morphology of the $Mg_{65}Cu_{25}Gd_{10}$ BMG with a h/d ratio of 1.

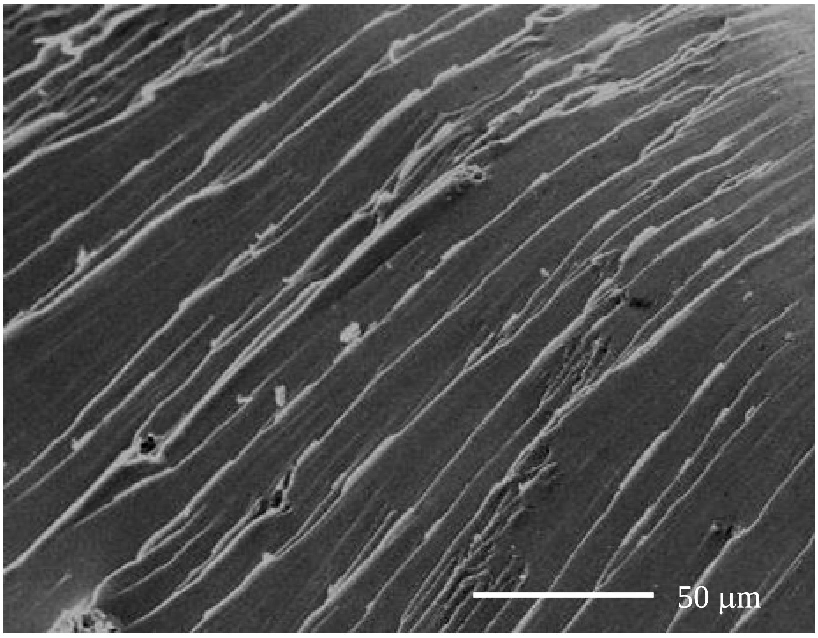

Figure 4.22 The fracture surface morphology of the $Mg_{65}Cu_{25}Gd_{10}$ BMG with a h/d ratio of 1.

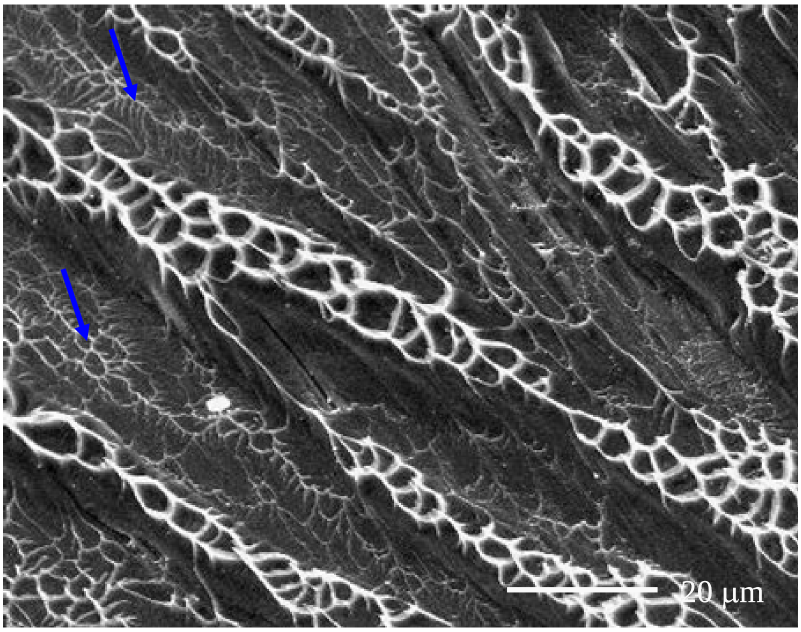

Figure 4.23 The fracture surface morphology of the $Mg_{65}Cu_{25}Gd_{10}$ BMG with a h/d ratio of 1.

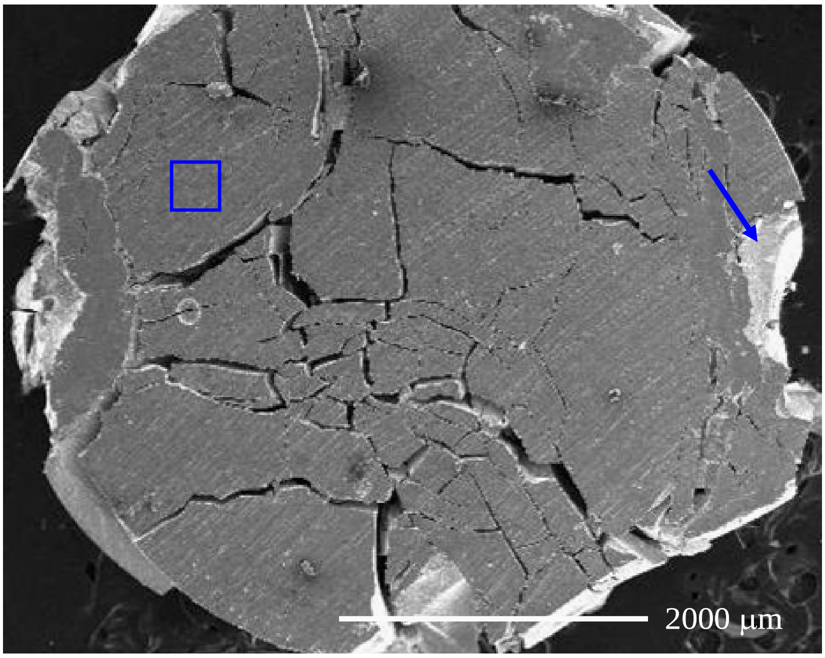

Figure 4.24 The outer appearance showing fracture plane of the $Mg_{65}Cu_{25}Gd_{10}$ BMG with a h/d ratio of 0.5.

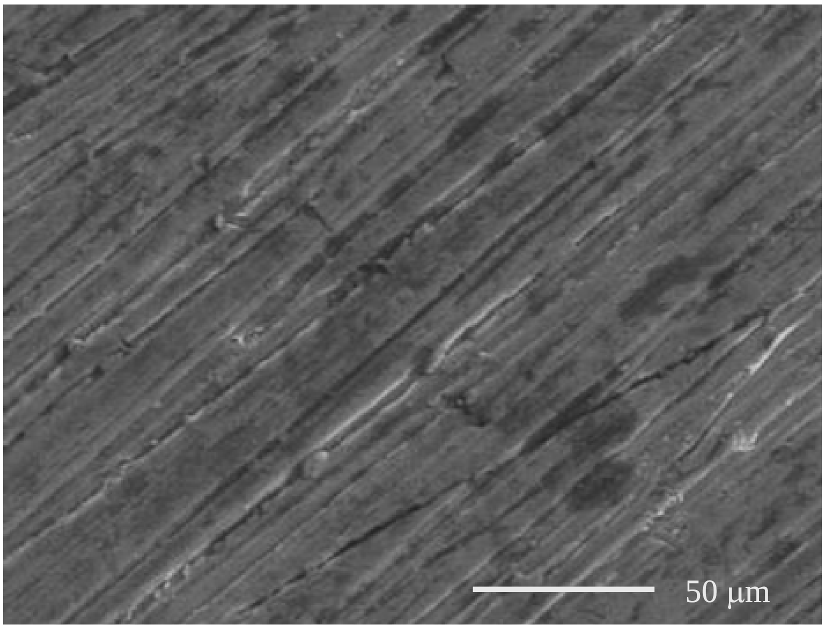

Figure 4.25 The fracture surface morphology of the $Mg_{65}Cu_{25}Gd_{10}$ BMG with a h/d ratio of 0.5.

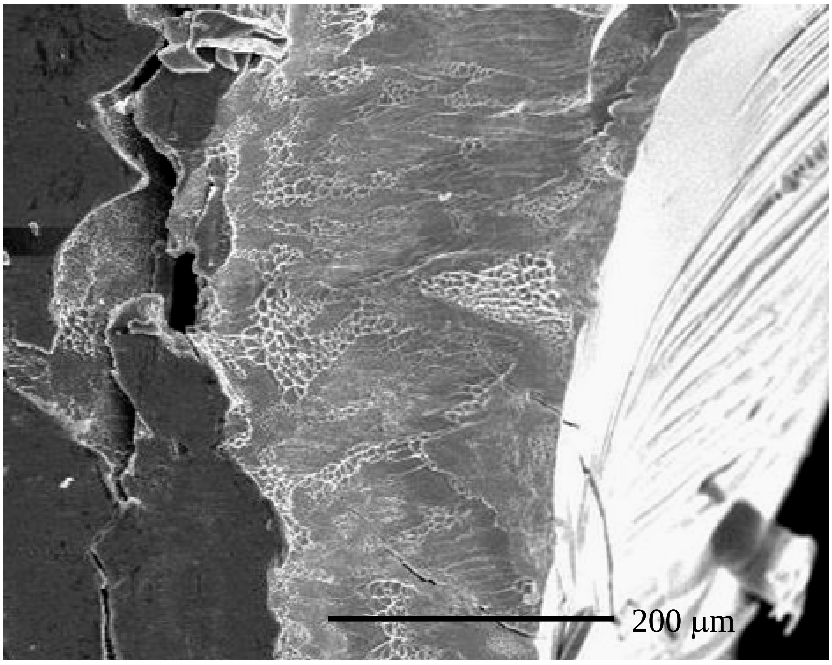

Figure 4.26 The fracture surface morphology of the $Mg_{65}Cu_{25}Gd_{10}$ BMG with a h/d ratio of 0.5.

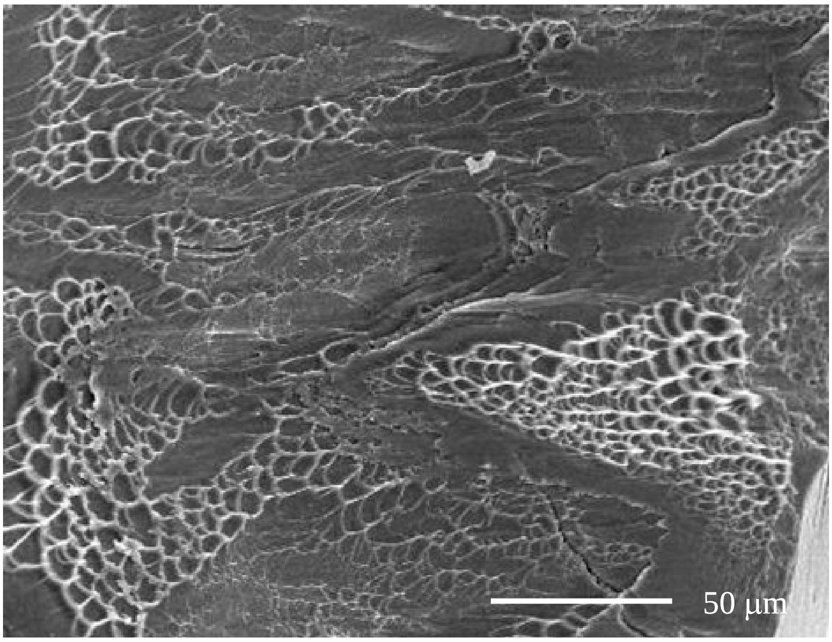

Figure 4.27 The fracture surface morphology of the $Mg_{65}Cu_{25}Gd_{10}$ BMG with a h/d ratio of 0.5.

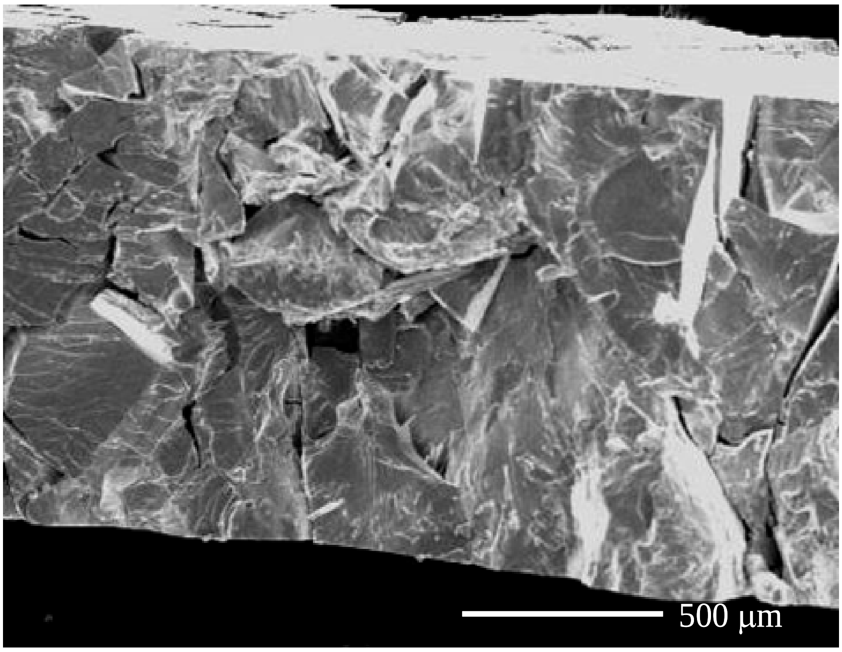

Figure 4.28 The cross-sectional view showing fracture morphology of the $Mg_{65}Cu_{25}Gd_{10}$ BMG with a h/d ratio of 0.5.

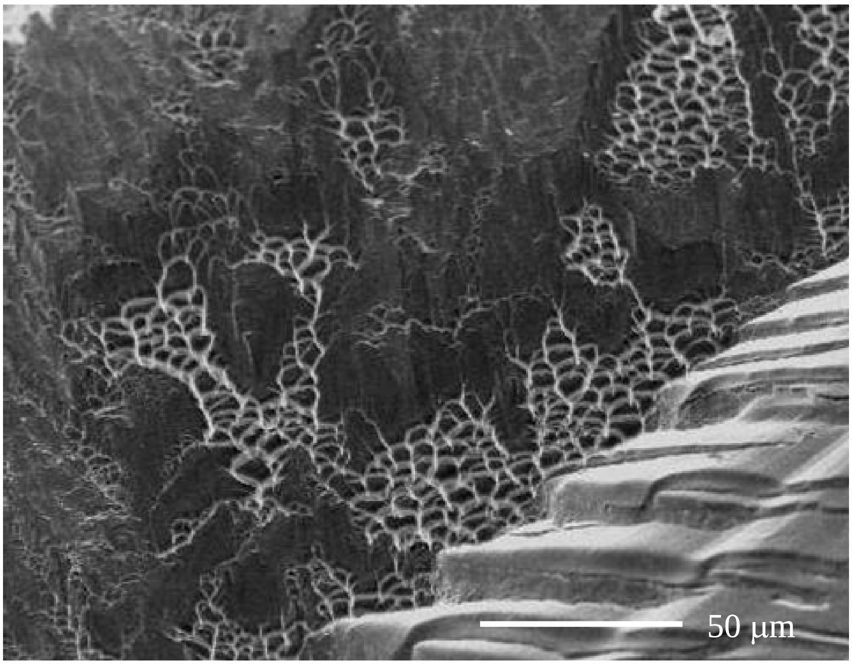

Figure 4.29 The cross-sectional view showing fracture morphology of the $Mg_{65}Cu_{25}Gd_{10}$ BMG with a h/d ratio of 0.5.

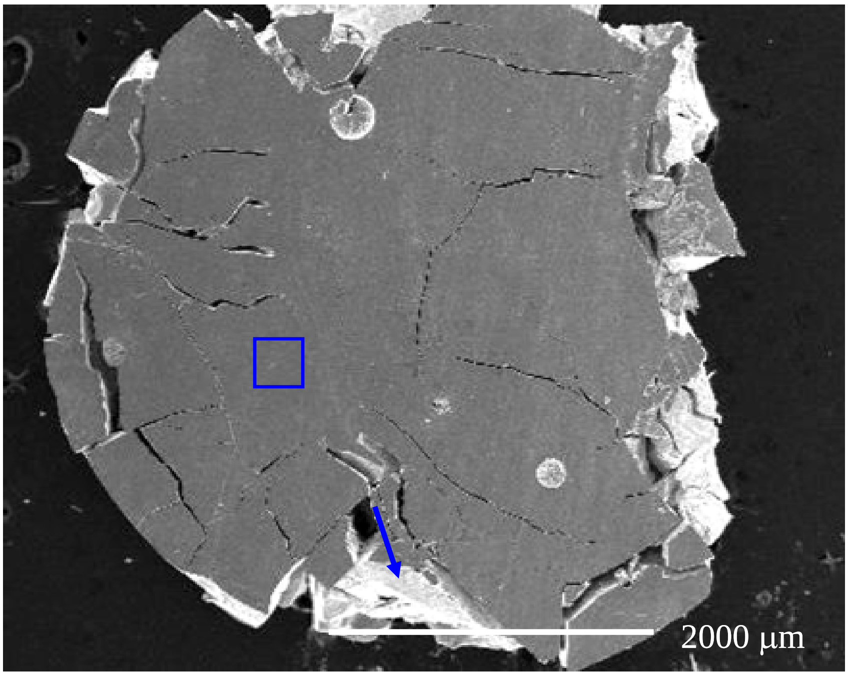

Figure 4.30 The outer appearance showing fracture plane of the $Mg_{65}Cu_{25}Gd_{10}$ BMG with a h/d ratio of 0.25.

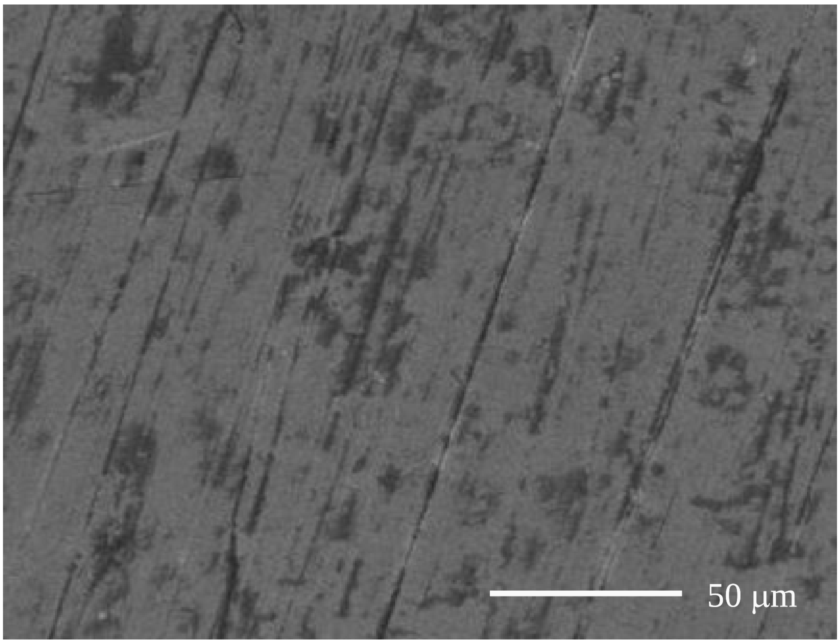

Figure 4.31 The fracture surface morphology of the $Mg_{65}Cu_{25}Gd_{10}$ BMG with a h/d ratio of 0.25.

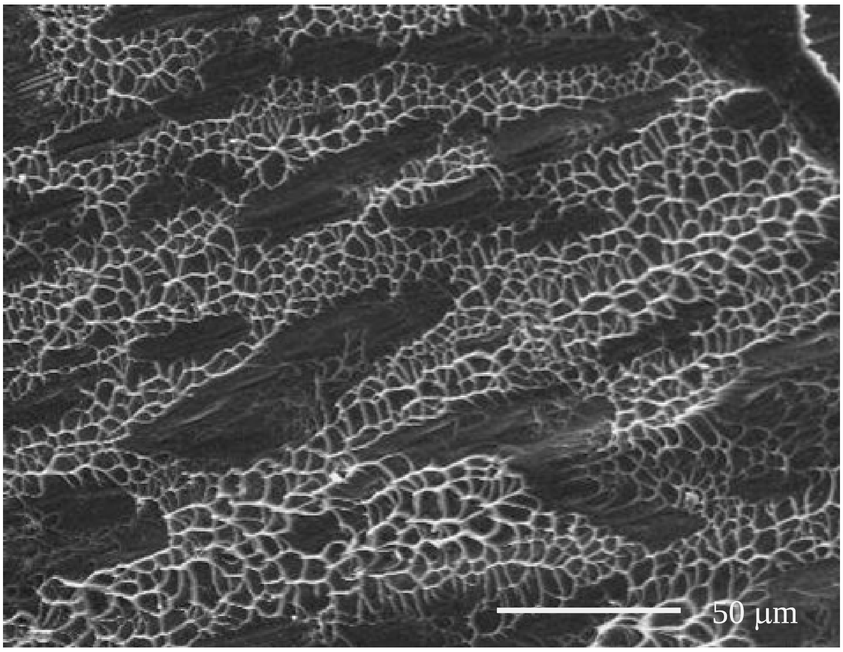

Figure 4.32 The fracture surface morphology of the $Mg_{65}Cu_{25}Gd_{10}$ BMG with a h/d ratio of 0.25.

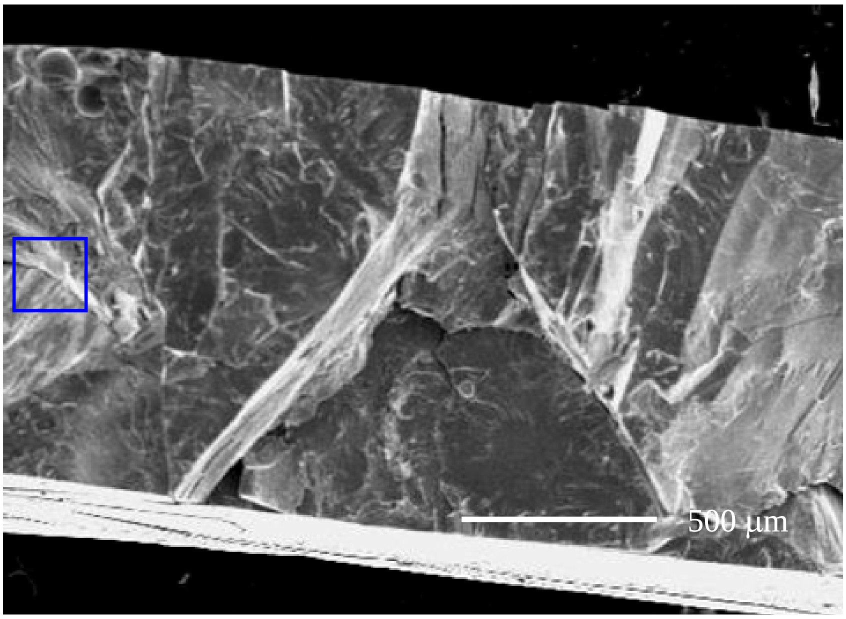

Figure 4.33 The cross-sectional view showing fracture morphology of the $Mg_{65}Cu_{25}Gd_{10}$ BMG with a h/d ratio of 0.25.

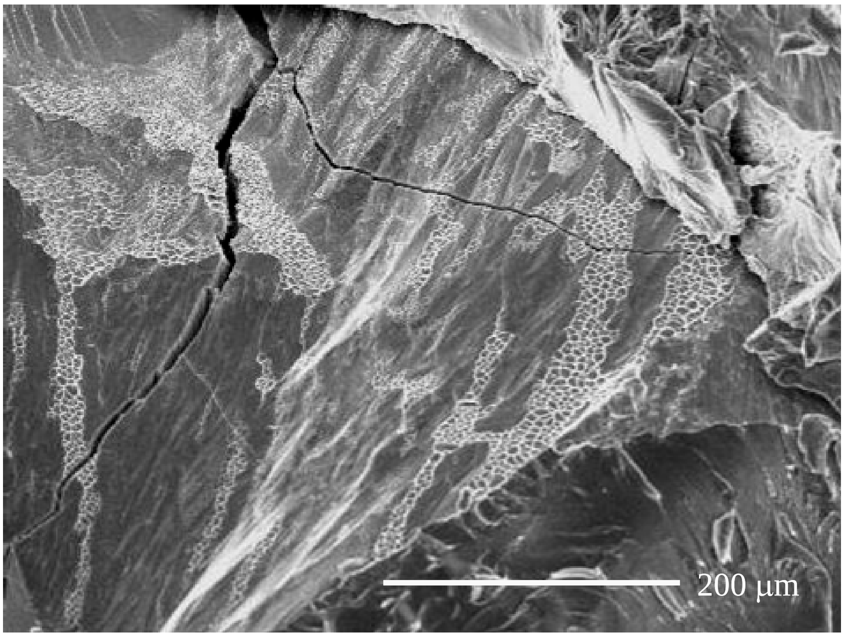

Figure 4.34 The cross-sectional view showing fracture morphology of the $Mg_{65}Cu_{25}Gd_{10}$ BMG with a h/d ratio of 0.25.

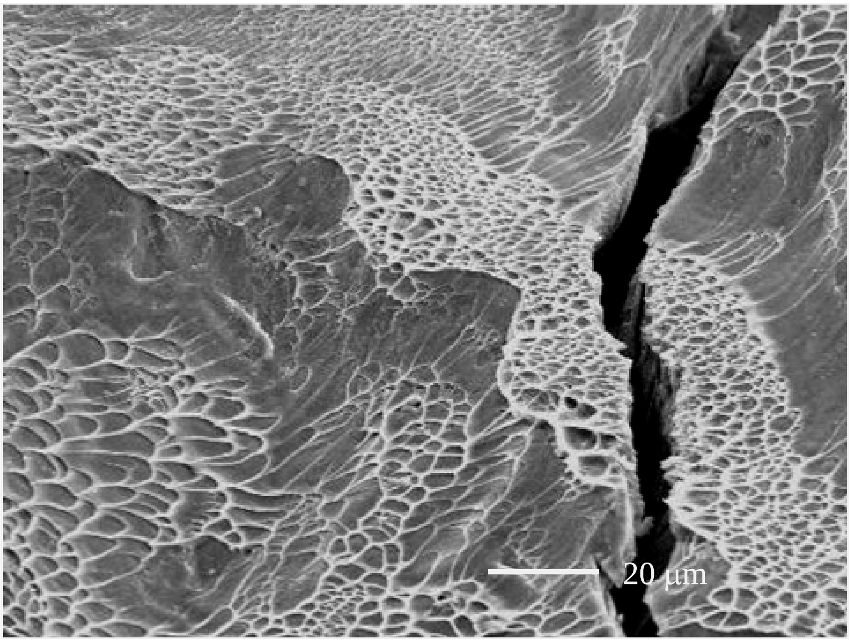

Figure 4.35 The cross-sectional view showing fracture morphology of the $Mg_{65}Cu_{25}Gd_{10}$ BMG with a h/d ratio of 0.25.

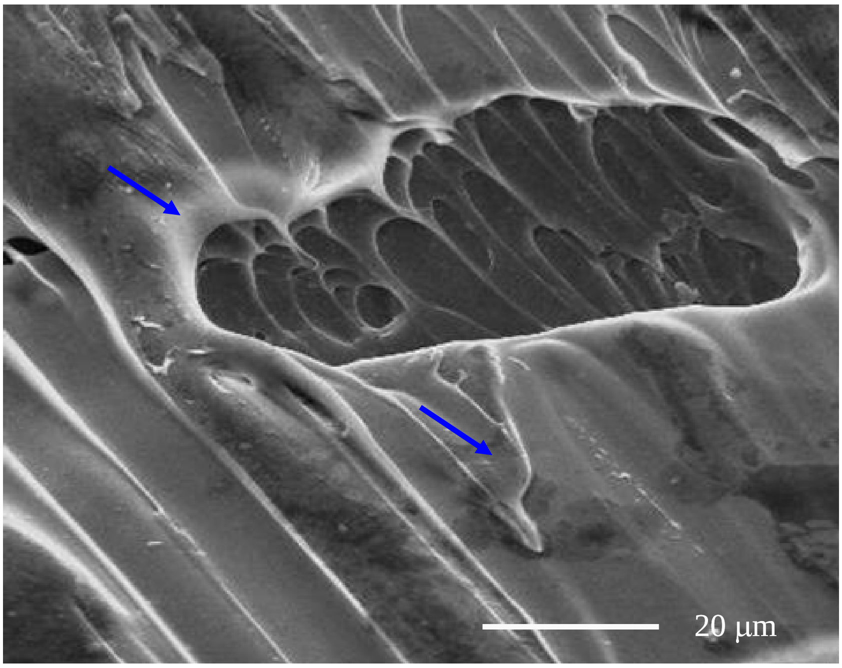

Figure 4.36 The compressive fracture surface showing flow layers of the $Mg_{65}Cu_{25}Gd_{10}$ BMG.

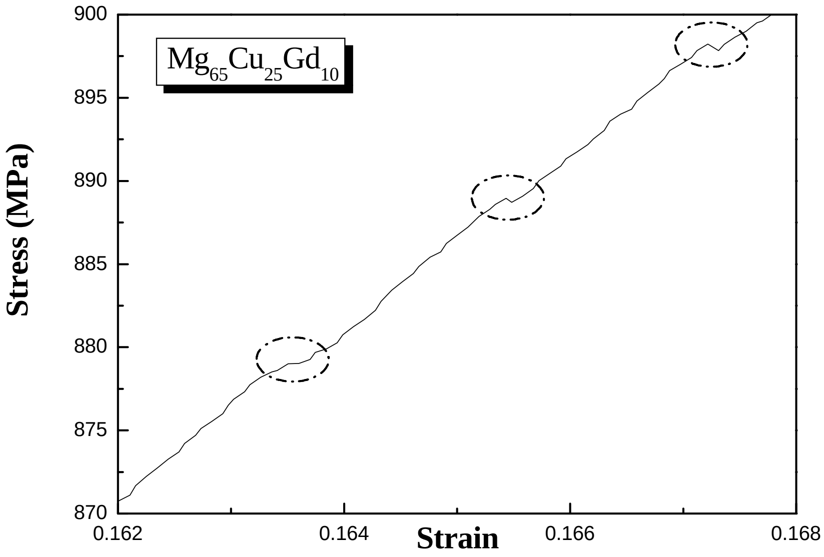

Figure 5.3 The compressive stress-strain curve of the $Mg_{65}Cu_{25}Gd_{10}$ BMG with h/d = 1:4 showing the serrated flow phenomenon.

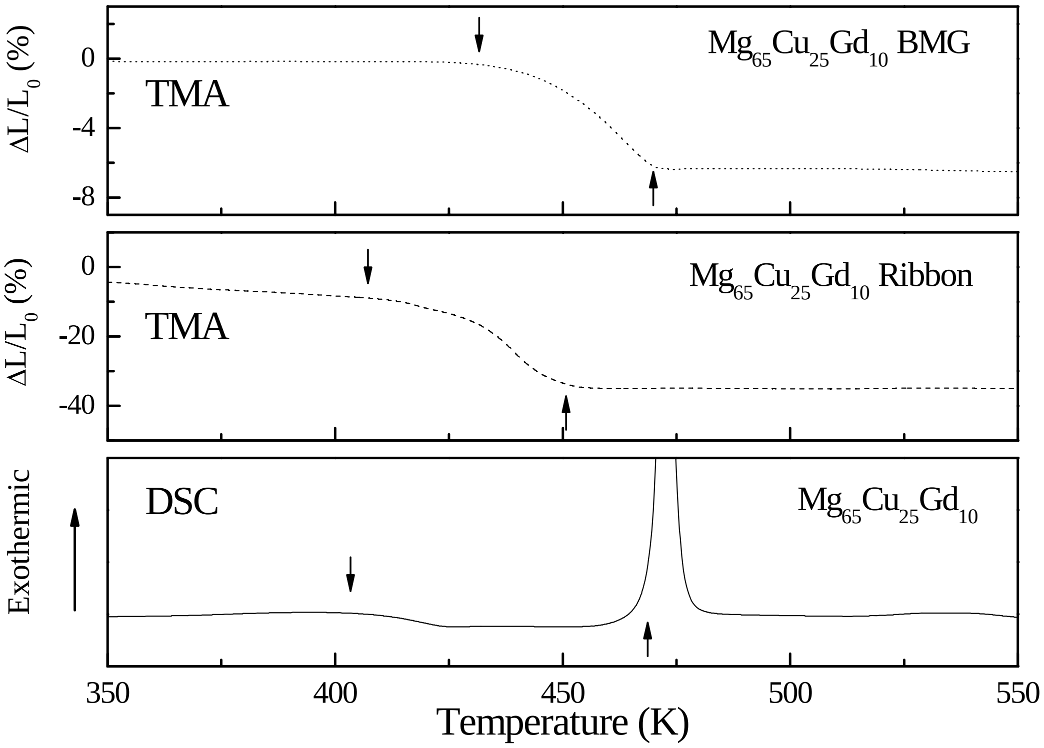

Figure 5.1 The combination of DSC and TMA curves for the $Mg_{65}Cu_{25}Gd_{10}$ ribbon and BMG at the heating rate of 0.17 K/s.

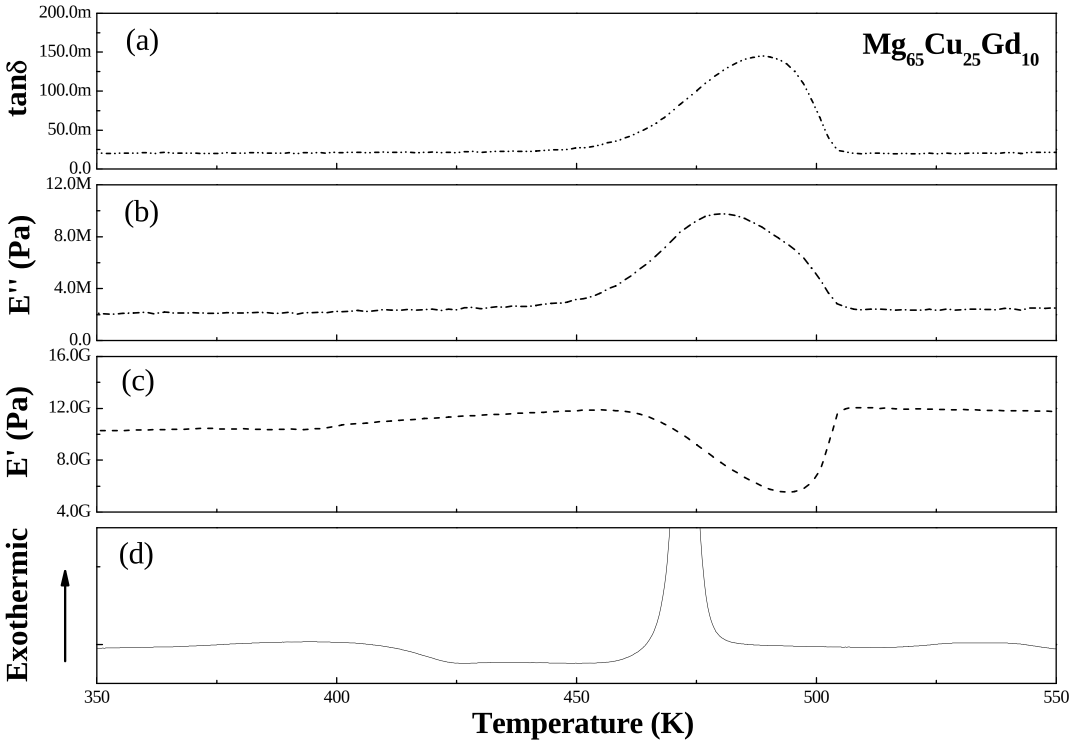

Figure 5.2 DSC curve and temperature dependences of E’, E’’, and tan δ for the $Mg_{65}Cu_{25}Gd_{10}$ BMG at the heating rate of 0.17 K/s: (a) temperature dependences of tan δ; (b) temperature dependences of E’’; (c) temperature dependences of E’; (d) DSC curve.

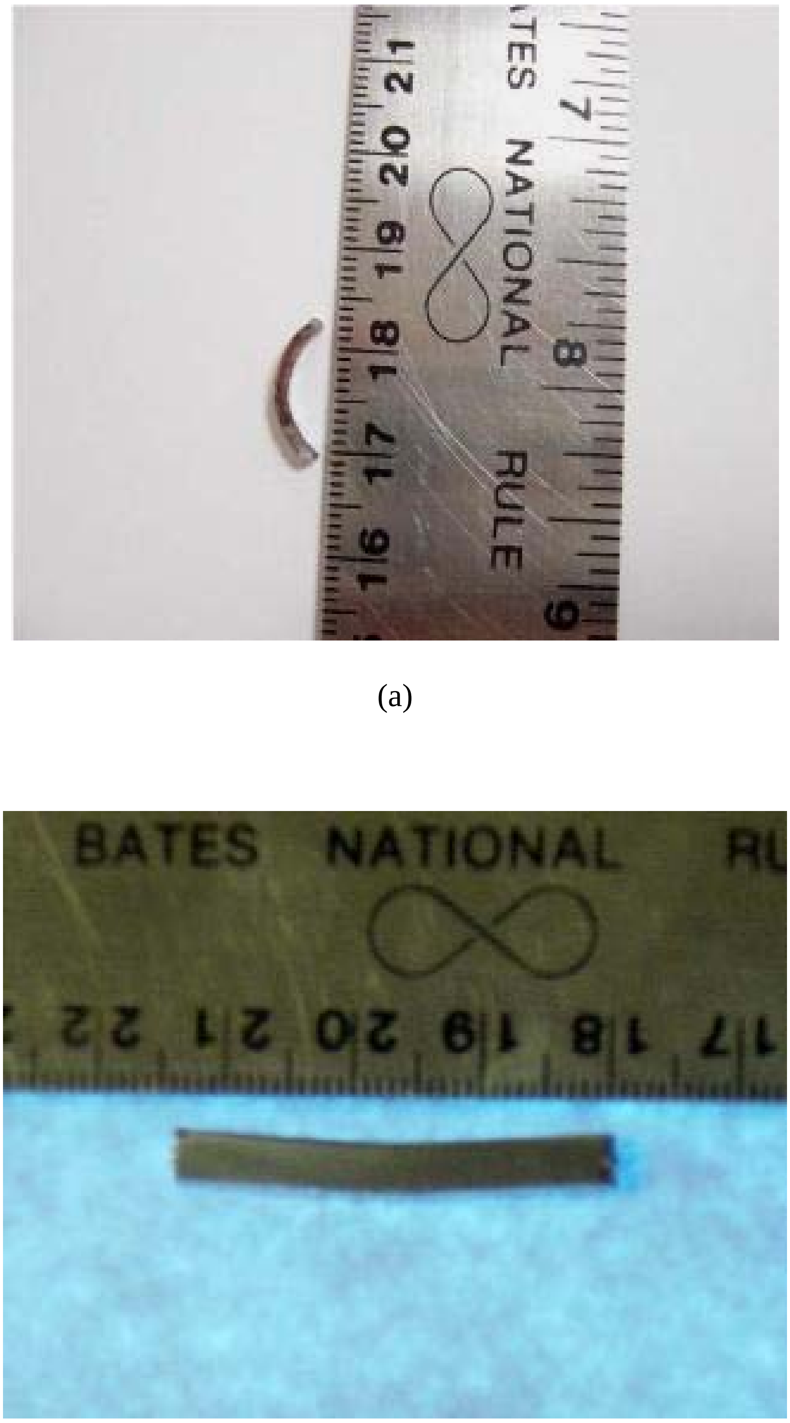

(a)

(b)

Figure 5.3 (a) A 1.8 mm x 3 mm x 15 mm bar shaped $Pt_{57.5}Cu_{14.7}Ni_{5.3}P_{22.5}$ sample bent over a mandrel of radius 6.35 mm. The strain to failure exceeds 14.2 %. (b) $Pt_{57.5}Cu_{14.7}Ni_{5.3}P_{22.5}$ samples with dimensions of 4 mm x 4 mm x 34 mm bent over a mandrel with a radius of 6 cm. The strain to failure exceeds 3 % [61].

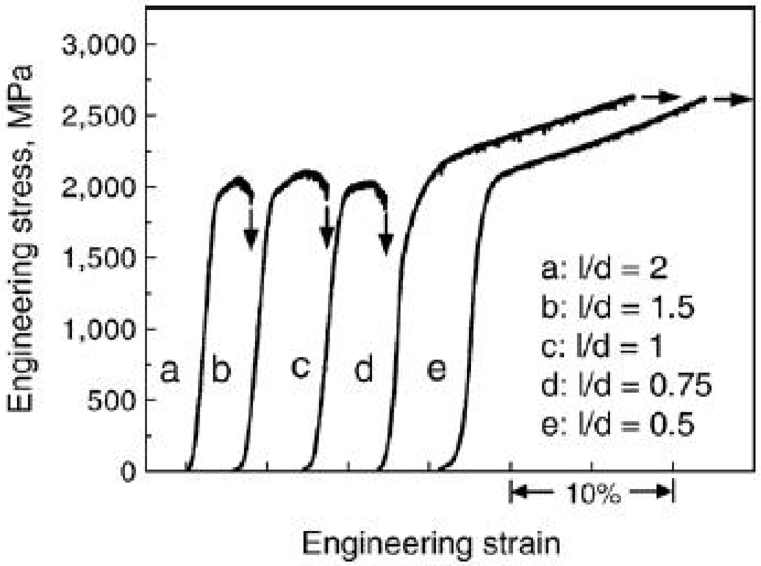

Figure 5.4 Compressive stress–strain curves of the specimens for $Zr_{52.5}Cu_{17.9}Ni_{14.6}Al_{10}Ti_5$ with various l /d ratios at a strain rate of 3.9×10^{-3} s^{-1} [62].

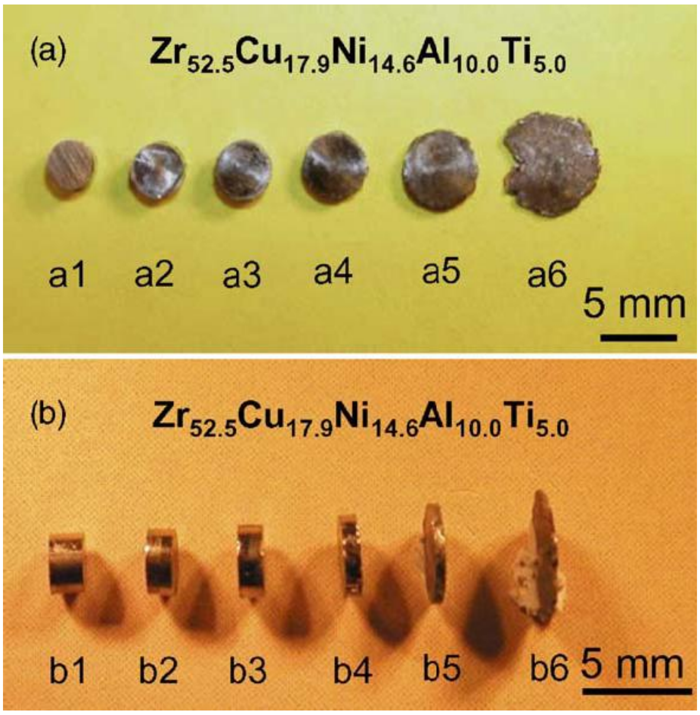

Figure 5.5 A planar view (a) and an edge view (b) of the undeformed and deformed specimens for $Zr_{52.5}Cu_{17.9}Ni_{14.6}Al_{10}Ti_5$ with an l /d ratio of 0.5. (a1) and (b1) undeformed, (a2) and (b2) 18.5% in elongation, (a3) and (b3) 28.5% in elongation, (a4) and (b4) 46.5% in elongation, (a5) and (b5) 61.7% in elongation, and (a6) and (b6) 76.4% in elongation [62].